

ISSN 2782-2192 (Print)
ISSN 2782-2206 (Online)

Journal of Advanced Materials and Technologies

J·A·M·T

**Vol. 8, No. 4.
2023**



TSTU Publishing

ISSN 2782-2192 (Print)
ISSN 2782-2206 (Online)
DOI: 10.17277/issn.2782-2192



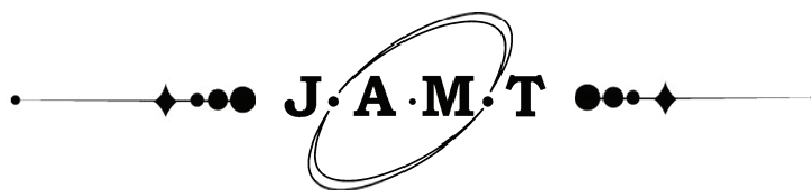
Journal of Advanced Materials and Technologies

**Vol. 8, No. 4.
2023**

**Tom 8, № 4.
2023**

16+

© Tambov State Technical University, Tambov, Russian Federation, 2023
© Merzhanov Institute of Structural Macrokinetics and Materials Sciences of Russian Academy of Sciences,
Chernogolovka, Moscow region, Russian Federation, 2023
© Design by TSTU Publishing, 2023



Journal of Advanced Materials and Technologies

Scientific Journal

“Journal of Advanced Materials and Technologies” is a peer-reviewed scientific journal of research in materials science and related issues in materials physics and mechanics.

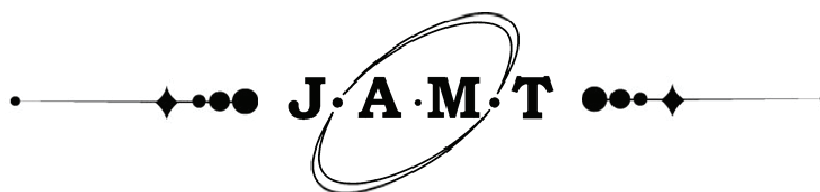
“Journal of Advanced Materials and Technologies” publishes original articles, reviews, short reports written by both renowned scientists and young researchers that contribute to the development of modern materials science.

The journal promotes research and exchange of information in the field of theoretical and practical research into materials science, modeling of processes involved in the creation of new materials, including nanomaterials, their properties and application.

The journal papers and metadata are available at Chemical Abstracts, CAS (American Chemical Society), Google Scholar, WorldCat, ROAR (Registry of Open Access Repositories), OpenAIRE (OpenAIRE - Open Access Infrastructure for Research in Europe), BASE (Bielefeld Academic Search Engine), RePEc: Research Papers in Economics, EBSCO.

ISSN 2782-2192 (Print), ISSN 2782-2206 (Online)

Rename information	Advanced materials & technologies (2016-2021) Print ISSN 2414-4606, Online ISSN 2541-8513
The journal was founded	2016
Publication frequency	Quarterly
Founders	Tambov State Technical University (TSTU), Merzhanov Institute of Structural Macrokinetics and Materials Sciences of Russian Academy of Sciences (ISMAN)
Postal address	TSTU: Bld. 2, 106/5, Sovetskaya St., Tambov, 392000 ISMAN: 8, Academician Osipyan St., Moscow region, Chernogolovka, 142432
Editorial office address	Bld. 2, 106/5, Sovetskaya St., Tambov, 392000
Contacts	Phone + 7 4752 63 03 91; amt.journal@yandex.ru
Printing House	TSTU Publishing, 112A, Michurinskaya St., Tambov, 392032 Phone + 7 4752 63 03 91; + 7 4752 63 07 46
Website	http://amt.tstu.ru/
E-mail	amt.journal@yandex.ru
Phone	+7 4752 63 92 93
Subscription	The electronic version of the Journal is freely available on the journal's website, as well as in open access databases. The subscription index for the Journal printed version in the unified catalog “Press of Russia” is 80453
Editor-in-Chief	Mikhail I. Alymov, D. Sc. (Engineering), Professor, Corresponding Member of the Russian Academy of Sciences



Journal of Advanced Materials and Technologies

Научный журнал

«**Journal of Advanced Materials and Technologies**» – научный рецензируемый журнал, посвященный исследованиям в области материаловедения и примыкающих вопросов физики и механики материалов.

Журнал «**Journal of Advanced Materials and Technologies**» публикует оригинальные статьи, обзоры, краткие сообщения, содействующие развитию современной науки о материалах, подготовленные как известными учеными, так и молодыми специалистами.

Миссия журнала – обмен актуальной научной информацией в области теоретических и практических исследований и моделирования процессов, связанных с получением, определением свойств новых материалов, в том числе наноразмерных, и их применения.

Средство массовой информации периодическое печатное издание, журнал «**Journal of Advanced Materials and Technologies**» зарегистрировано Федеральной службой по надзору в сфере связи, информационных технологий и массовых коммуникаций. Регистрационный номер СМИ ПИ № ФС 77-74804 от 25.01.2019.

Журнал входит в перечень рецензируемых научных изданий (перечень ВАК Минобрнауки РФ) от 16 декабря 2021 г. по научным специальностям: 1.4.15 – Химия твердого тела; 2.6.6 – Нанотехнологии и наноматериалы; 2.6.13 – Процессы и аппараты химических технологий; 2.6.17 – Материаловедение.

Материалы журнала размещены в РИНЦ, Chemical Abstracts, CAS (American Chemical Society), Академия Google (Google Scholar), WorldCat, СОЦИОНЕТ, ROAR (Registry of Open Access Repositories), OpenAIRE (OpenAIRE - Open Access Infrastructure for Research in Europe), BASE (Bielefeld Academic Search Engine), RePEc: Research Papers in Economics, EBSCO.

ISSN 2782-2192 (Print), ISSN 2782-2206 (Online)

**Сведения
о переименовании**

«Advanced materials & technologies» (2016–2021)
Print ISSN 2414-4606, Online ISSN 2541-8513

Журнал основан

2016 г.

Периодичность

4 раза в год

Учредители

Федеральное государственное бюджетное образовательное учреждение высшего образования «Тамбовский государственный технический университет» (ФГБОУ ВО «ТГТУ»),
Федеральное государственное бюджетное учреждение науки Институт структурной макрокинетики и проблем материаловедения им. А. Г. Мержанова Российской академии наук (ИСМАН)

Адреса учредителей

ФГБОУ ВО «ТГТУ»: 392000, Тамбовская область, г.о. город Тамбов, г. Тамбов, ул. Советская, д. 106/5, помещ. 2,
ИСМАН: 142432, Московская область, г. Черноголовка, ул. Академика Осипьяна, д. 8

Адрес издателя

ФГБОУ ВО «ТГТУ»: 392000, Тамбовская область, г.о. город Тамбов, г. Тамбов, ул. Советская, д. 106/5, помещ. 2

Адрес редакции

392000, Тамбовская область, г.о. город Тамбов, г. Тамбов, ул. Советская, д. 106/5, помещ. 2

Контакты

Тел.: + 7 4752 63 03 91; amt.journal@yandex.ru

Адрес типографии

392032, Тамбовская обл., г. Тамбов, ул. Мичуринская, д. 112А

Тел.: + 7 4752 63 03 91; + 7 4752 63 07 46

Сайт

<http://amt.tstu.ru/>

E-mail

amt.journal@yandex.ru

Телефон

+7 4752 63 92 93

Подписка

Подписку на печатную версию журнала можно оформить по объединенному каталогу «Пресса России». Подписной индекс – 80453

Главный редактор

Алымов Михаил Иванович, д. т. н., профессор, член-корреспондент РАН

EDITORS

- Mikhail I. Alymov**, D. Sc. (Eng.), Professor, Corresponding Member of the Russian Academy of Sciences (RAS), Director of Merzhanov Institute of Structural Macrokinetics and Materials Sciences RAS (ISMAN), Chernogolovka, Moscow Region, Russian Federation
- Mikhail N. Krasnyansky**, D. Sc. (Eng.), Professor, Rector of Tambov State Technical University (TSTU), Tambov, Russian Federation
- Alexey G. Tkachev**, D. Sc. (Eng.), Professor, Head of Department of Technologies and Methods of Nanoproducts Manufacturing, TSTU, Tambov, Russian Federation
- Irina V. Burakova**, Ph.D., Associate Professor of Department of Technologies and Methods of Nanoproducts Manufacturing, TSTU, Tambov, Russian Federation
- Imran Ali**, Ph.D., FRSC, Professor, Department of Chemistry, Jamia Millia Islamia (Central University), New Delhi, India
- Vyacheslav M. Buznik**, D. Sc. (Chem.), Professor, RAS Academician, All-Russian Scientific Research Institute of Aviation Materials, Moscow, Russian Federation
- Stepan N. Kalmykov**, D. Sc. (Chem.), Professor, RAS Academician, Dean of the Faculty of Chemistry at the Lomonosov Moscow State University, Moscow, Russian Federation
- Valeriy P. Meshalkin**, D. Sc. (Eng.), Professor, RAS Academician, Head of Department of Logistics and Economic Informatics, Mendelev University of Chemical Technology of Russia, Moscow, Russian Federation
- Tatyana P. Dyachkova**, D. Sc. (Chem.), Professor, Director of Center for Collective Use of Scientific Equipment "Production and Application of Multifunctional Nanomaterials", TSTU, Tambov, Russian Federation
- Jesus Iniesta Valcarcel**, Ph.D., Associate Professor, Department of Physical Chemistry, University of Alicante, Alicante, Spain
- Rami J. Sldozian**, PhD, Lecturer at the Department of Applied Science, University of Technology, Baghdad, Iraq
- Ruslan Kh. Khamizov**, D. Sc. (Chem.), Professor, Director of Vernadsky Institute of Geochemistry and Analytical Chemistry of RAS, Moscow, Russian Federation
- Mikhail L. Kheifetz**, D. Sc. (Eng.), Professor, Director of Institute of Applied Physics of National Academy of Science of Belarus, Minsk, Belarus
- Roman B. Morgunov**, D. Sc. (Phys. and Math.), Professor, Leading Researcher, Institute of Problems of Chemical Physics RAS, Chernogolovka, Moscow Region, Russian Federation
- Fadei F. Komarov**, D. Sc. (Phys. and Math.), Professor, Academician of the National Academy of Sciences of Belarus, Head of Elionics Laboratory at A. N. Sevchenko Institute of Applied Physical Problems of Belarusian State University, Minsk, Belarus
- Stephane Mangin**, Ph.D., Professor, Physics of Matter and Materials Department, Institute Jean Lamour, University of Lorraine, Nancy, France
- Vladimir F. Pershin**, D. Sc. (Eng.), Professor, Professor at the Department of Technologies and Methods of Nanoproducts Manufacturing, TSTU, Tambov, Russian Federation
- Dimiter Stavrev**, D. Sc. (Eng.), Professor, Professor of Department of Materials Science at the Technical University of Varna, Varna, Bulgaria
- Alexander M. Stolin**, D. Sc. (Phys. and Math.), Professor, Head of Laboratory, ISMAN RAS, Chernogolovka, Moscow Region, Russian Federation
- Yoshifumi Tanimoto**, Ph.D., Professor, Hiroshima University, Japan
- Vener A. Valitov**, D. Sc. (Eng.), Leading Researcher, Institute for Metals Superplasticity Problems of the Russian Academy of Sciences, Ufa, Russian Federation
- Sergey M. Arakelian**, D. Sc. (Phys. and Math.), Professor, Head of the Department of Physics and Applied Mathematics, Vladimir State University, Vladimir, Russian Federation
- Arif A. Babaev**, D. Sc. (Phys. and Math.), Professor, Head of the Laboratory of Optical Phenomena in Condensed Matter, Institute of Physics of Dagestan Scientific Center of Russian Academy of Sciences, Makhachkala, Republic of Dagestan, Russian Federation
- Evgeniy I. Terukov**, D. Sc. (Eng.), Professor, Deputy Director for Science of R&D Center of Thin-Film Technology for Energetics under Ioffe Institute, St. Petersburg, Russian Federation
- Valeriy Yu. Dolmatov**, D. Sc. (Eng.), Head of Research Laboratory at the "Special Construction and Technology Bureau "Technolog", St. Petersburg, Russian Federation
- Valeriy V. Savin**, D. Sc. (Phys. and Math.), Leading Researcher, Head of the Laboratory of Physical Materials Science, International Research Center "X-ray Coherent Optics", Immanuel Kant Baltic Federal University, Kaliningrad, Russian Federation
- Gennady E. Selyutin**, Ph.D., Associate Professor, Senior Researcher, Federal Research Center "Krasnoyarsk Science Center" of Siberian Branch of the Russian Academy of Sciences, Krasnoyarsk, Russian Federation
- Vladimir V. Petrov**, D. Sc. (Phys. and Math.), Professor, Saratov State University, Saratov, Russian Federation
- Yury E. Kalinin**, D. Sc. (Phys. and Math.), Professor, Voronezh State Technical University, Voronezh, Russian Federation
- Vladimir S. Sevostyanov**, D. Sc. (Eng.), Professor, Head of the Department "Technological Complexes, Machines and Mechanisms", V. G. Shukhov Belgorod State Technological University, Belgorod, Russian Federation
- Victor M. Mukhin**, D. Sc. (Eng.), Professor, D. Mendelev University of Chemical Technology of Russia, Moscow, Russian Federation
- Vladimir D. Vermel**, D. Sc. (Eng.), Professor, Head of the Scientific and Technical Center of the Scientific and Production Complex, Central Aerohydrodynamic Institute, Zhukovsky, Moscow Region, Russian Federation
- Nadezhda V. Usoltseva**, D. Sc. (Chem.), Professor, Director of the Research Institute of Nanomaterials, Ivanovo State University, Ivanovo, Russian Federation
- Lyaylya A. Abdrakhmanova**, D. Sc. (Eng.), Professor, Kazan State University of Architecture and Engineering, Kazan, Russian Federation
- Vyacheslav A. Sergeev**, D. Sc. (Eng.), Professor, Director of the Ulyanovsk branch of Kotelnikov Institute of Radioengineering and Electronics of Russian Academy of Science, Ulyanovsk, Russian Federation
- Irina V. Zaporotskova**, D. Sc. (Phys. and Math.), Professor, Director of the Institute of Priority Technologies, Volgograd State University, Volgograd, Russian Federation
- Vladimir E. Guterma**, Ph.D., Professor, Leading Researcher, Southern Federal University, Rostov-on-Don, Russian Federation
- Valeria S. Tafintseva**, Ph.D., Researcher, Department of Physics, Faculty of Science and Engineering, Norwegian University of Life Sciences, Norway
- Vyacheslav M. Tyutyunik**, D. Sc. (Eng.), Professor, Director General of International Nobel Information Centre (INIC), Ltd., TSTU, Tambov, Russian Federation
- Translator:** Natalia A. Gunina, Ph.D., Associate Professor, Head of Department of International Professional and Scientific Communication, TSTU, Tambov, Russian Federation

СОВЕТ РЕДАКТОРОВ

- Алымов Михаил Иванович**, д.т.н., профессор, член-корреспондент РАН, директор Института структурной макрокинетики и материаловедения им. А.Г. Мерджанова РАН (ИСМАН), Черноголовка, Московская область, Россия
- Краснянский Михаил Николаевич**, д.т.н., профессор, ректор, Тамбовский государственный технический университет (ТГТУ), Тамбов, Россия
- Ткачев Алексей Григорьевич**, д.т.н., профессор, заведующий кафедрой «Техника и технологии производства нанопроductов», ТГТУ, Тамбов, Россия
- Буракова Ирина Владимировна**, к.т.н., доцент, доцент кафедры «Техника и технологии производства нанопроductов», ТГТУ, Тамбов, Россия
- Али Ибран**, PhD, FRSC, профессор кафедры химии, Джамиа Миллия Исламия (Центральный университет), Нью-Дели, Индия
- Бузник Вячеслав Михайлович**, д.х.н., профессор, академик РАН, Всероссийский научно-исследовательский институт авиационных материалов, Москва, Россия
- Калмыков Степан Николаевич**, д.х.н., профессор, академик РАН, декан химического факультета Московского государственного университета им. М. В. Ломоносова, Москва, Россия
- Мешалкин Валерий Павлович**, д.т.н., профессор, академик РАН, заведующий кафедрой «Логистики и экономической информатики» Российского химико-технологического университета им. Д. И. Менделеева, Москва, Россия
- Дьячкова Татьяна Петровна**, д.х.н., профессор, директор центра коллективного пользования научным оборудованием «Получение и применение полифункциональных наноматериалов», ТГТУ, Тамбов, Россия
- Иньеста Хесус Валькарсель**, Ph.D., доцент кафедры физической химии Университета Аликанте, Аликанте, Испания
- Слдоэян Рами Джозеф**, к.т.н., преподаватель кафедры прикладных наук, Технологический университет, Багдад, Ирак
- Хамизов Руслан Хажсетович**, д.х.н., профессор, директор, Институт геохимии и аналитической химии им. В. И. Вернадского РАН, Москва, Россия
- Хейфец Михаил Львович**, д.т.н., профессор, директор института, Институт прикладной физики НАН Беларуси, Минск, Беларусь
- Морзунов Роман Борисович**, д.ф.-м.н., профессор, главный научный сотрудник, Институт проблем химической физики РАН, г. Черноголовка, Московская область, Россия
- Комаров Фадей Фадеевич**, д.ф.-м.н., профессор, академик Национальной академии наук Республики Беларусь, заведующий лабораторией эллионики, Институт прикладных физических проблем им. А. Н. Севченко Белорусского государственного университета, Минск, Беларусь
- Мангин Стефан**, Ph.D., профессор кафедры физики материи и материалов Института Жана Ламура, Университет Лотарингии, Нанси, Франция
- Першин Владимир Федорович**, д.т.н., профессор, профессор кафедры «Техника и технологии производства нанопроductов», ТГТУ, Тамбов, Россия
- Ставрев Димитр**, д.т.н., профессор, профессор кафедры «Материаловедения», Варненский технический университет, Варна, Болгария
- Столин Александр Моисеевич**, д.ф.-м.н., профессор, заведующий лабораторией, ИСМАН РАН, Черноголовка, Московская область, Россия
- Танимото Есифуми**, Ph.D., профессор, Хиросимский университет, Япония
- Валитов Венер Анварович**, д.т.н., ведущий научный сотрудник, Институт проблем сверхпластичности металлов РАН, Уфа, Республика Башкортостан, Россия
- Аракелян Сергей Мартиросович**, д.ф.-м.н., профессор, заведующий кафедрой физики и прикладной математики, Владимирский государственный университет им. А. Г. и Н. Г. Столетовых, Владимир, Россия
- Бабеев Ариф Азимович**, д.ф.-м.н., профессор, заведующий лабораторией оптических явлений в конденсированных средах Института физики им. Х. И. Амиханова ДНЦ РАН, Махачкала, Республика Дагестан, Россия
- Теруков Евгений Иванович**, д.т.н., профессор, заместитель генерального директора по научной работе ООО «НТЦ тонкопленочных технологий в энергетике при ФТИ им. А.Ф. Иоффе», Санкт-Петербург, Россия
- Долматов Валерий Юрьевич**, д.т.н., начальник научно-исследовательской лаборатории, «Специальное конструкторско-технологическое бюро «Технолог», Санкт-Петербург, Россия
- Савин Валерий Васильевич**, д.ф.-м.н., ведущий научный сотрудник, заведующий лабораторией физического материаловедения МНИЦ «Когерентная рентгеновская оптика для установок «Мегасайенс», Балтийский федеральный университет им. Иммануила Канта, Калининград, Россия
- Селютин Геннадий Егорович**, к.ф.-м.н., доцент, старший научный сотрудник, Институт химии и химической технологии Сибирского отделения Российской академии наук ФИЦ КНЦ СО РАН, Красноярск, Россия
- Петров Владимир Владимирович**, д.ф.-м.н., профессор, Саратовский национальный исследовательский университет им. Н. Г. Чернышевского, Саратов, Россия
- Калинин Юрий Егорович**, д.ф.-м.н., профессор, Воронежский государственный технический университет, Воронеж, Россия
- Севостьянов Владимир Семенович**, д.т.н., профессор, заведующий кафедрой «Технологические комплексы, машины и механизмы», Белгородский государственный технологический университет им. В. Г. Шухова, Белгород, Россия
- Мухин Виктор Михайлович**, д.т.н., профессор, Российский химико-технологический университет им. Д. И. Менделеева, Москва, Россия
- Вермель Владимир Дмитриевич**, д.т.н., профессор, начальник Научно-технического центра научно-производственного комплекса, Центральный аэрогидродинамический институт им. профессора Н. Е. Жуковского, Московская область, Жуковский, Россия
- Усольцева Надежда Васильевна**, д.х.н., профессор, директор НИИ наноматериалов, Ивановский государственный университет, Иваново, Россия
- Абдрахманова Ляйля Абдулловна**, д.т.н., профессор, Казанский государственный архитектурно-строительный университет, Казань, Россия
- Сергеев Вячеслав Андреевич**, д.т.н., профессор, директор Ульяновского филиала ФГБУН «Институт радиотехники и электроники им. В. А. Котельникова» РАН, Ульяновск, Россия
- Запороцкова Ирина Владимировна**, д.ф.-м.н., профессор, директор института приоритетных технологий, Волгоградский государственный университет, Волгоград, Россия
- Гутерман Владимир Ефимович**, д.х.н., профессор, главный научный сотрудник, Южный федеральный университет, Ростов-на-Дону, Россия
- Тафинцева Валерия Сергеевна**, Ph.D., научный сотрудник, кафедра физики, факультет науки и технологий, Норвежский университет естественных наук, Норвегия
- Тютюнник Вячеслав Михайлович**, д.т.н., профессор, генеральный директор ООО «Международный информационный Нобелевский центр» (МИНЦ), ТГТУ, Тамбов, Россия
- Переводчик:** Гунина Наталия Александровна, к.ф.н., заведующий кафедрой «Международная научная и профессиональная коммуникация», ТГТУ, Тамбов, Россия

CONTENTS

Original papers

Nanostructured, nanoscale materials and nanodevices

- Morozov M. V., Mansurov R. N., Drobyshev S. V.** Synthesis of nickel nanostructured microfibers to increase the electrochemical activity of nickel electrodes 260

Materials for energy and environment, next-generation photovoltaics, and green technologies

- Shubin I. N., Mkrtchyan E. S., Ananyeva O. A.** Promising sorbents based on compacted highly porous carbon materials 270
- Belov D. V., Belyaev S. N., Yunin P. A., Radishev D. B.** A method of obtaining aluminum tris(8-hydroxyquinoline) and its physicochemical properties 279
- Boiprav O. V., Bogush V. A., Grinchik N. N.** Multifunctional composite charcoal-containing microwave and X-ray radiation absorbers 294

Advanced structural materials, materials for extreme conditions

- Malakhov A. Yu., Saikov I. V., Denisov I. V., Berdychenko A. A., Ivanov S. G., Niyozbekov N. N.** AlMg6–AlMg6 weld interface: microstructure and mechanical properties after explosive welding 304
- Aljaboobi D. Z. M., Burakova I. V., Burakov A. E., Yarkin V. O.** Evaluation of the effect of a complex nanomodifying additive “lignosulfonate/graphene oxide” on the non-autoclaved aerated concrete hydration process 316
- Abzalov N. I., Septyarskii B. S., Kochetkov R. A., Lisina T. G., Alymov M. I.** Synthesis of the TiC + 20% NiCr composite from a granular mixture 324

СОДЕРЖАНИЕ

Оригинальные статьи

Наноструктурированные, наномасштабные материалы и наноустройства

- Морозов М. В., Мансуров Р. Н., Дробышев С. В. Синтез никелевых наноструктурированных микроволокон для повышения электрохимической активности никелевых электродов 260

Материалы для энергетики и окружающей среды, фотоэлектрическая энергия следующего поколения и зеленые технологии

- Шубин И. Н., Мкртчян Э. С., Ананьева О. А. Перспективные сорбенты на основе компактированного высокопористого углеродного материала 270
- Белов Д. В., Беляев С. Н., Юнин П. А., Радищев Д. Б. Способ получения и физико-химические свойства трис(8-гидроксихинолината) алюминия 279
- Бойправ О. В., Богущ В. А., Гринчик Н. Н. Многофункциональные композиционные углесодержащие поглотители микроволнового и рентгеновского электромагнитного излучения 294

Современные конструкционные материалы, материалы для экстремальных условий

- Малахов А. Ю., Сайков И. В., Денисов И. В., Бердыченко А. А., Иванов С. Г., Ниёзбеков Н. Н. Граница соединения АМг6–АМг6: микроструктура и механические свойства после сварки взрывом 304
- Альджабуи Д. З. М., Буракова И. В., Бураков А. Е., Яркин В. О. Оценка влияния комплексной наномодифицирующей добавки «лигносульфонат/оксид графена» на процесс гидратации неавтоклавногазобетона 316
- Абзалов Н. И., Сеплярский Б. С., Кочетков Р. А., Лисина Т. Г., Алымов М. И. Синтез композита TiC + 20 % NiCr из гранулированной шихты 324

Synthesis of nickel nanostructured microfibers to increase the electrochemical activity of nickel electrodes

© Mikhail V. Morozov^a✉, Ravil N. Mansurov^b, Sergey V. Drobyshev^a

^a Kazan National Research Technical University named after A. N. Tupolev – KAI,
10, Karl Marx St., Kazan, 423111, Russian Federation,

^b A. E. Arbuzov Institute of Organic and Physical Chemistry KazNC RAS,
8, Akademika Arbuzova St., Kazan, 423088, Russian Federation

✉ misha617@mail.ru

Abstract: At present, the investigation of the properties of nanostructured materials for electrochemical applications, in particular for the development of promising supercapacitors, is of current interest. In this regard, a special interest is directed to the study of new methods for the synthesis of nickel microfibers nanostructured materials. The research focuses on the fact that the existing synthesis methods are complicated and require either specialized equipment or a large number of chemical reagents for the synthesis of nickel nanostructured materials. The aim of this work is to determine the influence of the reagents, nickel chloride as an oxidizer and hydrazine hydrate as a reducing agent, on the parameters of nickel microfibers – length and surface development. Using this technique, nickel nanostructured microfibers were obtained depending on the oxidizer concentration. The morphology of the obtained products was characterized by optical microscopy and scanning electron microscopy. It was shown that the morphology of the microfibers changes smoothly with changes of the oxidizer concentration, which provides controllability of the product characteristics, adjustment of the required length of nickel microfibers in the range from 20 to 150 μm . The method of X-ray phase analysis confirmed that the final products of the synthesis are nickel microfibers without any side impurities. The high electrochemical activity of nickel electrodes modified by the synthesized structures in alkaline electrolyte was shown. The results obtained can be used in the electrochemical current sources, including batteries and supercapacitors, as well as in other applications where a developed surface is required, for example, in sensors and catalysis.

Keywords: nickel microfiber; synthesis of nanostructured nickel; nickel chloride; hydrazine hydrate; nickel electrodes; oxidizer concentration; electrochemical activity of the electrode; supercapacitor.

For citation: Morozov MV, Mansurov RN, Drobyshev SV. Synthesis of nickel nanostructured microfibers to increase the electrochemical activity of nickel electrodes. *Journal of Advanced Materials and Technologies*. 2023;8(4):260-269. DOI: 10.17277/jamt.2023.04.pp.260-269

Синтез никелевых наноструктурированных микроволокон для повышения электрохимической активности никелевых электродов

© М. В. Морозов^a✉, Р. Н. Мансуров^b, С. В. Дробышев^a

^a Казанский национальный исследовательский технический университет им. А. Н. Туполева – КАИ,
ул. Карла Маркса, 10, Казань, 423111, Российская Федерация,

^b Институт органической и физической химии имени А. Е. Арбузова КазНЦ РАН,
ул. Академика Арбузова, 8, Казань, 423088, Российская Федерация

✉ misha617@mail.ru

Аннотация: В настоящее время актуальными являются исследования свойств наноструктурированных материалов для электрохимических приложений, в частности, для разработки перспективных суперконденсаторов. В связи с этим особый интерес направлен на исследование новых способов синтеза никелевых микроволоконных наноструктурированных материалов. Проблема исследования заключается в том, что существующие способы синтеза сложны и требуют или специализированного оборудования, или большого количества химических

реактивов для синтеза никелевых наноструктурированных материалов. Цель работы – определение влияния реагентов хлорида никеля в качестве окислителя и гидразингидрата в качестве восстановителя на параметры никелевых микроволокон – длину и развитость поверхности. С помощью данной методики получены никелевые наноструктурированные микроволокна в зависимости от концентрации окислителя. Морфология полученных продуктов охарактеризована методами оптической микроскопии и сканирующей электронной микроскопии. Показано, что морфология микроволокон плавно меняется с изменением концентрации окислителя, что обеспечивает управляемость характеристиками продукта, настройку требуемой длины никелевых микроволокон в диапазоне от 20 до 150 мкм. Методом рентгенофазового анализа подтверждено, что конечными продуктами синтеза являются никелевые микроволокна без каких-либо побочных примесей. Показана высокая электрохимическая активность никелевых электродов, модифицированных синтезированными структурами, в щелочном электролите. Полученные результаты могут быть использованы в электрохимических источниках тока, в том числе аккумуляторах и суперконденсаторах, а также в других приложениях, там, где требуется развитая поверхность, например, в сенсорах и катализе.

Ключевые слова: никелевое микроволокно; синтез наноструктурированного никеля; хлорид никеля; гидразин гидрат; никелевые электроды; концентрация окислителя; электрохимическая активность электрода; суперконденсаторы.

Для цитирования: Morozov MV, Mansurov RN, Drobyshchev SV. Synthesis of nickel nanostructured microfibers to increase the electrochemical activity of nickel electrodes. *Journal of Advanced Materials and Technologies*. 2023;8(4):260-269. DOI: 10.17277/jamt.2023.04.pp.260-269

1. Introduction

The ever-increasing requirements for unique combinations of properties of substances, including thermal and electrical conductivity, strength and ductility, stability and reactivity are the main driving force in the field of architecturing new materials. This necessitates both the synthesis of new materials and the investigation of conditions for the fabrication of new products based on them [1, 2]. In the creation of electrodes for modern chemical sources of current, nickel and nickel-oxide materials for lithium-ion batteries are of particular interest [3–5]. Nanostructuring of nickel materials allows increasing their specific surface area, which is especially important in the development of supercapacitors because it increases their capacity and power [6–15].

The problem with the synthesis of nickel materials with developed surface area is that the existing synthesis methods are complex and require either specialized equipment or a large number of chemical reagents for the synthesis of nickel nanostructured materials, and thus it is a relevant issue. On the other hand, the application of porous electrode frameworks in chemical current sources (CCS) has been efficient. This shows that an important parameter is the particle length, which is necessary to create porous electrode frameworks from these particles, so it is important to learn how to produce long nickel microfibers resistant to alkaline environment. At the same time, the mechanism of synthesis of nanostructured nickel coatings is rather complex, and it is necessary to study reactions with a minimum set of reagents, which will also reduce the

amount of impurities in the synthesized product. Therefore, the aim of this work is to determine the effect of reagents including nickel chloride as an oxidizing agent and hydrazine hydrate as a reducing agent on the parameters of nickel microfibers – length and surface development under the condition of a minimum set of reagents. Next, we consider promising methods for the synthesis of nickel materials requiring a small set of reagents and low temperatures with a developed surface [16–20].

In [18], 80 % $\text{N}_2\text{H}_4 \cdot 6\text{H}_2\text{O}$ solution was mixed into the 1.9 M of NiCl_2 aqueous solution, which led to the formation of Ni complexes between NiCl_2 and N_2H_4 (pale purple precipitate), and the temperature of the solution increased due to the exothermic reaction. These complex compounds that gave this colour were identified as $[\text{Ni}(\text{NH}_3)_6]\text{Cl}_2$ and $[\text{Ni}(\text{N}_2\text{H}_4)_2]\text{Cl}_2$ [21]. It is also known that $[\text{Ni}(\text{NH}_3)_6]\text{Cl}_2$ is formed when $[\text{Ni}(\text{N}_2\text{H}_4)_2]\text{Cl}_2$ is heated to high temperature ($\sim 65^\circ\text{C}$) [22]. The decomposition of Ni complex compounds in a strongly alkaline environment ($\text{pH} \sim 13$) will lead to the formation of $\text{Ni}(\text{OH})_2$ [23, 24], and it can be reduced by N_2H_4 [25–28]. Thus, under the above synthesis conditions, intermediate nickel complexes and nickel hydroxide are formed due to the presence of alkali in the reagents, and excessive amount of hydrazine is needed for its reduction. The final product of the reaction is nickel, and the synthesized nanoparticles are of spherical shape, which is inefficient for the use in CCS.

In [19], a precursor solution was firstly prepared by adding the corresponding NiCl_2 , ammonium

citrate and sodium hydroxide to the reactor. Polyvinylpyrrolidone and silver nitrate were added to the above solution as a protecting agent and nucleating agent to enhance the reaction rate. The reduction reaction took place immediately after the addition of N_2H_4 and precipitation of black Ni particles. The results of X-ray phase analysis showed that nickel hydroxide was formed first and then it was reduced to metallic nickel by N_2H_4 . In view of these experimental results, it is believed that the reactions of $\text{Ni}(\text{OH})_2$ formation and its reduction to nickel particles by hydrazine are two competing reactions [19]. Thus, under these conditions, nickel hydroxide, which is an undesirable reaction product, is also formed, and the shape of nickel particles is spherical, making it inefficient for the application in CCS.

Template-based approaches have been widely used for the synthesis of magnetic metallic micro/nanofibers and wires. Many magnetic metallic fibers have been synthesized using porous anodic aluminium oxide or polycarbonate membrane as matrix [29, 30]. However, this method involves a complex manufacturing process and results in low product yields. Nickel microfiber can also be obtained by oxalate precursor precipitation-thermal decomposition-reduction process using ammonia as a coordinating agent [31]. Obtaining oxalate precursor occurs at high pH (≈ 9), which will lead to equipment deterioration and environmental pollution.

A chemical method for the synthesis of nickel microfibers in an acidic environment can be considered, but this synthesis takes place at high temperature and requires additional equipment, which increases the cost of synthesis [32]. The method of synthesis in an alkaline environment is known [33], but the use of chemical reagents, in addition to oxidizing and reducing agents, in the synthesis of nickel materials leads to the formation of side reactions [18, 19, 25–28]. For example, when NaOH is used, the by-product $\text{Ni}(\text{OH})_2$ appears; this involves an additional amount of hydrazine hydrate, which increases the cost of the synthesis itself. From [34] it is known that surfactants (surfactants) are used in the synthesis of nickel microfibers, but the cost of surfactants is high, which again affects the cost of synthesis of nickel materials. Therefore, the existing synthesis methods do not solve the identified research problem because they are complex and require either specialized equipment or a large number of chemical reagents for the synthesis of nickel nanostructured materials. In order to solve the problem of synthesis of nickel microfibers with developed surface, the present study has been carried out.

2. Materials and Methods

2.1. Synthesis of microfibre structures and electrodes

Nickel microfiber structures were prepared by mixing solutions of NiCl_2 (oxidant) and hydrazine hydrate (reducing agent). Four samples were synthesized using 600, 900, 1200 and 1500 mg of nickel chloride. Nickel (II) chloride was dissolved in 40 mL of water and heated to 60 °C, then hydrazine hydrate solution was injected into the resulting solution dropwise at a rate of $3 \text{ mL} \cdot \text{min}^{-1}$ to form a homogeneous solution obtained by dissolving 5 mL of hydrazine hydrate in 40 mL of distilled water. This reaction solution was thermostated for 40 minutes at 95 °C. After this time, the reaction was stopped, the products were removed from the solution and washed with distilled water several times and dried in an oven at 70 °C for at least 12 hours. Separately, for the samples using 1200 and 1500 mg of nickel chloride, the reaction was carried out with a thermostat time of 60 minutes to determine the completion time of the synthesis under these conditions.

Nickel electrodes modified with nickel microfiber were obtained by mixing solutions of nickel (II) chloride and hydrazine hydrate. 240 mg of nickel (II) chloride was dissolved in 40 mL of water and heated to 60 °C, then an industrial-type porous nickel foil electrode was placed in the solution and hydrazine hydrate solution was injected dropwise at a rate of $3 \text{ mL} \cdot \text{min}^{-1}$ to form a homogeneous solution obtained by dissolving 5 mL of hydrazine hydrate in 40 mL of distilled water. The final solution was thermostated for 1 hour at 95 °C. After one hour, the reaction was stopped and the electrode with nickel microfibers was removed from the solution and washed with distilled water several times and dried in an oven at 70 °C for at least 12 hours.

2.2. Analytic Methods

The morphology of the products obtained during the synthesis, including their overall structure and surface area, was examined by scanning electron microscopy (SEM) on an Auriga Crossbeam workstation (Carl Zeiss, Germany) with a thermal field emission cathode. Also the overall structure of the microfibers was investigated by optical microscopy on an Axio Imager.Z2m microscope (Carl Zeiss, Germany). The phase composition of the products was investigated by X-ray phase analysis on a research grade Shimadzu XRD-7000 X-ray

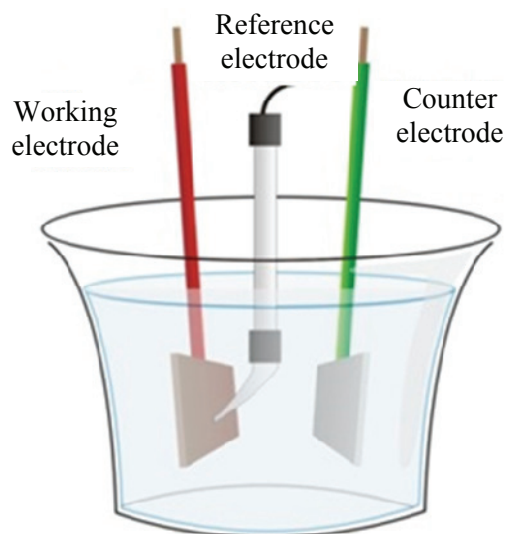


Fig. 1. Three-electrode cell

diffractometer (Shimadzu Corporation, Japan) with a vertical θ - θ goniometer. Energy dispersive X-ray analysis spectra were obtained on the Auriga Crossbeam workstation for elemental analysis of products.

2.3. Electrochemical measurements

A series of cyclic voltammetry experiments were carried out to characterize the relationship between the surface development of the synthesized materials and the electrochemical activity of nickel electrodes modified with the synthesized structures, in alkaline electrolyte. For this purpose, a three-electrode cell setup was used (Fig. 1).

An electrode with synthesized microfiber structures with dimensions of 3×3 cm or a porous

nickel foil electrode of industrial type without microfiber structures was used as a working electrode. A silver chloride electrode was used as a reference electrode and a platinum wire was used as a counter electrode. After that, voltammograms of the electrodes in alkaline electrolyte in 0.1 M caustic potassium solution were taken in the potential range from -1 to 1 V at a sweep speed from 5 to 60 $\text{mV}\cdot\text{s}^{-1}$ on an Autolab PGSTAT302N potentiostat/galvanostat (MetrohmAutolab, Netherlands).

3. Results and Discussion

3.1. Synthesis of nickel microfiber structures at different reagent concentrations

Table 1 shows the optical microscope images of washed and dried microfibers.

The results of the microfiber length study are presented in Table 2.

From the optical microscopy data, it is observed that the length of microfibers decreases with the increasing oxidizer concentration (Table 1). The same is observed visually and shown in Table 2. At lower concentrations of nickel chloride, the fibers grow in solid and large pieces, unlike at higher concentrations [3].

Table 3 shows the SEM images of microfibers in dependence of the oxidizer concentration.

Analyzing the images from Table 3, it can be concluded that with the increase of the oxidizer concentration, the length of microfibers decreases and the obtained structures are agglomerates of particles, which corresponds to the conclusions of [3].

Table 1. Microfiber images obtained using an optical microscope, depending on the mass of the oxidizer

Mass of the oxidizer, mg	Overview	Images of separate fibres
600		


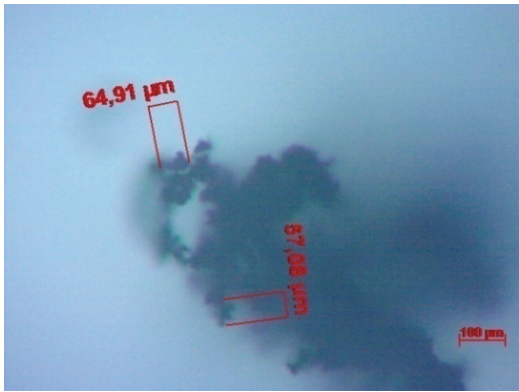
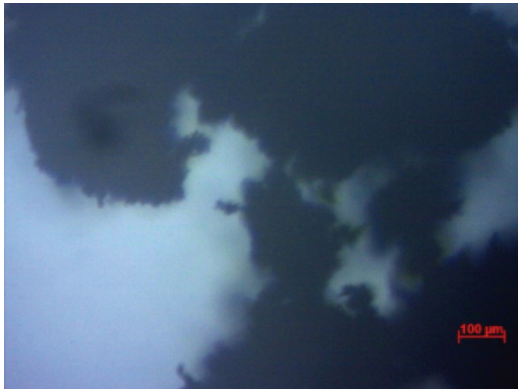
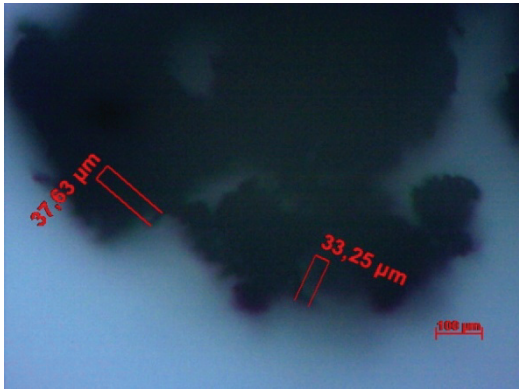

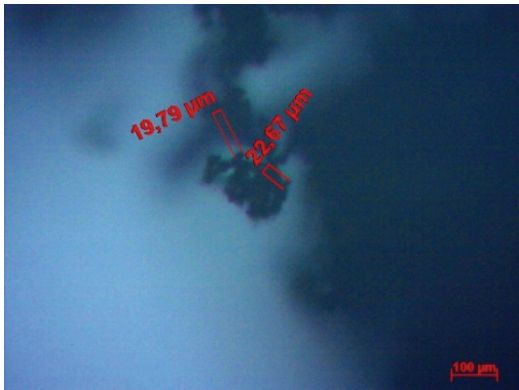
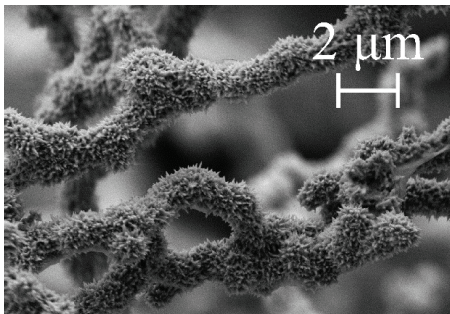
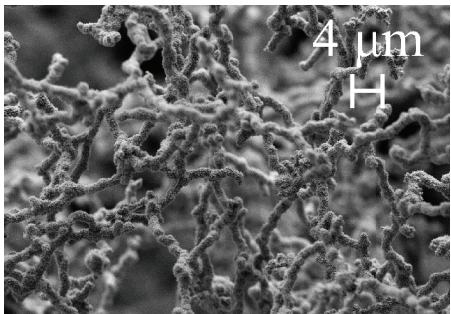
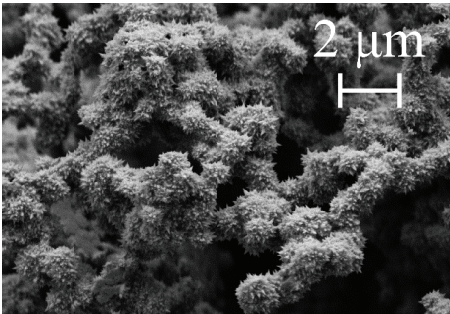
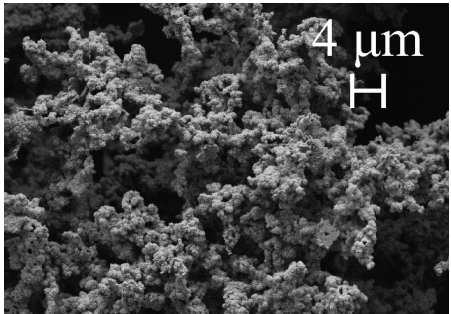
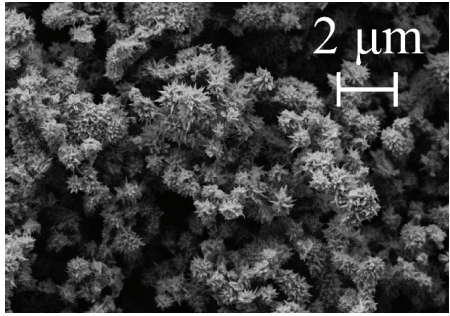
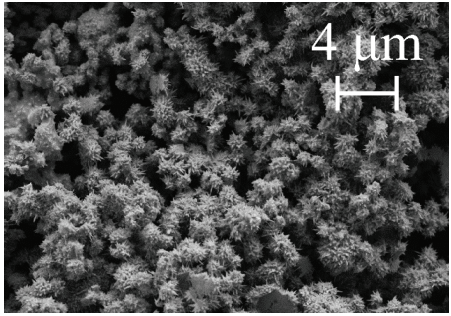
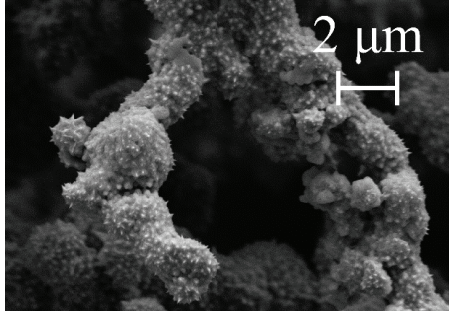
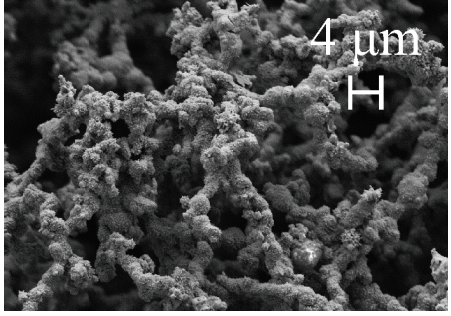
Mass of the oxidizer, mg	Overview	Images of separate fibres
900		
1200		
1500		

Table 2. Results of optical microscopy image analysis

Sample number	Hydrazine hydrate ($\text{N}_2\text{H}_4 \cdot \text{H}_2\text{O}$), mL	Nickel chloride ($\text{N}_2\text{H}_4 \cdot 6\text{H}_2\text{O}$), mg	Microfiber length range, μm
1	5	600	145 ± 10
2		900	65 ± 10
3		1200	38 ± 8
4		1500	22 ± 5

Table 3. SEM images of nickel microfibers, depending on the mass of the reactant

Sample number	Smaller scale image (magnification 20 000)	Larger scale image (magnification 5000)
1		
2		
3		
4		

The synthesized microfibers (Fig. 2) have a developed surface covered with nanospikes, which indicates that their use in supercapacitors is promising [6–15]. The length of the nanospikes as estimated from Fig. 2 is 100–250 nm, and their dimensions in the transverse direction are much smaller than those in the longitudinal direction. Thus, the nanospikes provide a developed surface for electrodes based on synthesized nickel nanostructured microfibers.

In the experiments in which a large amount of oxidant (1200 and 1500 mg) was used, it was observed that some powder inclusions did not react completely and remained after the completion of the synthesis. SEM images show that the inclusions are non-electrically conducting hollow spherical particles (Fig. 3), which appear as a light blue powder in the microfiber structure. Energy dispersive X-ray analysis shows that this substance consists of at least nitrogen, chlorine and nickel (Fig. 4).

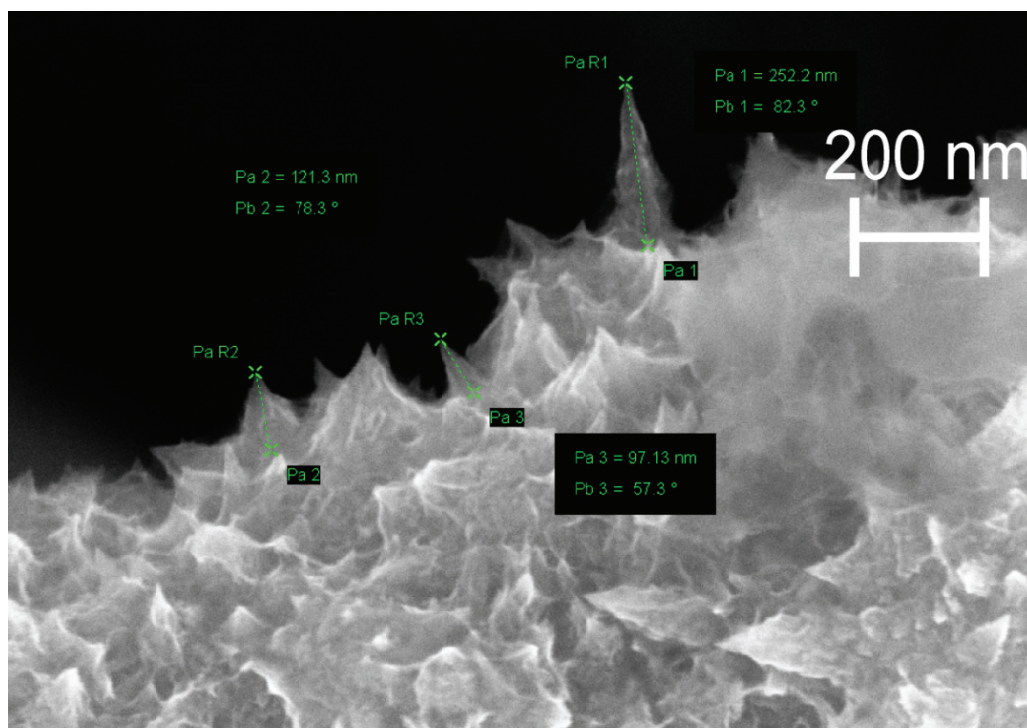


Fig. 2. Enlarged SEM image of the nickel microfibre surface (sample 1, magnification 190 000)

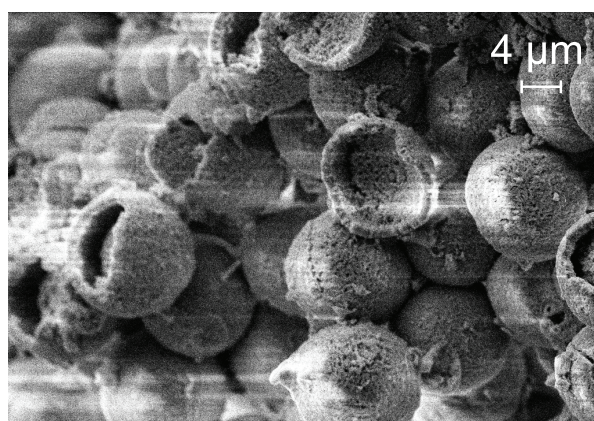


Fig. 3. SEM images of powder inclusions at magnification 7000

Sources [35] indicate that nanostructured nickel is formed by the decomposition of $\text{Ni}(\text{NH}_3)_6\text{Cl}_2$. Presumably, this substance in the form of light blue particles is observed in the obtained SEM images, which is confirmed by the presence of chlorine, nitrogen and nickel in the particles according to the results of energy dispersive X-ray analysis.

To determine the phase composition experiments were repeated with samples 1, 2, 3 and 4 using X-ray phase analysis (XRD). For samples 3 and 4, it was decided to increase the experiment time to complete the synthesis (maintaining at 95 °C for 60 min) and intermediate powder samples were taken to identify the inclusions.

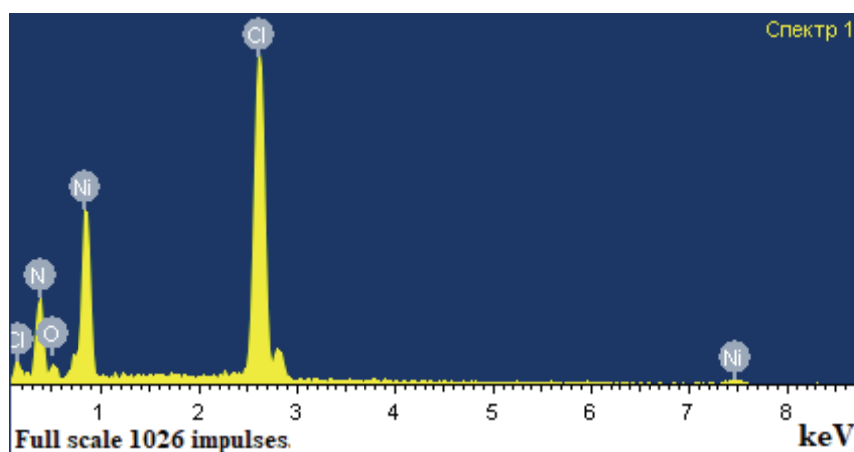


Fig. 4. Results of energy dispersive X-ray spectroscopy of powder inclusions

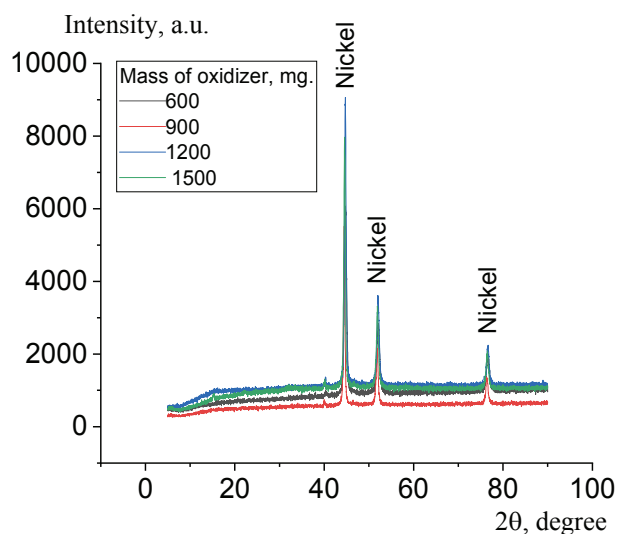


Fig. 5. Diffractogram of samples with different oxidizer mass after the completion of synthesis

As can be seen in Fig. 5, all samples consist of only nanostructured nickel and contain no other phases. Meanwhile, samples 3 and 4 obtained after 1 hour of thermostating at 95 °C do not contain any inclusion.

3.2. Investigation of the electrochemical activity of the synthesised nickel-based electrodes in alkaline electrolyte

Figure 6 shows cyclic voltammetry obtained for nickel foil and electrode with microfiber structures in 0.1 M KOH solution in the potential range $[-1.0-1.0]$ V at potential sweep rate $\nu = 20 \text{ mV}\cdot\text{s}^{-1}$. It was noted in [36] that in the considered potential range nickel oxide NiO and β -nickel hydroxide ($\beta\text{-Ni}(\text{OH})_2$) can be formed. Presumably, the presence of a cathodic peak in the 0.1 V region for the electrode with microfiber structures is because the developed nickel surface is transformed and additional nickel hydroxides are formed on the electrode surface, which can be reduced at the cathodic peak. Accordingly, the more developed the surface is, the more intensive is the process of hydroxide formation [36]. The absence of this peak for nickel foil is explained by the absence of a developed nanostructured surface on it, and microstructured nickel particles are much less susceptible to conversion to hydroxides. It should be noted that the bend on the cyclic voltammetry image at potentials of 1 V and more corresponds to the region of oxygen release, and the bend at potentials less than -1 V corresponds to the region of hydrogen release [36].

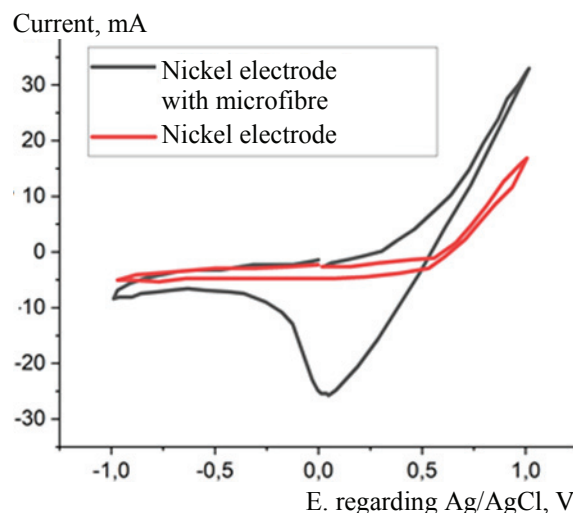


Fig. 6. Cyclic voltammograms obtained for nickel foil and electrode with microfiber structures in 0.1 M KOH solution in the range of potentials $[-1.0-1.0]$ V at the potential sweep rate $\nu = 20 \text{ mV}\cdot\text{s}^{-1}$

4. Conclusion

In this work, the synthesis of nickel nanostructured microfibers was carried out at different concentrations of reagents. The synthesis of coatings was carried out using a technique with a minimum set of initial reagents to reduce the cost of synthesis technology and avoid the occurrence of residual impurities. To obtain nickel materials with developed surface using the proposed methodology, it is necessary to carry out the synthesis for at least one hour. The hydrazine hydrate solution should be added dropwise at a rate of $3 \text{ mL}\cdot\text{min}^{-1}$ to create a homogeneous solution. By methods of optical microscopy and scanning electron microscopy the morphology of the obtained intermediate and final products of synthesis was investigated. It was found that a decrease in oxidant concentration is required to increase the length of the microfibers, which provides length tuning in the range from 20 to 150 μm . It was confirmed by X-ray phase analysis that the final products of the synthesis are nickel microfibers. The electrochemical activity of nickel foil electrodes modified by the synthesized structures exceeds the activity of the original foil electrodes by about five times. In the future it is planned to investigate in detail the electrochemical activity of the synthesized structures, to determine the optimal synthesis conditions and to develop a method of creating supercapacitor electrodes with nickel nanostructured materials. Also, the results obtained can be used in the creation of batteries, as well as in other applications, where a developed surface is required, for example, in sensors and catalysis.

5. Funding

The study was funded by the government assignment for the Federal Research Center “Kazan Scientific Center of the Russian Academy of Sciences”.

6. Conflict of interests

The authors declare no conflict of interests.

References

1. Török TI, Pázmán J, Szabó M, et al. Laboratory preparation and characterization of electroless nickel coated powders of industrially produced aluminium and iron(III) oxides. *Materials Science Forum*. 2013;752:284-293. DOI:10.4028/www.scientific.net/msf.752.284
2. Gromov AA, Nalivaiko AY, Ambaryan GN, et al. Aluminum–alumina composites: Part 1: Obtaining and characterization of powders. *Materials*. 2019;12(19):3180. DOI:10.3390/ma12193180
3. Morozov M, Ivanov S, Kadirov M, et al. Facile synthesis of a binder-free 3D Ni/NiO microwire network with a nanostructured fiber surface for a negative electrode in Li-ion battery. *Journal of Applied Electrochemistry*. 2021;51(5):815-828. DOI:10.1007/s10800-021-01541-5
4. Liu C, Li C, Ahmed K, et al. Template free and binder less NiO nanowire foam for Li-ion battery anodes with long cycle life and ultrahigh rate capability. *Scientific Reports*. 2016;6(1). DOI:10.1038/srep29183
5. Holzer L, Iwanschitz B, Hocker T, et al. Microstructure degradation of cermet anodes for solid oxide fuel cells: Quantification of nickel grain growth in dry and in humid atmospheres. *Journal of Power Sources*. 2011;196(3):1279-1294. DOI:10.1016/j.jpowsour.2010.08.017
6. Nam K-W, Kim K-H, Lee E-S, et al. Pseudocapacitive properties of electrochemically prepared nickel oxides on 3-dimensional carbon nanotube film substrates. *Journal of Power Sources*. 2008;182(2):642-652. DOI:10.1016/j.jpowsour.2008.03.090
7. Wu M-S, Hsu W-H. Nickel nanoparticles embedded in partially graphitic porous carbon fabricated by direct carbonization of nickel-organic framework for high-performance supercapacitors. *Journal of Power Sources*. 2015;274:1055-1062. DOI:10.1016/j.jpowsour.2014.10.133
8. Yuan G- hui, Jiang Z- hua, Aramata A, et al. Electrochemical behavior of activated-carbon capacitor material loaded with nickel oxide. *Carbon*. 2005;43(14): 2913-2917. DOI:10.1016/j.carbon.2005.06.027
9. Cheng Y-K, Zhang F, Tang L-L, et al. Pregnancy associated nasopharyngeal carcinoma: A retrospective case-control analysis of maternal survival outcomes. *Radiotherapy and Oncology*. 2015;116(1):125-130. DOI:10.1016/j.radonc.2015.06.008
10. Dong S, Ji X, Yu M, et al. Direct synthesis of interconnected porous carbon nanosheet/nickel foam composite for high-performance supercapacitors by microwave-assisted heating. *Journal of Porous Materials*. 2017;25(3):923-933. DOI:10.1007/s10934-017-0504-0
11. Liu Y, Lu Q, Huang Z, et al. Electrodeposition of Ni–Co–S nanosheet arrays on N-doped porous carbon nanofibers for flexible asymmetric supercapacitors. *Journal of Alloys and Compounds*. 2018;762:301-311. DOI:10.1016/j.jallcom.2018.05.239
12. Nagaraju G, Cha SM, Yu JS. Ultrathin nickel hydroxide nanosheet arrays grafted biomass-derived honeycomb-like porous carbon with improved electrochemical performance as a supercapacitive material. *Scientific Reports*. 2017;7(1). DOI:10.1038/srep45201
13. Wu M-S, Zheng Z-B, Lai Y-S, et al. Nickel cobaltite nanograss grown around porous carbon nanotube-wrapped stainless steel wire mesh as a flexible electrode for high-performance supercapacitor application. *Electrochimica Acta*. 2015;182:31-38. DOI:10.1016/j.electacta.2015.09.049
14. Feng J, Zhao J, Tang B, et al. The electrochemical performance of ordered mesoporous carbon/nickel compounds composite material for supercapacitor. *Journal of Solid State Chemistry*. 2010;183(12):2932-2936. DOI:10.1016/j.jssc.2010.09.043
15. Yang H-X, Zhao D-L, Meng W-J, et al. Nickel nanoparticles incorporated into N-doped porous carbon derived from N-containing nickel-MOF for high-performance supercapacitors. *Journal of Alloys and Compounds*. 2019;782:905-914. DOI:10.1016/j.jallcom.2018.12.259
16. Muench F, Oezaslan M, Rauber M, et al. Electroless synthesis of nanostructured nickel and nickel–boron tubes and their performance as unsupported ethanol electrooxidation catalysts. *Journal of Power Sources*. 2013;222:243-252. DOI:10.1016/j.jpowsour.2012.08.067
17. Zhao X, Muench F, Schaefer S, et al. Electroless decoration of macroscale foam with nickel nano-spikes: A scalable route toward efficient catalyst electrodes. *Electrochemistry Communications*. 2016;65:39-43. DOI:10.1016/j.elecom.2016.02.002
18. Choi J-Y, Lee Y-K, Yoon S-M, et al. A chemical route to large-scale preparation of spherical and monodisperse Ni powders. *Journal of the American Ceramic Society*. 2005;88(11):3020-3023. DOI:10.1111/j.1551-2916.2005.00582.x
19. Chou L-H, Hung W-C, Lee M-T. On the preparation of nickel nanoparticles by chemical reduction method: X-ray absorption spectroscopy. *Materials Science*. 2016;22(2). DOI:10.5755/j01.ms.22.2.12921
20. Eluri R, Paul B. Synthesis of nickel nanoparticles by hydrazine reduction: mechanistic study and continuous flow synthesis. *Journal of Nanoparticle Research*. 2012;14(4). DOI:10.1007/s11051-012-0800-1
21. Nicholls D, Swindells R. Hydrazine complexes of nickel(II) chloride. *Journal of Inorganic and Nuclear Chemistry*. 1968;30(8):2211-2217. DOI:10.1016/0022-1902(68)80219-2
22. Guo L, Liu C, Wang R, et al. Large-scale synthesis of uniform nanotubes of a nickel complex by a solution chemical route. *ChemInform*. 2004;35(25). DOI:10.1002/chin.200425241
23. Li Y, Li C, Wang H, et al. Preparation of nickel ultrafine powder and crystalline film by chemical control

reduction. *Materials Chemistry and Physics*. 1999;59(1):88-90. DOI:10.1016/s0254-0584(99)00015-2

24. Gao J, Guan F, Zhao Y, et al. Preparation of ultrafine nickel powder and its catalytic dehydrogenation activity. *Materials Chemistry and Physics*. 2001;71(2): 215-219. DOI:10.1016/s0254-0584(01)00275-9

25. Chen D-H, Wu S-H. Synthesis of Nickel Nanoparticles in Water-in-Oil Microemulsions. *Chemistry of Materials*. 2000;12(5):1354-1360. DOI:10.1021/cm991167y

26. Boudjahem A-G, Monteverdi S, Mercy M, et al. Study of support effects on the reduction of Ni^{2+} ions in aqueous hydrazine. *Langmuir*. 2003;20(1):208-213. DOI:10.1021/la035120

27. Zheng H-G, Liang J-H, Zeng J-H, et al. Preparation of nickel nanopowders in ethanol-water system (EWS). *Materials Research Bulletin*. 2001;36(5):947-952. DOI:10.1016/s0025-5408(01)00569-4

28. Park JW, Chae EH, Kim SH, et al. Preparation of fine Ni powders from nickel hydrazine complex. *Materials Chemistry and Physics*. 2006;97(2):371-378. DOI:10.1016/j.matchemphys.2005.08.028

29. Qiao L, Han X, Gao B, et al. Microwave absorption properties of the hierarchically branched Ni nanowire composites. *Journal of Applied Physics*. 2009;105(5): 053911. DOI:10.1063/1.3081649

30. Xue S, Li M, Wang Y, et al. Electrochemically synthesized binary alloy FeNi nanorod and nanotube arrays in polycarbonate membranes. *Thin Solid Films*. 2009;517(20):5922-5926. DOI:10.1016/j.tsf.2007.08.011

31. Okamoto T, Ichino R, Okido M, et al. Effect of ammonia on the crystal morphology of nickel oxalate

precipitates and their thermal decomposition into metallic nickel. *Materials Transactions*. 2005;46(2):171-174. DOI:10.2320/matertrans.46.171

32. Zhang C, Yao Y, Zhan J, et al. Template-free synthesis of Ni microfibres and their electromagnetic wave absorbing properties. *Journal of Physics D: Applied Physics*. 2013;46(49):495308. DOI:10.1088/0022-3727/46/49/495308

33. Zhang X, Zhang Z, Han X. Synthesis of coral-like nickel nanocrystallites via a dipolar-interaction-directed self-assembly process. *Journal of Crystal Growth*. 2005;274(1):113-117. DOI:10.1016/j.jcrysgro.2004.09.075

34. Niu H, Chen Q, Ning M, et al. Synthesis and one-dimensional self-assembly of acicular nickel nanocrystallites under magnetic fields. *The Journal of Physical Chemistry B*. 2004;108(13):3996-3999. DOI:10.1021/jp0361172

35. Yue HY, Song SS, Huang S, et al. Preparation of three-dimensional hollow graphene balls and simultaneous electrochemical determination of dopamine and uric acid. *Journal of Materials Science: Materials in Electronics*. 2018;29(14):12330-12339. DOI:10.1007/s10854-018-9346-z

36. Oshchepkov AG, Bonnefont A, Pronkin SN, et al. Nanostructured nickel nanoparticles supported on vulcan carbon as a highly active catalyst for the hydrogen oxidation reaction in alkaline media. *Journal of Power Sources*. 2018;402:447-452. DOI:10.1016/j.jpowsour.2018.09.051

Information about the authors / Информация об авторах

Mikhail V. Morozov, Cand. Sc. (Eng.), Associate Professor, Department of the Nanotechnology in Electronics, Kazan National Research Technical University named after A.N. Tupolev – KAI (KNRTU-KAI), Kazan, Russian Federation; ORCID 0000-0003-1434-830X; e-mail: misha617@mail.ru

Ravil N. Mansurov, Junior Researcher, A.E. Arbuzov Institute of Organic and Physical Chemistry, Kazan, Russian Federation; ORCID 0000-0002-4003-0525; e-mail: ravil545@bk.ru

Sergey V. Drobyshev, Assistant, Department of the Nanotechnology in Electronics, KNRTU-KAI, Kazan, Russian Federation; ORCID 0000-0002-1655-4492; e-mail: warlordik_009@mail.ru

Морозов Михаил Валерьевич, кандидат технических наук, доцент кафедры «Нанотехнологии в электронике (НТвЭ)», Казанский национальный исследовательский технический университет им. А. Н. Туполева – КАИ (КНИТУ-КАИ), Казань, Российская Федерация; ORCID 0000-0003-1434-830X; e-mail: misha617@mail.ru

Мансуров Равиль Нафисович, младший научный сотрудник, Институт органической и физической химии имени А. Е. Арбузова КазНЦ РАН, Казань, Российская Федерация; ORCID 0000-0002-4003-0525; e-mail: ravil545@bk.ru

Дробышев Сергей Викторович, ассистент, кафедра НТвЭ, КНИТУ-КАИ, Казань, Российская Федерация; ORCID 0000-0002-1655-4492; e-mail: warlordik_009@mail.ru

Received 16 August 2023; Accepted 28 September 2023; Published 15 December 2023



Copyright: © Morozov MV, Mansurov RN, Drobyshev SV, 2023. This article is an open access article distributed under the terms and conditions of the Creative Commons Attribution (CC BY) license (<https://creativecommons.org/licenses/by/4.0/>).

Promising sorbents based on compacted highly porous carbon materials

© Igor N. Shubin^a✉, Elina S. Mkrtchyan^a, Oksana A. Ananyeva^a

^a Tambov State Technical University, Bld. 2, 106/5, Sovetskaya St., Tambov, 392000, Russian Federation

✉ i.shubin77@yandex.ru

Abstract: The paper considers the stages of preparing a compacted highly porous carbon material (HPCM), which involves alkaline high-temperature activation of the initial carbonizate at a temperature of 400–7500 °C for a duration of 2 hours. As a result of activation, a material was produced with a specific surface area of 2600–2700 m²·g⁻¹ and a pore volume of more than 1.3 cm³·g⁻¹. The activated material was compacted using binders, which were basalt fiber (HPCM/BF), polyvinyl alcohol (HPCM/PVA) and polyvinyl acetate (HPCM/PVAC). Conditions for compacting were as follows: pressure in the range from 25 to 1600 kgf·cm⁻², temperature 75–1900 °C and duration between 30 and 150 minutes. As a result, the compacted material had a specific surface area of 1550–2000 m²·g⁻¹ and a specific pore volume of 0.693–0.849 cm³·g⁻¹. For the final samples, the sorption capacity for molecules of the organic dye methylene blue (MB) was determined. The kinetic studies showed that the absorptive capacity of the initial material HPCM was 1691 mg·g⁻¹, while that of compacted samples of HPCM/PVAC, HPCM/BF and HPCM/PVA was 1611, 1000, and 1270 mg·g⁻¹, respectively. In this case, the time for the onset of adsorption equilibrium was 15 min. The presented results show that the compacted carbon material can be a promising sorbent of organic pollutants from aqueous solutions.

Keywords: highly porous carbon material; compaction; specific surface area; adsorption; methylene blue; kinetics.

For citation: Shubin IN, Mkrtchyan ES, Ananyeva OA. Promising sorbents based on compacted highly porous carbon materials. *Journal of Advanced Materials and Technologies*. 2023;8(4):270-278. DOI: 10.17277/jamt.2023.04.pp.270-278

Перспективные сорбенты на основе компактированного высокопористого углеродного материала

© И. Н. Шубин^a✉, Э. С. Мкртчян^a, О. А. Ананьева^a

^a Тамбовский государственный технический университет,
ул. Советская, 106/5, пом. 2, Тамбов, 392000, Российская Федерация

✉ i.shubin77@yandex.ru

Аннотация: Рассмотрены этапы получения компактированного высокопористого углеродного материала (ВУМ), предусматривающие проведение щелочной высокотемпературной активации исходного карбонизата при температуре 400...750 °C продолжительностью 2 ч. В результате активации получен материал, обладающий удельной поверхностью 2600...2700 м²/г и объемом пор более 1,3 см³/г. Активированный материал компактирован с применением связующих, в качестве которых использовались базальтовое волокно (ВУМ/БВ), поливиниловый спирт (ВУМ/ПВС) и поливинилацетат (ВУМ/ПВА). Условия проведения компактирования – давление прессования в диапазоне от 25 до 1600 кгс/см², температура 75...190 °C и продолжительность от 30 до 150 мин. В результате компактированный материал обладал удельной поверхностью 1550...2000 м²/г и удельным объемом пор 0,693...0,849 см³/г. Для конечных образцов определена сорбционная емкость по молекулам органического красителя метиленового синего (МС). В результате кинетических исследований выявлена поглотительная способность как исходного материала ВУМ – 1691 мг/г, так и компактированных образцов ВУМ/ПВС – 1611 мг/г, ВУМ/БВ – 1000 мг/г, ВУМ/ПВА – 1270 мг/г. При этом время наступления адсорбционного равновесия составило ≈ 15 мин. Представленные результаты показывают, что компактированный углеродный материал может являться перспективным сорбентом органических загрязнителей из водных растворов.

Ключевые слова: высокопористый углеродный материал; компактирование; удельная площадь поверхности; адсорбция; метиленовый синий; кинетика.

Для цитирования: Shubin IN, Mkrtchyan ES, Ananyeva OA. Promising sorbents based on compacted highly porous carbon materials. *Journal of Advanced Materials and Technologies*. 2023;8(4):270-278. DOI: 10.17277/jamt.2023.04.pp.270-2780

1. Introduction

The development and study of promising highly porous carbon materials with a large specific surface and porosity with a predominance of micro- and mesopores are of interest for many studies, the results of which are in demand in a number of branches of modern industry. These materials seem to be the most promising as universal sorbents for various liquid and gaseous media, devices for storing and transporting fuel, as catalysts, fertilizer carriers, fuel cells, as well as solving environmental problems in such industries as petrochemistry, power engineering, radio electronics, medicine, and agriculture. This is explained primarily by the presence of a balanced combination of a developed system of micro- and mesopores, with a significant specific surface area, corresponding accessible pores and their large volume, with the presence of sufficiently large transport pores that ensure rapid diffusion of sorbed substances, chemical inertness, and stability under real conditions of the use of such materials [1–4].

To produce highly porous carbon materials, various pre-carbonized initial carbon raw materials, including phenol-formaldehyde resin, hydroquinone, carboxymethylcellulose, natural coals, furfural, dextrin, urotropine, carbon nanotubes, graphene, or their combinations are activated with various gas-phase or liquid-phase reagents, such as various acids or alkalis, water vapor, etc. [5–11].

Thus, the authors in [12–16] conducted a study of the impact of activation parameters of the initial carbon raw material and the modes of its subsequent compaction on the sorption characteristics of a highly porous carbon material (HPCM), noting their direct relationship and the possibility of scaling the results of laboratory studies in relation to the possibilities of real production.

The use of graphene in the preparation of a highly porous carbon material with a hierarchical pore structure for potential applications in electronics, catalysis, and sorption is the subject of studies [17], where the authors pointed out the promise of the obtained materials, the presence of a significant surface area, and the possibility of chemical doping and functionalization.

The evaluation of the adsorption properties of highly porous materials with the determination of

their structural characteristics was the subject of research in [18, 19], which considered the mechanisms of adsorption and phase behavior of liquids in ordered nanoporous materials with a well-defined pore structure and prove the importance of studying these mechanisms for improving the characteristics of physical adsorption.

The activation process aimed at increasing and improving the volume of micropores, while maintaining a clear network of mesopores was studied in [20]. It was proven that the applied activator – potassium hydroxide – had the biggest impact on the material characteristics, directly contributing to an increase in the volume of micropores. It was shown that alkaline activation is a suitable method for increasing the adsorption capacity of carbon while maintaining a mesoporous structure.

The study of microporous carbon modified with organic substances as fillers to improve thermal and mechanical properties was conducted in [21]. The prepared sorption material showed a significant increase in characteristics when used in thin-film composite direct osmosis membranes.

The prepared highly porous carbon materials can be used in various forms: in the form of powder, granules, films or fibers, both for absorption, separation, purification of various liquid and gaseous substances, and as carriers for catalysts, medicines, etc. However, high requirements are often imposed on them in terms of the possibility of molding into blocks or granules for the convenience of further use in finished products and improvement of its sorption characteristics [22–26].

They are a type of materials with a high specific surface area, large pore volume, and a hierarchical porous structure [27]; they are environmentally friendly, economical, nontoxic, and selective, which makes them good candidates for adsorption of organic and inorganic pollutants from aqueous media, including heavy metals and dyes [28, 29]. They can also be used for drug delivery, catalysis, storage and transportation of gaseous media, ecology, etc. [30].

In modern industry, various dyes are widely used, one of the most common representatives of which is methylene blue (MB), which has the chemical formula $C_{16}H_{18}ClN_3S$, which is a representative of the group of quinoneimine dyes

Table 1. Comparative characteristics of MB dye molecules on various carbon nanomaterials

Adsorbent	pH	Experiment conditions		Time, min	Adsorption capacity, $\text{mg}\cdot\text{g}^{-1}$	Ref.
		Initial concentration, $\text{mg}\cdot\text{L}^{-1}$	Sorbent weight, g			
Nanocomposite of saponified polymethyl acrylate with grafted dextrin with embedded nanosilica	7.5	–	20 mg	45	515.40	[36]
Activated charcoal from seed husks	–	316	0.055	19.3	436.68	[37]
Nickel alginate aerogel/activated carbon	–	1000	10 mg	48 h	465.12	[38]
Activated charcoal derived from corn stalks	11	10	1.4	50	90 %	[39]
Activated charcoal made from olive pits	10	–	0.05	24 h	714	[40]
Biochar obtained from leaf litter by slow pyrolysis	12	–	–	–	101.27	[41]
Activated charcoal from walnut shell	–	50	10 mg	540	632	[42]
Activated carbon/cellulose	6.9	100	–	24 h	103.66	[43]
Activated charcoal from barley husks	8	50	0.2	180	61.60	[44]

containing a phenothiazine ring [31]. MB is a cationic dye that is not considered highly toxic to human health at low doses and short-term contact [32]. However, long-term exposure or high levels of MB in water can cause detrimental effects on human health. The toxic effects of methylene blue include permanent damage to human eyes, nausea, diarrhea, skin irritation, and possibly cancer [33, 34]. In connection with the development of anthropogenic activities, a large number of toxic contaminants, including the MB dye, affect the environment due to improper disposal of wastewater from various enterprises. In this regard, the problem of purification of aqueous media from industrial dyes, including MB, the decomposition process of which is very complicated, becomes especially urgent [35].

Currently, materials that are used as sorbents for these purposes and their characteristics are presented in Table 1.

On the basis of preliminary studies, the authors of the paper developed and investigated a compacted highly porous carbon material to solve this environmental problem.

Thus, the purpose of this paper is to study the sorption characteristics of a compacted highly porous carbon material with respect to the organic dye MB.

2. Materials and Methods

2.1. Reagents and method for preparing a compacted highly porous carbon material

At the first stage of research aimed at obtaining a compacted highly porous carbon material, the issues of chemical activation were worked out, which made it possible to determine rational operating parameters and materials: the initial carbon raw material for carbonizate is a mixture of dextrin (Dekstrinzavod CJSC, Murom, Russia) and graphene oxide (Nanotechcenter Ltd., Tambov, Russia), an activator is potassium hydroxide (RM Engineering, Moscow, Russia), the ratio of components of the reaction mixture of carbonizate was potassium hydroxide: 1 : 3, activation temperature range 400–750 °C, the duration of the main stage was 2 hours [7, 9].

Basalt fiber (HPCM/BF) (Kamenny Vek Ltd., Dubna, Russia) in the amount of 1–10%, polyvinyl alcohol (HPCM/PVA) (TK Spektr-Khim, Moscow, Russia) and polyvinyl acetate (HPCM/PVAC) (JSC Pigment, Tambov, Russia) – 10–30 % were used as a binder.

2.2. Characterization

The diagnostics of the characteristics of the activated carbon material before compaction, i.e., its specific surface area and porosity, was carried out on the analytical complex Nova Quantachrome E1200 (Quantachrome, Boynton Beach, USA). As a result, a material was obtained with a specific surface area of 2600–2700 m²·g⁻¹ and a pore volume of more than 1.3 cm³·g⁻¹ [7, 9].

2.3. Adsorption studies

To analyze the efficiency of sorption of the synthetic organic MB dye on compacted carbon sorbents, batch experiments were carried out. The sorbent weighing 0.01 g was placed in 30 mL of MB solution with $C_0 = 1500 \text{ mg} \cdot \text{L}^{-1}$ according to the Russian standard 4453-74. Each test tube with the solutions to be purified and the sorbent was continuously shaken on a programmable rotator Multi Bio RS-24 (Biosan, Riga, Latvia) for 5, 15, 30, and 60 min. The equilibrium C_e concentration of MB molecules was determined from the optical density measured on a PE-5400V spectrophotometer (Ekros, St. Petersburg, Russia) at a wavelength of $\lambda = 815 \text{ nm}$.

The static sorption capacity of Q_e sorbents, $\text{mg} \cdot \text{g}^{-1}$, was calculated by the formula:

$$Q_e = \frac{(C_0 - C_e)V}{m}, \quad (1)$$

where C_0 and C_e are initial and final concentrations of substances in solution, $\text{mg} \cdot \text{L}^{-1}$; V is the volume of the solution, L; m is the sorbent sample weight, g.

2.4. Compaction of activated carbon material

For compaction of the activated carbon material, a laboratory setup was developed based on the “IP 100 M – Auto” testing press (Plant of testing instruments and equipment “ZIPO”, Armavir, Russia) (Fig. 1).

During this stage, compaction modes were investigated; they included several series of experiments with different pressing pressures, temperatures, and process durations. The amount of the binder was established as a result of preliminary studies by the authors and analysis of literary sources.

For the next stage of research (determination of sorption activity), the samples prepared under the compaction parameters given in Table 2 were used.

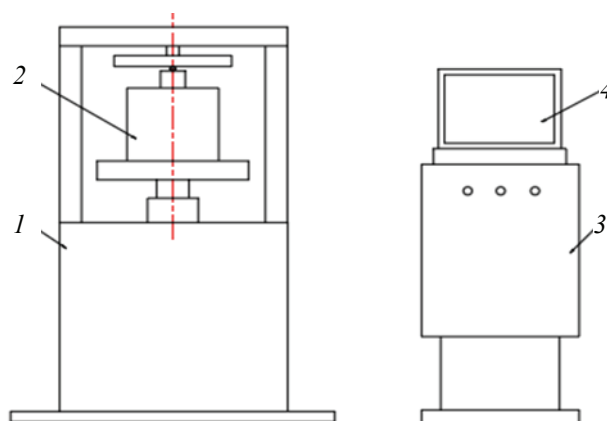


Fig. 1. Laboratory setup for studying the compaction modes of a highly porous carbon material:
1 – press; 2 – heated mold; 3 – press control cabinet; 4 – monitor for setting and displaying the operating modes

Table 2. Compaction mode parameters and characteristics of the prepared samples (blocks)

Parameter	Composites		
	HPCM/PVA	HPCM/BF	HPCM/PVAC
Step wise heating and pressing	75 °C, 3.5 kN, for 15 min	75 °C, 3.5 kN, for 15 min	75 °C, 1.5 kN, for 1 min
	90 °C, 7.5 kN, for 60 min	90 °C, 7.5 kN, for 60 min	90 °C, 3.5 kN, for 1 min
	120 °C, 7.5 kN, for 60 min	120 °C, 7.5 kN, for 60 min	130 °C, 7.5 kN, for 1 min
	190 °C, kN, for 120 min	190 °C, kN, for 120 min	
Mold cooling and pressing-off	Up to 40–50 °C	Up to 40–50 °C	Up to 40–50 °C, placing the sample in an oven for 120 min at a temperature of 80 °C
Block weight, g	16.3–16.8	24.5–25.5	32–33
Height × diameter, mm	(24.5–25.5) × 40	(24–25) × 40	(33–234) × 40

3. Results and Discussion

3.1. Finding specific surface area and porous structure parameters

The resulting compacted carbon materials had the following characteristics: specific surface area 1550–2000 $\text{m}^2\cdot\text{g}^{-1}$, specific micropore volume 0.693–0.849 $\text{cm}^3\cdot\text{g}^{-1}$.

An analysis of the causes of the difference in the physical and structural characteristics of the resulting materials requires additional research and the accumulation of experimental data, since the mechanism of the binder impact on the carbon material is not fully understood at the moment. At the same time, the authors are inclined to believe that polymeric binders (PVA and PVAC) form a certain spatial structure that provides relatively good permeability and contact surface of the block. In the case of a fiber (BF), it is assumed that a rigid spatial framework is formed in a compacted sample, practically without transport pores.

At the same time, the parameters of compacted materials confirm the correctness and promise of this line of research and can be considered a starting point for further work within this stage, which involves further testing of the pressing parameters and the study of binders, including combinations of polymers with fibers.

3.2. Kinetic studies

As a result of kinetic studies in a static mode, graphs of the dependences of the adsorption capacity of the synthesized materials on the time of contact with a pollutant, the MB dye, were plotted (Fig. 2).

As a result of kinetic studies, it was found that the initial HPCM has an absorption capacity of 1691 $\text{mg}\cdot\text{g}^{-1}$ when removing MB dye molecules. When a binding agent is added, the compacted carbon sorbent

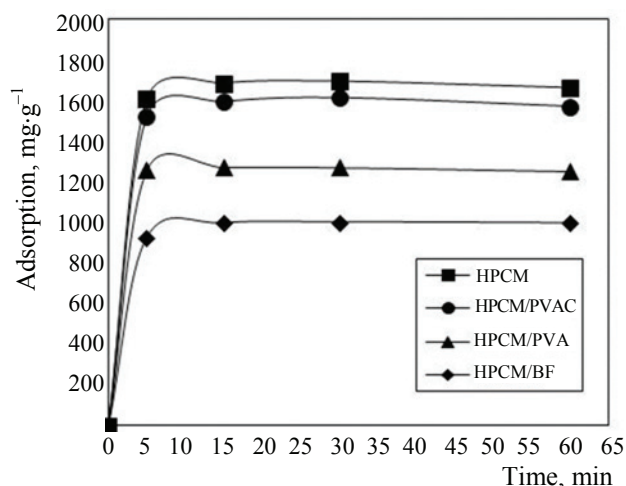


Fig. 2. Adsorption kinetics of MB dye molecules on compacted carbon sorbents HPCM, HPCM/PVA, HPCM/PVAC, HPCM/BF

HPCM/PVA exhibits the highest absorption capacity – 1611 $\text{mg}\cdot\text{g}^{-1}$. In turn, when using basalt fiber (HPCM/BF) and polyvinyl acetate (HPCM/PVAC), the adsorption capacity is 1000 and 1270 $\text{mg}\cdot\text{g}^{-1}$, respectively.

To describe the process of sorption of MB molecules (Table 3), namely, the mechanisms involved in the transfer of sorbate to the surface and inside the structure of sorbents, the obtained experimental data were processed by equations of known kinetic models (equations of pseudo-first and pseudo-second order, the Elovich equation and the intraparticle diffusion equation) [45].

The pseudo-second order model has high correlation coefficients $R^2 = 0.9999$ for all compacted carbon sorbents HPCM, HPCM/PVA, HPCM/PVAC, HPCM/BF. Accordingly, we can conclude that the reaction between the adsorbate and the functional groups of the sorbent proceeds strictly stoichiometrically (one molecule occupies one

Table 3. Description of the sorption process of MB dye molecules

Sorbents	Pseudo-first order			Pseudo-second order		
	$\log(Q_e - Q_t) = \log Q_e - \frac{k_1}{2.303} t$			$\frac{t}{Q_t} = \frac{1}{k_2 Q_e^2} + \frac{1}{Q_e} t$		
	Q_e	k_1	R^2	Q_e	k_2	R^2
HPCM	362	−0.0014	0.1387	1666	0.0120	0.9999
HPCM/PVA	400	−0.0062	0.4072	1666	0.0018	0.9999
HPCM/PVAC	232	0.0009	0.3039	1250	−0.0032	0.9999
HPCM/BF	141	−0.0066	0.3716	1000	0.0050	0.9999

Sorbents	Elovich equation			Intraparticle diffusion equation		
	$Q_t = \frac{1}{\beta} \ln(\alpha\beta) + \frac{1}{\beta} \ln t$			$Q_t = k_{id} t^{0.5} + C$		
	α	β	R^2	k_{id}	C	R^2
HPCM	$40,28 \cdot 10^{36}$	0.0478	0.3859	6.9197	1616.4	0.2519
HPCM/PVA	$22,95 \cdot 10^9$	0.0136	0.7397	28.866	1516.4	0.564
HPCM/PVAC	$96,65 \cdot 10^{13}$	-0.4771	0.0559	-1.6535	1270.0	0.1711
HPCM/BF	$11,72 \cdot 10^{14}$	0.0351	0.7113	11.113	925.43	0.5335

Note: Q_e is the number of adsorbed dye molecules on the adsorbent surface at the moment of equilibrium, $\text{mg} \cdot \text{g}^{-1}$; Q_t is the number of adsorbed dye molecules on the surface of the adsorbent at time t , $\text{mg} \cdot \text{g}^{-1}$; k_1 is the pseudo-first order adsorption rate constant, min^{-1} ; k_2 is the pseudo-second order adsorption rate constant, $\text{g} \cdot (\text{mg} \cdot \text{min})^{-1}$; α is the constant adsorption constant, $(\text{min} \cdot \text{mg} \cdot \text{g}^{-1})^{-1}$; β is the degree of surface coverage and chemisorption activation energy, $\text{g} \cdot \text{mg}^{-1}$; k_{id} is the internal diffusion coefficient, $(\text{mg} \cdot (\text{g} \cdot \text{min})^{-1})^{-1}$; C is the thickness of the boundary layer, $\text{mg} \cdot \text{g}^{-1}$.

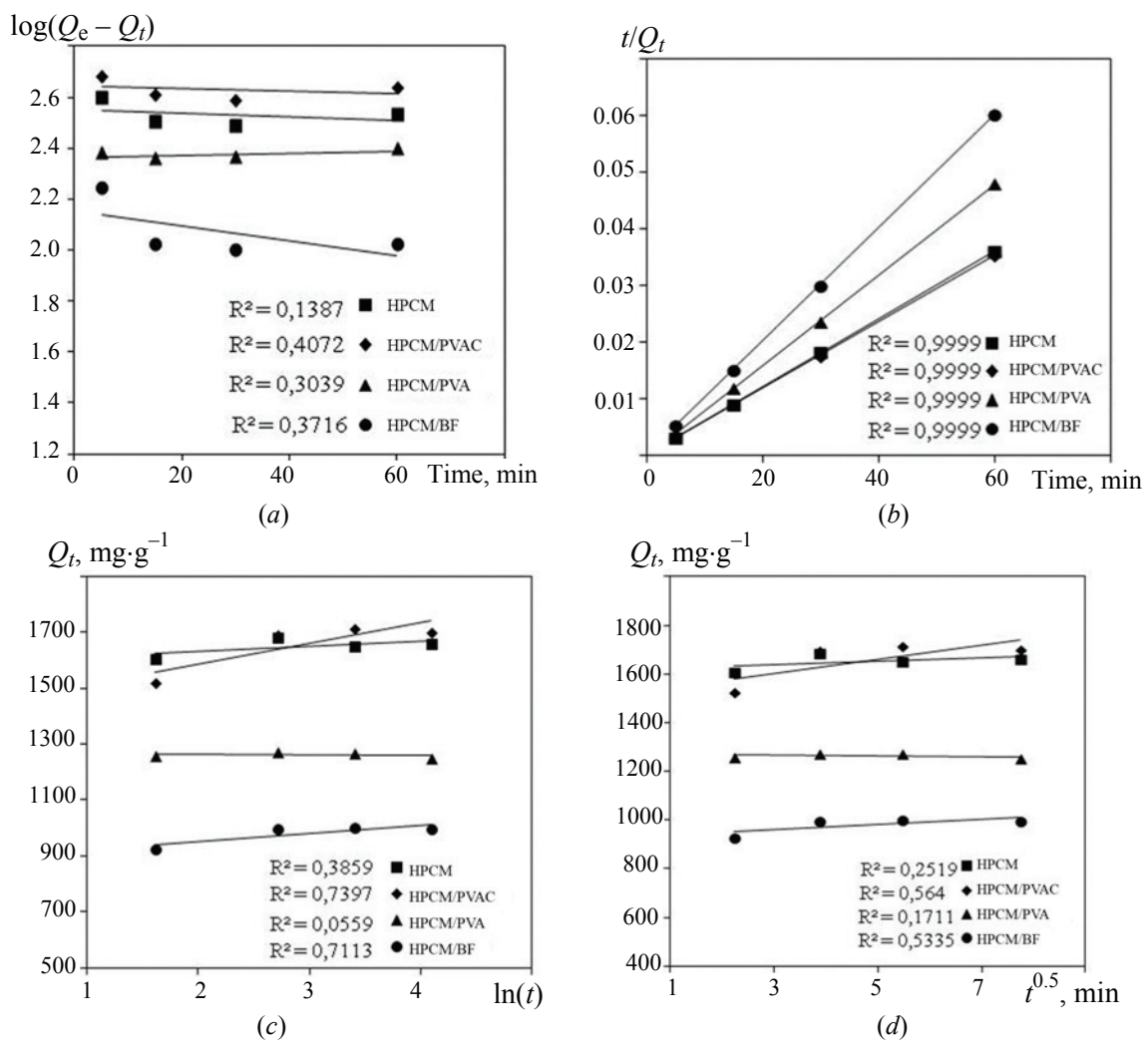


Fig. 3. Results of mathematical processing of experimental kinetic data:
 a – the pseudo-first order model; b – the pseudo-second order model;
 c – the Elovich equation model; d – the intraparticle diffusion equation model

position on the sorbent), i.e. a chemical interaction occurs between the dye molecules and the functional groups of the sorbent.

Analyzing the differences in the adsorption characteristics of the studied samples, it can be assumed at this stage of research that when PVA is used as a binder, a certain stable spatial structure is formed that ensures good transport permeability of the adsorbed substances, when PVAC is used, such a structure is formed somewhat worse, with the possible closure of part of the pores directly by the binder. In the case of application as a binder fiber, a significant drop in the sorption capacity can be explained by the formation of a rigid spatial framework in a compacted sample without the formation of transport pores, i.e. only the outer surface of the sample remains active.

4. Conclusion

The conducted studies have shown the relevance of the development of compacted carbon materials for their use as sorption materials. The main stages of obtaining these materials were determined, which included the selection of the initial carbon raw material, the activator and process parameters for high-temperature chemical activation, the establishment of process modes for compacting the prepared activated carbon material (pressure, duration and temperature) – for which a laboratory setup was developed and various binders were selected (for which polyvinyl alcohol, polyvinyl acetate and basalt fiber were used).

The characteristics of the compacted carbon material were found: the specific surface area and pore volume amounted to 1550–2000 m²·g⁻¹ and 0.693–0.849 cm³·g⁻¹, respectively. The maximum adsorption capacity for methylene blue for the initial HPCM was 1691 mg·g⁻¹, while for materials with binding agents HPCM/PVA, HPCM/BF, and HPCM/PVAC it was 1611 mg·g⁻¹, 1000 mg·g⁻¹, and 1270 mg·g⁻¹, respectively. The time of adsorption equilibrium of the process when using carbon sorbents HPCM, HPCM/PVA, HPCM/PVAC, HPCM/BF was ≈ 15 minutes. Also, experimental kinetic data were described using the known equations of kinetic models (the pseudo-first and pseudo-second order equations, the Elovich equation and the intraparticle diffusion equation). As a result, it was found that the experimental dependences have high correlation coefficients R^2 with the calculated values obtained using the pseudo-second order model. This brings us to the conclusion that chemical sorption of the MB dye has a predominant effect on

compacted carbon sorbents. A direct dependence of the sorption capacity of compacted samples and their strength characteristics on the type and content of the binder used and compaction modes was established, which can be explained by the obtained structure of the material, however, these areas are separate stages of research that are not included in this study.

Thus, it can be concluded that the compacted carbon material prepared with various binders can be an effective adsorbent of pollutants from aqueous solutions, which makes it a promising material for solving environmental problems.

5. Funding

The study was supported by the Russian Science Foundation grant No. 22-13-20074, <https://rscf.ru/project/22-13-20074/>.

6. Acknowledgments

This work was done using facilities of the shared access center “Production and application of multifunctional nanomaterials” (Tambov State Technical University).

7. Conflict of interests

The authors declare no conflict of interest.

References

1. Krasnikova EM, Moiseenko NV. Adsorption and structural characteristics of carbon-containing adsorbents from plant raw material modified with oxidizers. “*Actual physical and chemical problems of adsorption and synthesis of nanoporous materials*”: All-Russian symposium with international participation, dedicated to the memory of Corresponding Member of the Russian Academy of Sciences V.A. Avramenko. Moscow: IPChE RAS; 2022. p. 219-221. (In Russ.)
2. Mishchenko SV, Tkachev AG. *Carbon nanomaterials: production property application*. Moscow: Mashinostroyeniye Publ.; 2008.320 p. (In Russ.)
3. Popova AA, Shubin IN. et al. Features of development of perspective sorbents of a new generation based on carbon nanomaterial. *6 interdisciplinary scientific forum with international participation “New materials and perspective technologies” collection of materials*. Moscow: Center for Scientific and Technical Solutions; 2020. p. 733-735. (In Russ.)
4. Klimov ES, Buzaeva MV. *Natural sorbents and complexones in wastewater treatment*. Ulyanovsk: UIGTU; 2011. 201 p. (In Russ.)
5. Popova AA, Aliev RE, Shubin IN. Features of nanoporous carbon material synthesis. *Advanced Materials & Technologies*. 2020;3(19):28-32. DOI:10.17277/amt.2020.03.pp.028-032

6. Jorda-Beneyto M, Suarez-Garcia F, Lozano-Castell D, Cazorla-Amoros D, Linares-Solano A. Hydrogen storage on chemically activated carbons and carbon nanomaterials at high pressure. *Carbon*. 2007;45(2):293-303. DOI:10.1016/j.carbon.2006.09.022
7. Popova AA, Shubin IN. Investigation of technological activation parameters affecting the characteristics of nanoporous carbon material. *Materials Science*. 2022;11:3-8. DOI:10.31044/1684-579X-2022-0-11-3-8
8. Carvalho AP, Cardoso B, Pires J, Carvalho MB. Preparation of activated carbons from cork waste by chemical activation with KOH. *Carbon*. 2003;41(14):2873-2876. DOI:10.1016/S0008-6223(03)00323-3
9. Popova AA, Shubin IN. Study of the process of high-temperature alkaline activation of carbon material with additional exposure to water vapor. *Vestnik Tambovskogo gosudarstvennogo tekhnicheskogo universiteta*. 2022;28(3):76-486. DOI:10.17277/vestnik.2022.03. pp.476-486 (In Russ.)
10. Lozano-Castello D, Calo JM, Cazorla-Amoros D, Linares-Solano A. Carbon activation with KOH as explored by temperature programmed techniques, and the effects of hydrogen. *Carbon*. 2007;45:2529-2536. DOI:10.1016/j.carbon.2007.08.021
11. Dong W, Xia W, Xie K. et al. Synergistic effect of potassium hydroxide and steam co-treatment on the functionalization of carbon nanotubes applied as basic support in the pd-catalyzed liquid-phase oxidation of ethanol. *Carbon*. 2017;121:452-462. DOI:10.1016/J.CARBON.2017.06.019
12. Falco C, Marco-Lozar JP, Salinas-Torres D, Morallo'n E, Cazorla-Amoro's D, Titirici MM, Lozano-Castello D. Tailoring the porosity of chemically activated hydrothermal carbons: Influence of the precursor and hydrothermal carbonization temperature. *Carbon*. 2013;62:346-355. DOI:10.1016/j.carbon.2013.06.017
13. Marco-Lozar JP, Kunowsky M, Carruthers JD, Linares-Solano A. Gas storage scale-up at room temperature on high density carbon materials. *Carbon*. 2014;76:123-132. DOI:10.1016/j.carbon.2014.04.058
14. Seema H, Kemp KC, Le NH, Park S-W, Chandra V, Lee JW, Kim KS. Highly selective CO₂ capture by S-doped microporous carbon materials. *Carbon*. 2014;66:320-326. DOI:10.1016/j.carbon.2013.09.006
15. Sevilla M, Fuertesa AB, Mokayac R. Preparation and hydrogen storage capacity of highly porous activated carbon materials derived from polythiophene. *International Journal of Hydrogen Energy*. 2011;36(24):15658-15663. DOI:10.1016/j.ijhydene.2011.09.032
16. Kim HS, Kang MS, Yoo WC. Highly enhanced gas sorption capacities of N-doped porous carbon spheres by hot NH₃ and CO₂ treatments. *The Journal of Physical Chemistry C*. 2015;119(51):28512-28522. DOI:10.1021/acs.jpcc.5b10552
17. Gadipelli S, Guo ZX. Graphene-based materials: synthesis and gas sorption, storage and separation. *Progress in Materials Science*. 2015;69:1-60. DOI:10.1016/j.pmatsci.2014.10.004
18. Cychosz KA, Thommes M. Progress in the physisorption characterization of nanoporous gas storage materials. *Engineering*. 2018;4:559-566. DOI:10.1016/j.eng.2018.06.001
19. Bahadur J, Melnichenko YB, He L, Contescu CI, Gallego NC, Carmichael JR. SANS investigations of CO₂ adsorption in microporous. *Carbon*. 2015;95:535-544. DOI:10.1016/j.carbon.2015.08.010
20. Perez-Mendoza M, Schumacher C, Suarez-Garcia F, Almazan-Almazan MC, Domingo-Garci'a M, Lo'pez-Garzo'n FJ, Seaton NA. Analysis of the microporous texture of a glassy carbon by adsorption measurements and Monte Carlo simulation. Evolution with chemical and physical activation. *Carbon*. 2006;44:638-645. DOI:10.1016/j.carbon.2005.09.037
21. Wu X, Shaibani M, Smith SJD, Konstas K, Hill MR, Wang H, Zhang K, Xie Z. Microporous carbon from fullerene impregnated porous aromatic frameworks for improving the desalination performance of thin film composite forward osmosis membranes. *Journal of Materials Chemistry A*. 2018;6(24):11327-11336. DOI:10.1039/C8TA01200H
22. Zgrzebnicki M, Kalamaga A, Wrobel R. Sorption and textural properties of activated carbon derived from charred beech wood. *Molecules*. 2021;26:7604. DOI:10.3390/molecules26247604
23. Olontsev VF, Farberova EA, Minkova AA. et al. Optimization of the porous structure of activated carbons in the process of technological production. *Vestnik PNIPU. Himicheskaya tekhnologiya i biotekhnologiya*. 2015;4:9-23. (In Russ.)
24. Tkachev AG, Memetov NR, Kucherova AE, Merzik AV, Shubin IN, Zelenin AD, Popova AA. *Molded nanostructured microporous carbon sorbent and method of its preparation*. Russian Federation patent 2736586. 18 November 2020. (In Russ.)
25. Fenelonov VB. *Porous carbon*. Novosibirsk: Institute of Catalysis SB RAS; 1995. 518 p. (In Russ.)
26. Vasiliev LL, Kanonchik LE, Kulakov AG, Mishkinis DA, Safonova AM, Luneva NK. Activated carbon fiber composites for ammonia, methane and hydrogen adsorption. *International Journal of Low-Carbon Technologies*. 2006;1(2):95-111. DOI:10.1093/ijlct/1.2.95
27. Ouyang J, Zhou L, Liu Z, Heng JYY, Chen W. Biomass-derived activated carbons for the removal of pharmaceutical micropollutants from wastewater: a review. *Separation and Purification Technology*. 2020;253:117536. DOI:10.1016/j.seppur.2020.117536
28. Han X, Wang H, Zhang L. Efficient removal of methyl blue using nanoporous carbon from the waste biomass. *Water Air Soil Pollution*. 2018;229(2):26. DOI:10.1007/s11270-017-3682-0
29. Shahkarami S, Azargohar R, Dalai AK, Soltan J. Breakthrough CO₂ adsorption in bio-based activated carbons. *Journal of Environmental Sciences*. 2015;34:68-76. DOI:10.1016/j.jes.2015.03.008
30. Pérez-Mayoral E, Matos I, Bernardo M, Fonseca IM. New and advanced porous carbon materials in fine chemical synthesis. *Emerging Precursors of Porous Carbons. Catalysts*. 2019;9(2):133. DOI:10.3390/catal9020133
31. Goncharov AI. *Handbook of chemistry*. Kyiv: Vishcha school; 1978. 308 p. (In Russ.)

32. Mkrtchyan ES, Ananyeva OA, Burakova IV, Burakov AE. Synthesis of nanocomposite materials on basis of modified graphene oxide for removal of organic dyes from aqueous media. *XXXVI international scientific and practical conference: "Issues of science 2022: potential of science and modern aspects"*. Anapa: Research Center ESP; 2022. p. 60-64. (In Russ.)
33. Shooto ND, Nkutha CS, Guiland NG, Naidoo EB. Pristine and modified mucuna beans adsorptive studies of toxic lead ions and methylene blue dye from aqueous solution. *South African journal of Chemical Engineering*. 2020;31:33-43. DOI:10.1016/j.sajce.2019.12.001
34. Hossain S, ShahrzamanMd, Kabir SF, Rahman MdS, Sultana S, Mallik AK, Haque P, Takafuji M, Rahman MM. Jute cellulose nanocrystal/poly(N,N-dimethylacrylamide-co-3-methacryloxypropyltrimethoxysilane) hybrid hydrogels for removing methylene blue dye from aqueous solution. *Journal of Science: Advanced Materials and Devices*. 2021;6(2):254-263. DOI:10.1016/j.jsamd.2021.02.005
35. Mbaz GM, Parani S, Oluwafemi OS. Instant removal of methylene blue using water-soluble non-cadmium based quantum dots. *Materials Letters*. 2021;303:130495. DOI:10.1016/j.matlet.2021.130495
36. Ray J, Jana S, Mondal B, Tripathy T. Enhanced and rapid adsorptive removal of toxic organic dyes from aqueous solution using a nanocomposite of saponified polymethyl acrylate grafted dextrin with embedded nanosilica. *Journal of Molecular Liquids*. 2019;275: 879-894. DOI:10.1016/j.molliq.2018.11.126
37. Ofgea NM, Tura AM, Fanta GM. Activated carbon from H_3PO_4 -activated moringastenopetale seed husk for removal of methylene blue: optimization using the response surface method (RSM). *Environmental and Sustainability Indicators*. 2022;16:100214. DOI:10.1016/j.indic.2022.100214
38. Wang Y, Pan J, Li Y, Zhang P, Li M, Zheng H, Zhang X, Li H, Du Q. Methylene blue adsorption by activated carbon, nickel alginate/activated carbon aerogel, and nickel alginate/graphene oxide aerogel: a comparison study. *Journal of Materials Research and Technology*. 2020;9(6):12443-12460. DOI:10.1016/j.jmrt.2020.08.084
39. Nayeri D, Mousavi SA, Fatahi M, Almasi A, Khodadoost F. Dataset on adsorption of methylene blue from aqueous solution onto activated carbon obtained from low cost wastes by chemical-thermal activation – modelling using response surface methodology. *Data in Brief*. 2019;25:104036. DOI:10.1016/j.dib.2019.104036
40. Al-Ghouti MA, Sweleh AO. Optimizing textile dye removal by activated carbon prepared from olive stones. *Environmental Technology and Innovation*. 2019;16:100488. DOI:10.1016/j.eti.2019.100488
41. Ji B, Wang J, Song H, Chen W. Removal of methylene blue from aqueous solutions using biochar derived from a fallen leaf by slow pyrolysis: Behavior and mechanism. *Journal of Environmental Chemical Engineering*. 2019;7(3):103036. DOI:10.1016/j.jece.2019.103036
42. Li Z, Hanafy H, Zhanga L, Sellaoud L, Nettoe MS, Oliveiraf MLS, Seliemh MK, Dottoe GL, Bonilla-Petriciolet A, Li Q. Adsorption of congo red and methylene blue dyes on an ashitaba waste and a walnut shell-based activated carbon from aqueous solutions: Experiments, characterization and physical interpretations. *Chemical Engineering Journal*. 2020;388:124263. DOI:10.1016/j.ccej.2020.124263
43. Somsesta N, Sricharoenchaikul V, Aht-Ong D. Adsorption removal of methylene blue onto activated carbon/cellulose biocomposite films: Equilibrium and kinetic studies. *Materials Chemistry and Physics*. 2015;240: 122221. DOI:10.1016/j.matchemphys.2019.122221
44. Canales-Flores RA, Prieto-García F. Taguchi optimization for production of activated carbon from phosphoric acid impregnated agricultural waste by microwave heating for the removal of methylene blue. *Diamond and Related Materials*. 2020;109:108027. DOI:10.1016/j.diamond.2020.108027
45. Gautam RK, Chattopadhyaya MC. *Nanomaterials for wastewater remediation*. Oxford: Elsevier; 2016. 347 p.

Information about the authors / Информация об авторах

Elina S. Mkrtchyan, Postgraduate, Tambov State Technical University (TSTU), Tambov, Russian Federation; ORCID 0000-0002-3867-7063; e-mail: elina.mkrtchyan@yandex.ru

Oksana A. Ananyeva, Master's Degree Student, TSTU, Tambov, Russian Federation; ORCID 0000-0002-1188-9402; e-mail: oksana.a9993471@gmail.com

Igor N. Shubin, Cand. Sc. (Eng.), Associate Professor, Associate Professor, TSTU, Tambov, Russian Federation; ORCID 0009-0007-3235-5702; e-mail: i.shubin77@yandex.ru

Мкртчян Элина Саковна, аспирант, Тамбовский государственный технический университет (ТГТУ), Тамбов, Российская Федерация; ORCID 0000-0002-3867-7063; e-mail: elina.mkrtchyan@yandex.ru

Ананьева Оксана Альбертовна, магистрант, ТГТУ, Тамбов, Российская Федерация; ORCID 0000-0002-1188-9402; e-mail: oksana.a9993471@gmail.com

Шубин Игорь Николаевич, кандидат технических наук, доцент, ТГТУ, Тамбов, Российская Федерация; ORCID 0009-0007-3235-5702; e-mail: i.shubin77@yandex.ru

Received 25 August 2023; Accepted 9 October 2023; Published 15 December 2023



Copyright: © Shubin IN, Mkrtchyan ES, Ananyeva OA, 2023. This article is an open access article distributed under the terms and conditions of the Creative Commons Attribution (CC BY) license (<https://creativecommons.org/licenses/by/4.0/>).

A method of obtaining aluminum tris(8-hydroxyquinoline) and its physicochemical properties

© Denis V. Belov^{ab}✉, Sergey N. Belyaev^{ab}, Pavel A. Yunin^b, Dmitriy B. Radishev^a

^a Federal Research Center A.V. Gaponov-Grekhov Institute of Applied Physics of the Russian Academy of Sciences, 46, Ulyanova St., Nizhny Novgorod, 603950, Russian Federation,

^b The Institute for Physics of Microstructures of the Russian Academy of Sciences, Nizhny Novgorod, 603950, Russian Federation

✉ bdv@ipfran.ru

Abstract: Obtaining high-purity single-crystalline aluminum tris(8-hydroxyquinolate) (Alq_3) in significant volumes is a topical task both for OLED technologies and for its use as a promising electron-pumped laser material. This article proposes a simple, convenient and ecologically friendly “one-pot” synthesis based on the interaction of high-purity aluminum powder and 8-hydroxyquinoline in an aqueous solvent of ammonia with high yield. The method allows for the selective synthesis of an α -polymorphic modification of the meridional isomer Alq_3 . An electron microscopic study of the α -phase powder *mer*- Alq_3 was carried out. It has been determined that the substance has a uniform morphology of a tree-like branching structure formed from rod-like linear crystals. The structure of the resulting compound was characterized by X-ray diffraction, Raman spectroscopy, and electron spectroscopy. Qualitative and semi-quantitative analysis of chemical elements was carried out using energy-dispersive X-ray spectroscopy (EDX method). The optical absorption spectra of Alq_3 solvents in eight organic solvents were studied: DMSO, CH_3CN , EtOH, *i*-PrOH, TEP, CHCl_3 , 1,4-dioxane, and toluene. The molar extinction coefficients of α - Alq_3 in organic solvents were calculated in the short-wave and visible regions of the spectrum. The solvatochromic effect in the studied systems was assessed. A methodology for the quantitative determination of Alq_3 in organic solvents and standardization of its solvents has been developed by the spectrophotometric method.

Keywords: one-pot synthesis; aluminum tris(8-hydroxyquinoline); *mer*- Alq_3 ; 8-hydroxyquinoline; Raman spectroscopy; UV/VIS; OLED; OLED.

For citation: Belov DV, Belyaev SN, Yunin PA, Radishev DB. Obtaining method and physicochemical properties of aluminum tris(8-hydroxyquinoline). *Journal of Advanced Materials and Technologies*. 2023;8(4):279-293. DOI: 10.17277/jamt.2023.04.pp.279-293

Способ получения и физико-химические свойства трис(8-гидроксихинолината) алюминия

© Д. В. Белов^{ab}✉, С. Н. Беляев^{ab}, П. А. Юнин^b, Д. Б. Радищев^a

^a Институт прикладной физики им. А. В. Гапонова-Грехова РАН, ул. Ульянова, 46, Нижний Новгород, 603950, Российская Федерация,

^b Институт физики микроструктур РАН, ГСП-105, Нижний Новгород, 603950, Российская Федерация

✉ bdv@ipfran.ru

Аннотация: Получение высокочистого монокристаллического трис(8-гидроксихинолината) алюминия (Alq_3) в значительных объемах является актуальной задачей как для ОСИД-технологий, так и для его применения в качестве перспективного лазерного материала с электронной накачкой. В статье предложен простой, удобный и экологичный «one-pot» синтез, основанный на взаимодействии порошка высокочистого алюминия и 8-гидроксихинолина в водном растворе аммиака с высоким выходом. Метод позволяет осуществлять селективный синтез α -полиморфной модификации меридионального изомера Alq_3 . Проведено электронно-микроскопическое

исследование порошка α -фазы *mer*-Alq₃. Определено, что вещество имеет однородную морфологию древовидной ветвящейся структуры, образованной из стержневидных линейных кристаллов. Структура полученного соединения охарактеризована методами рентгеновской дифракции, спектроскопии комбинационного рассеивания света и электронной спектроскопии. Методом энергодисперсионной рентгеновской спектроскопии (EDX-метод) проведен качественный и полуколичественный анализ химических элементов. Изучены спектры оптического поглощения растворов Alq₃ в восьми органических растворителях: ДМСО, CH₃CN, EtOH, *i*-PrOH, ТЭФ, CHCl₃, 1,4-диоксан, толуол. Рассчитаны коэффициенты молярной экстинкции α -Alq₃ в органических растворителях в коротковолновой и видимой областях спектра. Проведена оценка сольватохромного эффекта в изученных системах. Разработана методика количественного определения Alq₃ в органических растворителях и стандартизации его растворов спектрофотометрическим методом.

Ключевые слова: «one-pot» синтез; трис(8-гидроксихинолилат) алюминия; *mer*-Alq₃; 8-гидроксихинолин; КР-спектроскопия; UV/VIS; ОСИД; OLED.

Для цитирования: Belov DV, Belyaev SN, Yunin PA, Radishev DB. Obtaining method and physicochemical properties of aluminum tris(8-hydroxyquinoline). *Journal of Advanced Materials and Technologies*. 2023;8(4):279-293. DOI: 10.17277/jamt.2023.04.pp.279-293

1. Introduction

The studies of Tang and Van Slyke in 1987 [1], who discovered the intense electroluminescence of aluminum tris(8-hydroxyquinolate), began the era of developing new light-emitting devices – Organic Light Emitting Diodes (OLEDs). Recently, technical products based on the use of organic electroluminophores have become of great practical importance. Based on them, new highly efficient light sources and information display devices are being developed.

Compared to fluorescent lamps and inorganic light-emitting diodes (LED), OLED devices have a number of advantages: smaller dimensions, weight and power consumption with comparable brightness, better color rendering, low power dissipation of the luminous surface and the ability to create large luminous surfaces (flat displays).

Aluminum tris(8-hydroxyquinolate) (Alq₃) is one of the most widely used compounds in OLED technology. Due to its thermal stability, ease of synthesis and purification, and exceptional electron transport and electroluminescent properties in thin films, Alq₃ is used as a green organic electroluminescent phosphor and an electron transport layer in the manufacture of OLED devices.

Alq₃ is an organometallic coordination compound that emits green light with a photoluminescence wavelength of about 500 nm. In metal hydroxyquinolates, hydroxyquinolines act as bidentate ligands and attach to the aluminum atom through oxygen and nitrogen atoms with a coordination number of six. The luminescence ability of Alq₃ is responsible for the $\pi \rightarrow \pi^*$ electronic transition from the HOMO of the ligand, localized on the phenoxyl ring, to the LUMO, located on the pyridine ring.

Today, the existence of two isomers is known: meridional *mer*-Alq₃ and frontal *fac*-Alq₃ which crystallize in five polymorphic modifications of Alq₃ – α , β , γ , δ , ϵ [2–5]. Each such phase is stable under certain thermodynamic conditions and has its own spectral characteristics [6].

It is currently known that three of the five polymorphic modifications of crystalline Alq₃ (α , β , ϵ) are composed of *mer*- isomers (*meridional*) with C1 symmetry [3], and two polymorphic modifications (γ , δ) are composed of *fac*- isomers (*facial*) with C3 symmetry [6]. The phase and impurity purity of Alq₃ determines both the basic functional properties of the compound (luminescence, electron-hole conductivity, etc.) and the durability of the product as a whole.

Various methods for the synthesis of Alq₃ are presented in the literature [7–9], but there is no easy-to-implement method of directed synthesis with controlled phase composition. The task of obtaining high-purity Alq₃ in significant volumes is relevant not only for OLED technologies, but also for further studies of single-crystal Alq₃, which is used as a promising electron-pumped laser material.

The purpose of this work is to obtain Alq₃ in a new, convenient way and to study its structural and optical properties using Raman spectroscopy and UV-visible spectrophotometry.

2. Materials and Methods

2.1. Alq₃ synthesis

Sample I. To synthesize the product, the well-known technique proposed in [10] was used. The product was obtained from 8-hydroxyquinoline (HQ) and aluminum salt in an aqueous medium. For this purpose, 1 g of aluminum nitrate Al(NO₃)₃·9H₂O

was dissolved in 100 mL of deionized H₂O. The solvent was heated to 60 °C. 1.5 g of HQ was dissolved in a mixture consisting of 20 mL of H₂O and 4 mL of glacial acetic acid. The HQ solvent was slowly added drop wise to the aluminum nitrate solvent. The pH of the resulting solvent was then increased to 8 by adding ammonia solvent to precipitate the product Alq₃. The resulting precipitate was thoroughly washed with hot water (60 °C). The bright yellow powder with a melting point > 300 °C was dried in a vacuum oven at a temperature of 130 °C. The yield of Alq₃ was no more than 95 %.

Sample II. 1 g of Al₂O₃ was added to 100 mL of 1 M HCl solvent and heated to 50–60 °C. The solvent was filtered while hot. A 10 % excess of the reagent was added to the resulting filtrate, then a freshly prepared 2 M solvent of CH₃COONH₄ was slowly introduced until a non-disappearing yellow precipitate appeared and an additional 25 mL was added for complete precipitation. The precipitate was filtered, washed with hot water and dried at 120 °C. The reagent was prepared as follows: 12.5 g of HQ was added with stirring to 25 mL of glacial acetic acid with low heating until dissolved. The resulting solvent was poured into 450 mL of deionized H₂O heated to 60 °C. The solvent was cooled, filtered and diluted to 500 mL.

Sample III. Alq₃ synthesis was carried out according to the method [5] in isopropyl alcohol (*i*-PrOH).

Sample IV. Metallic aluminum powder (“PA-HF”, 99.99 wt. %) and a 25 % aqueous solvent of ammonia hydrate NH₃·H₂O (“special purity grade”, 99.9 wt. %) were used as starting materials. Alq₃ synthesis was carried out in one step. Aluminum powder was poured (25 °C) into a NH₃·H₂O solvent, the mixture was heated until its activation it and stirred until intense gas evolution began. A solvent of HQ in a 10 % aqueous solvent of ammonia hydrate was added to the resulting mixture in a molar ratio of Al : HQ = 1 : 3. The initial reagent HQ (pure grade, 99.9 wt. %) was recrystallized from absolute EtOH and dried in vacuum ($T_{\text{melt}} = 74.5\text{--}75\text{ }^{\circ}\text{C}$). The reaction vessel was then placed on a heating device and kept at boiling temperature for 60 minutes. The synthesis was carried out with constant stirring at a speed of at least 300 rpm. Over time, the solvent became discolored and a yellow-green precipitate formed. The resulting precipitate was filtered, washed with water and dried at a temperature of 120 °C in an argon atmosphere.

The synthesis product was a yellow-green crystalline powder ($T_{\text{melt}} = 300\text{ }^{\circ}\text{C}$). Recrystallization was carried out from chloroform.

A comparison was made with commercially available Alq₃ (Sigma-Aldrich) with a purity of at least 99.995 %.

During the studies the following organic solvents were used: EtOH (≥ 99.8 %, special purity), *i*-PrOH (≥ 99.8 %, special purity, 11-5 OP-1, JSC “EKOS-1”, Russia), CH₃CN (≥ 99.8 %, analytical grade, JSC “EKOS-1”, Russia), dimethyl sulfoxide (DMSO) (≥ 99.8 %, UFS, JSC “EKOS-1”, Russia), CHCl₃ (≥ 99.8 %, reference, JSC “EKOS-1”, Russia), 1,4-dioxane (≥ 99.8 %, analytical grade, JSC “EKOS-1”, Russia), toluene (≥ 99.8 %, analytical grade, JSC “EKOS-1”, Russia), triethyl phosphate (TEP) (≥ 99.8 %, JSC “EKOS-1”, Russia). All solvents were purified, dehydrated, and distilled using standard methods before use.

2.2. Analytic methods

X-ray diffraction analysis of powdered samples was carried out on a Bruker D8 Discover diffractometer (CuK α radiation) in Bragg-Brentano geometry with a LynxEye linear position-sensitive detector. The analyzed powders were placed in identical fused quartz cuvettes, and diffraction patterns were recorded by $\theta/2\theta$ scanning in the angular range from 3° to 50° along the 2 θ angle.

The morphology of the synthesized samples was studied using a VEGA 3 XMH (TESCAN) scanning electron microscope (SEM) with a LaB₆ lanthanum hexaboride cathode. The samples were applied to adhesive conductive tape without prior manipulation or mechanical impact. Qualitative and semi-quantitative analysis of chemical elements was carried out by energy dispersive X-ray spectroscopy (EDX method) using an energy dispersive spectrometer based on a semiconductor silicon drift detector with nitrogen-free cooling manufactured by OXFORD INSTRUMENTS, with an accuracy of the mass fraction of elements of 0.1 %, mounted on a scanning electron microscope column with range of detectable elements from Be(4) to Pu(94).

Micrographs of the synthesized Alq₃ samples were obtained using a ZEISS Axio Imager Vario optical microscope. The following research methods in reflected light were used: bright field, dark field, polarization contrast, differential interference contrast (Nomarski DIC), circular differential interference contrast (C-DIC).

Raman spectroscopy (Raman spectra) was performed on a Renishaw InVia Reflex instrument (Renishaw plc, UK) with a Leica DMLM confocal microscope with a resolution of up to 2.5 μm . The laser radiation wavelength was 514.5 nm, the radiation power was 0.1–1.0 mW at the measurement point, and the diameter of the analyzing laser beam was $\sim 1 \mu\text{m}$.

Electronic absorption spectra (UV/VIS spectra) of Alq_3 were recorded using a UV-3600i Plus spectrophotometer (Shimadzu, Japan) (with a quartz cuvette absorbing layer thickness of 10 mm in dual-beam mode).

3. Results and Discussion

3.1. Crystal structure of synthesized compounds

Figures 1 and 2 demonstrate X-ray diffraction patterns of the synthesized Alq_3 samples. Figure 1 shows diffraction patterns of the synthesized products: samples I–III. All samples differ from each other in the location of the characteristic peaks. However, none of them corresponds to the spectrum characterizing the pure Alq_3 phase. Unidentified and additional peaks can be seen in the spectra. For example, the diffraction pattern shown in Fig. 1 (curve 2) contains a number of additional peaks in the 2θ range at $8.5\text{--}11^\circ$, $17\text{--}18^\circ$, $21\text{--}23^\circ$, 24° , $31\text{--}35^\circ$. The presence of additional peaks, their modification and disappearance indicates the presence of impurities and residual solvents [11].

Figure 2 (curve 2) shows the diffraction pattern of Alq_3 (sample IV) obtained by the proposed method.

For comparison, Fig. 2 also demonstrates a powder diffraction pattern (curve 1) calculated in the “Diffrac. Topas” software package based on CCDC data # 1241652 for single crystals of the α -phase Alq_3 [12]. When calculating the diffraction pattern from the cif file data in “Diffrac. Topas” and fitting it to the experiment, the fundamental parameters approach was used. At the same time, instrumental parameters were set, i.e. dimensions of the slits (0.6 mm equatorial slit on the primary beam and the axial Soller slit 2.5°), detector parameters (a position-sensitive one-dimensional Lynx EYE detector with an aperture of 2° at the angle 2θ was used), taking into account the axial and equatorial divergence of the beam and spectral composition of radiation ($\text{CuK}\alpha$ doublet). When fitting, the parameters of the powder microstructure were varied – the sizes of the regions of coherent scattering and microdeformation (50 nm and 0.2 %, respectively), as well as the approximation of the instrumental background by a 5th order Chebyshev polynomial.

Figure 2 (curve 3) also shows a diffraction pattern of a commercial sample of the α -polymorphic phase *mer*- Alq_3 (Sigma-Aldrich). One can see an almost complete coincidence of the diffraction pattern of the synthesized α - Alq_3 (sample IV) with the calculation results and the diffraction pattern of the commercial sample.

The crystal structure of the α -phase Alq_3 has triclinic symmetry, space group $P\bar{1}$, unit cell parameters: $a = 6.2586(8) \text{ \AA}$, $b = 12.914(2) \text{ \AA}$, $c = 14.743(2) \text{ \AA}$, $\alpha = 109.66(1)^\circ$, $\beta = 89.66(1)^\circ$, $\gamma = 97.68(1)^\circ$ [12].

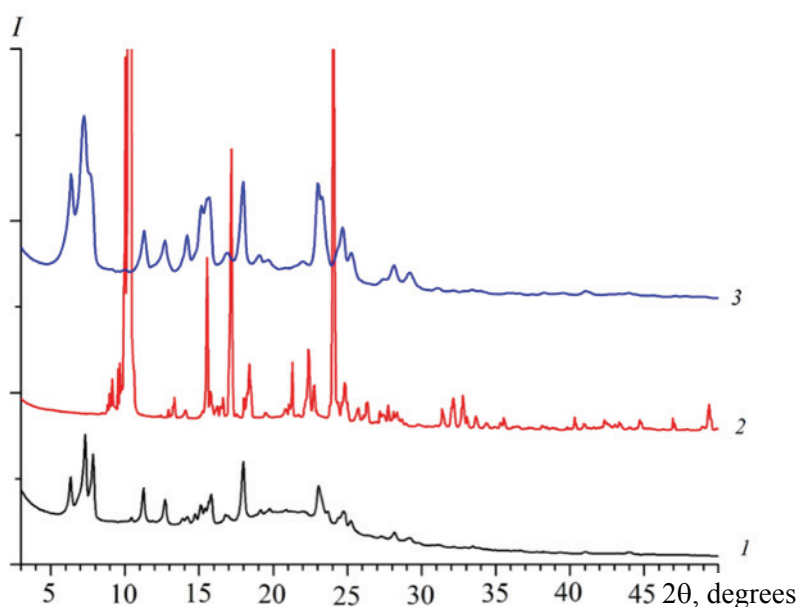


Fig. 1. X-ray diffraction patterns of Alq_3 powder samples: sample I (1), sample II (2), sample III (3)

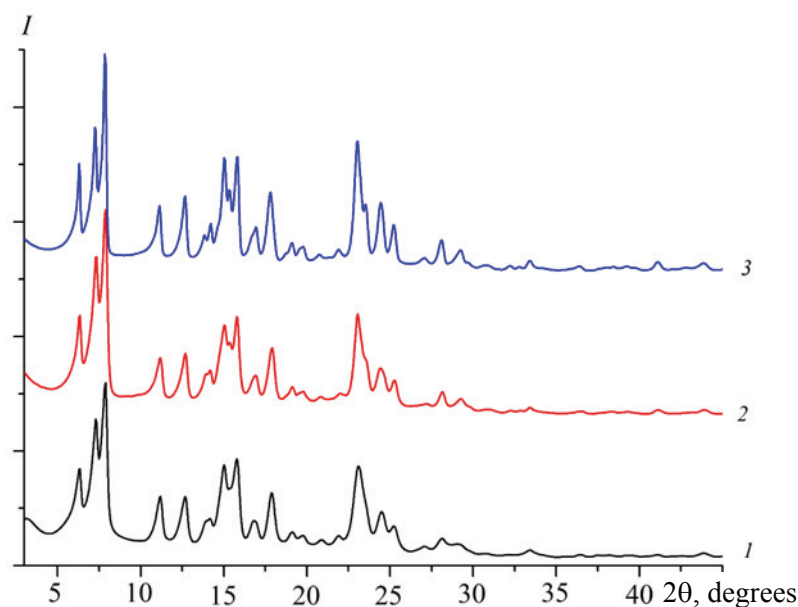


Fig. 2. Powder diffraction patterns of Alq_3 : according to the results of calculation in the “Diffrac. Topas” software package based on the data of [12] (1), synthesized sample IV (2), commercial sample of α -phase Alq_3 “Sigma-Aldrich” (3)

According to the powder diffraction data (Fig. 2, curve 2), the synthesized Alq_3 (sample IV) corresponds to the commercial preparation and calculated data, as indicated by the presence of three intense, well-resolved peaks in the range $6^\circ < 2\theta < 8^\circ$. It is also possible to identify two well-resolved peaks in the range $10^\circ < 2\theta < 13^\circ$, two peaks in the range $13^\circ < 2\theta < 17^\circ$, a characteristic peak at 18° and three well-resolved peaks in the range $23^\circ < 2\theta < 26^\circ$. The data obtained are consistent with previously published works [12–15].

Figure 3 shows the structure and crystal packing of the α -phase of the geometric *mer*- Alq_3 isomer.

Figure 4 shows photographs of *mer*- Alq_3 powder (sample IV). The product crystals have a rod shape with a random distribution. The maximum size of rods is about 100 μm . There are no obvious defects

visually observed on the surface of the crystals, which indicates a sufficiently high quality of the resulting *mer*- Alq_3 powder.

Electron microscopic research of the α -phase powder of *mer*- Alq_3 was carried out. Figure 5 shows the corresponding microphotographs. It was determined that the substance has a uniform morphology of a tree-like branching structure formed from rod-like linear crystals. The results of microscopy indicate the absence of impurities that differ in particle shape from the bulk of the substance, and the results of energy-dispersive elemental microanalysis confirm the formation of a powder of the *mer*- Alq_3 α -phase which is homogeneous in chemical composition. In Table 1 shows the data of EDX analysis of the synthesized Alq_3 powder (sample IV).

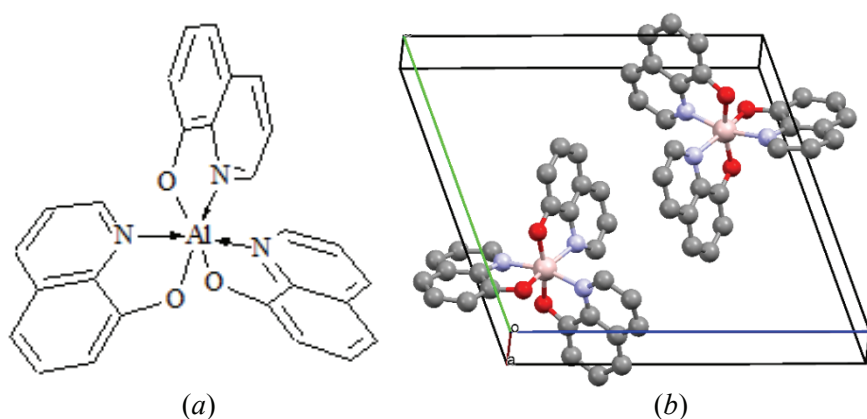


Fig. 3. Chemical structure (a) and type of crystal packing of the geometric *mer*- Alq_3 isomer (b)

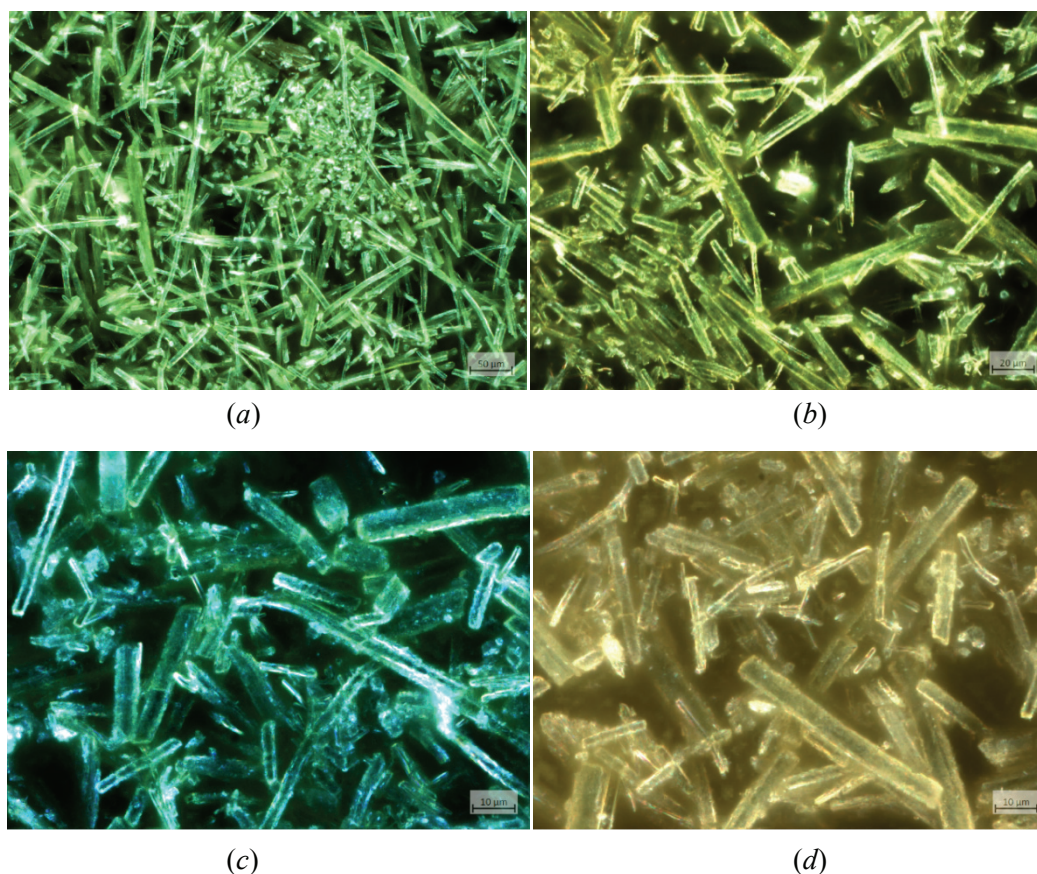


Fig. 4. Micrographs of *mer*-Alq₃ α-phase powder (sample IV):
×20, 0.5 HD DIC M27 (a); ×50, 0.8 HD DIC (b); ×100, 0.9 BD DIC (c); ×100, 0.9 BD DIC (d)

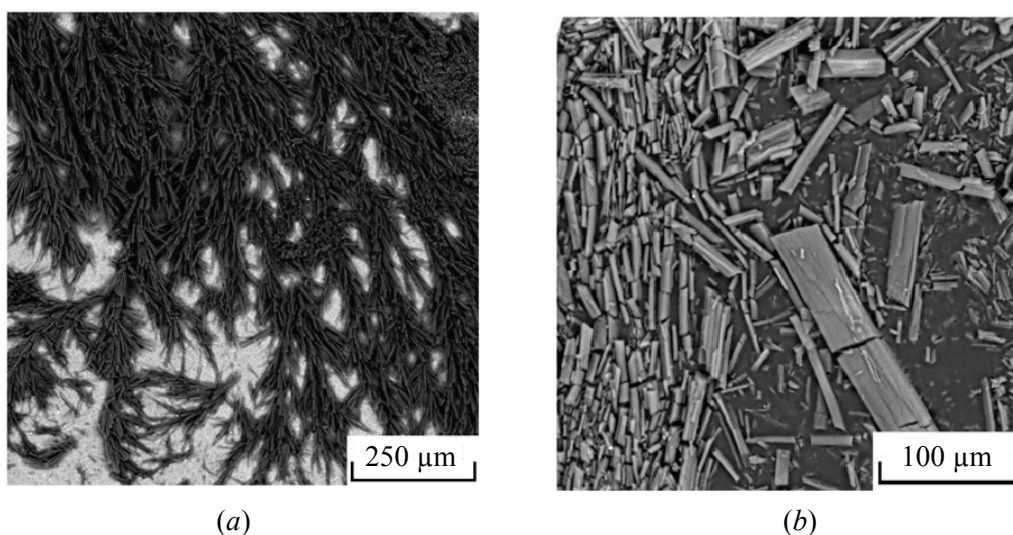


Fig. 5. Morphology of *mer*-Alq₃ α-phase powder crystals

Table 1. Results of Alq₃ EDX analysis (molecular formula C₂₇H₁₈AlN₃O₃, molecular weight 459.42)

Element	C	Al	N	O
Found (powder), wt. %	70.6 ± 0.01	5.7 ± 0.01	9.2 ± 0.01	10.5 ± 0.01
Calculated, wt. %	70.6	5.7	9.2	10.5

3.2. Raman spectroscopy of HQ and Alq₃

Figure 6 shows the Raman spectra of the synthesized sample of the *mer*-Alq₃ (sample IV) (1) α -phase and the original reagent of 8-hydroxyquinoline (HQ) (2).

Tables 2 and 3 show the interpretation of the Raman spectra of the synthesized compound, i.e. *mer*-

Alq₃ (sample IV) α -phase and 8-hydroxyquinoline (HQ).

Raman spectrum of Alq₃ (Table 2). According to literature data [16], about 150 normal modes can be distinguished in the Raman spectrum of Alq₃, which include vibrations of the hydroxyquinoline fragment and vibrations of the Al–O and Al–N bonds.

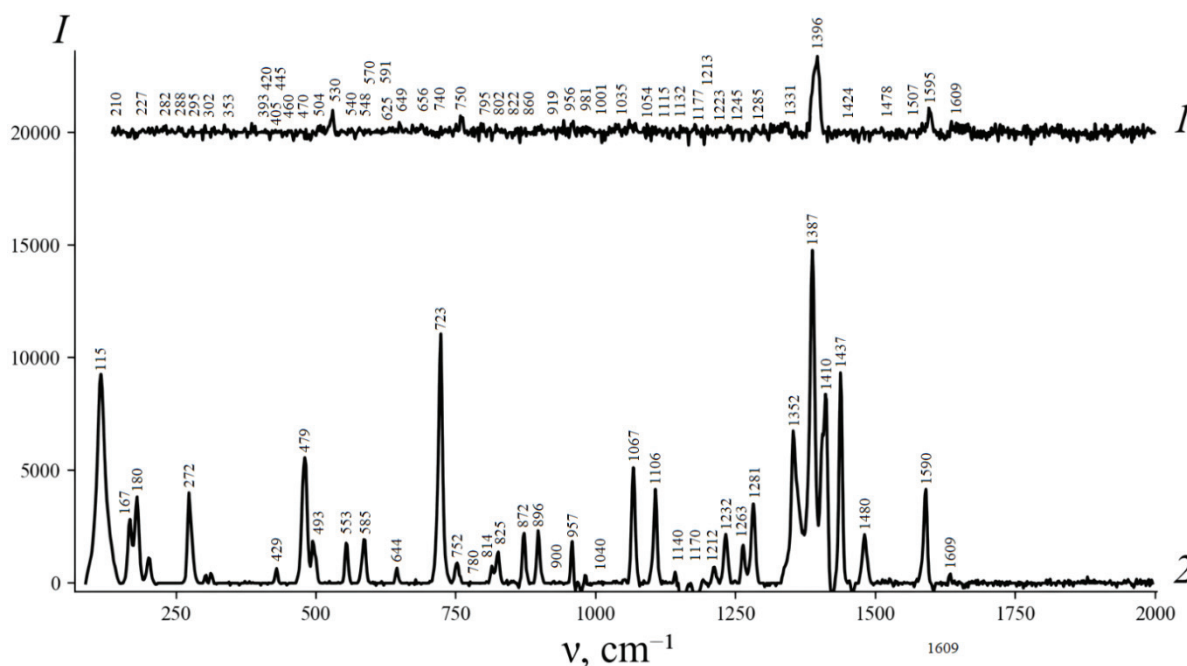


Fig. 6. Raman spectra: α -polymorphic phase of *mer*-Alq₃, sample IV (1), 8-hydroxyquinoline (HQ) (2)

Table 2. Line frequencies in the Raman spectrum (Fig. 6, spectrum 1) and Alq₃ vibrational mode assignment (sample IV)

ν , cm ⁻¹	Vibrational modes	Line assignment
1609	CC ring stretching, CN ring stretching	$\nu_{\text{ring}}(\text{C-C}) + \nu(\text{C-N})$
1595	Ring stretching, CH wagging	$\nu_{\text{ring}} + \delta(\text{C-H})$
1507	Ring stretching	ν_{ring}
1478	CH wagging, ring stretching	$\delta(\text{C-H}) + \nu_{\text{ring}}$
1471	CH wagging, ring stretching	$\delta(\text{C-H}) + \nu_{\text{ring}}$
1424	CH wagging, ring stretching	$\delta(\text{C-H}) + \nu_{\text{ring}}$
1396	CH wagging, ring stretching	$\delta(\text{C-H}) + \nu_{\text{ring}}$
1331	Ring stretching, CO stretching, CH wagging	$\nu_{\text{ring}} + \nu(\text{C-O}) + \delta(\text{C-H})$
1285	CO stretching, CH wagging	$\nu(\text{C-O}) + \delta(\text{C-H})$
1245	CN stretching, CH wagging	$\nu(\text{C-N}) + \delta(\text{C-H})$
1236	CN stretching, CH wagging	$\nu(\text{C-N}) + \delta(\text{C-H})$
1223	CN stretching, CH wagging	$\nu(\text{C-N}) + \delta(\text{C-H})$
1213	CN stretching, CH wagging	$\nu(\text{C-N}) + \delta(\text{C-H})$
1177	CH wagging	$\delta(\text{C-H})$
1132	CH wagging	$\delta(\text{C-H})$
1115	CO stretching, CH wagging	$\nu(\text{C-O}) + \delta(\text{C-H})$
1054	Ring stretching, CH wagging	$\nu_{\text{ring}} + \delta(\text{C-H})$
1035	Ring stretching, CH wagging	$\nu_{\text{ring}} + \delta(\text{C-H})$

Continued Table 2

ν, cm^{-1}	Vibrational modes	Line assignment
1001	CH wagging	$\delta_{\text{wagging}}(\text{C-H})$
981	Ring deformation	RD
956	CH wagging	$\delta_{\text{wagging}}(\text{C-H})$
919	Ring deformation, AlN stretching	$RD + \nu(\text{Al-N})$
860	CH wagging	$\delta_{\text{wagging}}(\text{C-H})$
822	CH wagging	$\delta_{\text{wagging}}(\text{C-H})$
802	Ring deformation	RD
795	CH wagging	$\delta_{\text{wagging}}(\text{C-H})$
750	Breathing, ring	$\nu_{\text{ring}}(\text{breathing})$
740	AlN stretching	$\nu(\text{Al-N})$
656	CH wagging	$\delta_{\text{wagging}}(\text{C-H})$
649	AlO stretching, ring deformation	$\nu(\text{Al-O}) + RD$
625	AlO, AlN stretching, ring deformation	$\nu(\text{Al-O}) + \nu(\text{Al-N}) + RD$
591	CH torsion	$(\text{C-H})_{\text{torsion}}$
570	Ring deformation, AIOC wagging	$RD + \delta(\text{Al-O-C})$
548	AlO, AlN stretching, ring deformation	$\nu(\text{Al-O}) + \nu(\text{Al-N}) + RD$
540	AlO, AlN stretching, ring deformation	$\nu(\text{Al-O}) + \nu(\text{Al-N}) + RD$
523	Ring deformation, AlO stretching	$RD + \nu(\text{Al-O})$
504	Ring deformation	RD
470	Ring deformation	RD
460	CH torsion	$(\text{C-H})_{\text{torsion}}$
445	CH torsion	$(\text{C-H})_{\text{torsion}}$
420	AlN stretching, AIOC wagging	$\nu(\text{Al-N}) + \delta(\text{Al-O-C})$
405	ring deformation, AlO stretching	$RD + \nu(\text{Al-O})$
393	ring deformation, AlN stretching	$RD + \nu(\text{Al-N})$
353	ring deformation, AIOC wagging	$RD + \delta(\text{Al-O-C})$
302	AlN stretching, CCO wagging	$\nu(\text{Al-N}) + \delta(\text{C-C-O})$
295	Ring torsion	RT
288	Ring torsion	RT
282	Ring torsion	RT
227	Ring wagging	$\delta_{\text{wagging}}(\text{C-C})$
210	Ring wagging	$\delta_{\text{wagging}}(\text{C-C})$

Table 3. Line frequencies in the Raman spectrum (Fig. 6, spectrum 2) and correlation of vibrational modes HQ

ν, cm^{-1}	Vibrational modes	Line assignment
1609	CC ring stretching, CH wagging	$\nu_{\text{ring}}(\text{C-C}) + \delta(\text{C-H})$
1590	CC ring stretching, CH wagging	$\nu_{\text{ring}}(\text{C-C}) + \delta(\text{C-H})$
1480	CC ring stretching	$\nu_{\text{ring}}(\text{C-C})$
1437	OH wagging, CC stretching	$\delta(\text{O-H}) + \nu_{\text{ring}}(\text{C-C})$
1410	CC stretching, CC wagging	$\nu_{\text{ring}}(\text{C-C}) + \delta(\text{C-C})$
1387	CC stretching, CC wagging	$\nu_{\text{ring}}(\text{C-C}) + \delta(\text{C-C})$
1352	CC stretching, CO stretching, CH wagging	$\nu_{\text{ring}} + \nu_{\text{ring}}(\text{C-O}) + \delta(\text{C-H})$
1281	CH wagging, CN stretching	$\delta(\text{C-H}) + \nu_{\text{ring}}(\text{C-N})$
1263	CH wagging	$\delta(\text{C-H})$
1232	CC stretching	$\nu_{\text{ring}}(\text{C-C})$
1212	CN, CO stretching	$\nu_{\text{ring}}(\text{C-N}) + \nu_{\text{ring}}(\text{C-O})$
1170	CH wagging	$\delta(\text{C-H})$
1140	CH wagging	$\delta(\text{C-H})$

Continued Table 3

ν , cm^{-1}	Vibrational modes	Line assignment
1106	CC stretching, CH wagging	$\nu_{\text{ring}}(\text{C-C}) + \delta(\text{C-H})$
1067	CH wagging	$\delta_{\text{wagging}}(\text{C-H})$
1040	CH wagging	$\delta_{\text{wagging}}(\text{C-H})$
957	CH wagging	$\delta_{\text{wagging}}(\text{C-H})$
900	CH wagging	$\delta_{\text{wagging}}(\text{O-H})$
896	CH wagging	$\delta_{\text{wagging}}(\text{C-H})$
872	CH wagging	$\delta_{\text{wagging}}(\text{C-H})$
825	Ring wagging	$\delta_{\text{bending}}(\text{C-C})$
814	Ring deformation	RD
780	CH, OH wagging	$\delta_{\text{wagging}}(\text{C-H}) + \delta_{\text{wagging}}(\text{O-H})$
752	Breathing, ring wagging	$\delta_{\text{bending}}(\text{C-C})$
723	Ring torsion	RT
644	Breathing, ring stretching, CH wagging	$\nu_{\text{ring}} + \delta(\text{C-H})$
585	CO, CH wagging	$\delta(\text{C-O}) + \delta(\text{C-H})$
553	Ring deformation	RD
493	Ring torsion and deformation	$RT + RD$
479	CO wagging	$\delta_{\text{wagging}}(\text{C-O})$
272	Ring torsion	RT
180	Ring torsion	RT
167	Ring torsion	RT

The modes between 1609 and 1035 cm^{-1} are mainly due to the stretching of C–C bonds of hydroxyquinoline rings and the bending vibrations of C–H bonds (C–H rocking plane vibration, scissor vibration). The characteristic lines in Alq_3 spectrum (Fig. 6, spectrum 1) at 1595 and 1396 cm^{-1} correspond to the vibrational modes of the aromatic ring [$\nu_{\text{ring}} + \delta(\text{C-H})$] of 8-hydroxyquinolate (HQ) ligand, while in the Raman spectrum of HQ (Fig. 6, spectrum 2) the last peak is shifted to shorter wavelengths and has a maximum at 1387 cm^{-1} . Stretching vibrations of the C–C bond, accompanied by rocking and shear vibrations of the C–H bond are responsible for the lines at 1478–1396 cm^{-1} . In the region of 1213–1285 cm^{-1} , stretching vibrations of C–N and C–O bonds are observed. The lines at 1177 and 1132 cm^{-1} are attributed to wagging vibrations of C–H bonds. The lower frequency line at 750 cm^{-1} belongs to the mode characterizing Al–O vibrations and breathing vibrations of the benzene and pyridine rings. The spectra of coordination compounds at wave numbers around 740 cm^{-1} exhibit vibrations of Al–N bonds [17], which are absent in the spectrum of the original HQ. The modes at 625, 548, 540 and 530 cm^{-1} correspond to combined vibrations [$\nu(\text{Al-O}) + \nu(\text{Al-N}) + \delta_{\text{ring}}$]; the modes at 504 and 470 cm^{-1} correspond to vibrations of ring deformations. According to [18], vibrations indicating the formation of Al–O chemical bonds in

hydroxyquinolate molecules appear in the range of 500–520 cm^{-1} . The line at 570 cm^{-1} refers to wagging vibrations of the benzene and pyridine rings and torsional vibrations of Al–O–C. The line at 520 cm^{-1} is attributed to vibrations of Al–O bond stretching and deformation of hydroxyquinoline fragments attached to metal atoms (breathing vibration of benzene and pyridine rings). The frequency of the Al–O stretching vibration mode at 520 cm^{-1} is in satisfactory agreement with the observed value of 523 cm^{-1} , which characterizes the meridional isomer. In turn, this value for the *fac*-isomer is 534 cm^{-1} [19]. Torsional vibrations of Al–O and wagging vibrations of the benzene and pyridine rings are characterized by the line at 504 cm^{-1} . The vibrational mode observed at 750 cm^{-1} can be attributed to the breathing mode of the HQ fragment, while the line at 802 cm^{-1} is attributed to the deformation mode of the HQ ring [20]. The lines at 591, 460 and 445 cm^{-1} characterize the torsional vibrations of the C–H bond. The line at 405 cm^{-1} can be attributed to vibrations of ring deformation and Al–O bond stretching.

The Raman spectrum of HQ (Table 3) has a more pronounced vibrational structure compared to Alq_3 spectrum (Fig. 6, spectrum 2). Symmetrical vibrations of aromatic rings are characterized by high intensity. Thus, symmetrical vibrations of C–C bonds are active in the regions of 1590 and 1410 cm^{-1} .

The peak at 1480 cm^{-1} characterizes the C–C bond stretching mode. The HQ vibration peak located at 1437 cm^{-1} is characterized by $\delta(\text{C–O–H})$ wagging and C–C bond stretching modes. Three intense bands at 1352 , 1387 and 1437 cm^{-1} characterize vibrations of ring stretching, C–O bonds, and wagging of O–H bonds. The HQ peak located at 1281 cm^{-1} is characterized by C–H bond wagging and C–N stretching modes. The peak at 1232 cm^{-1} characterizes the stretching vibrations of C–C bonds, and at 1212 cm^{-1} it characterizes the stretching vibrations of C–N and C–O bonds. The vibration lines at 800 and 550 cm^{-1} are attributed to the HQ ring deformation mode [20]. The line at 752 cm^{-1} is attributed to the HQ breathing mode. The band at 723 cm^{-1} corresponds to highly symmetrical vibrations of the quinoline rings [21]. The spectrum contains a band at 644 cm^{-1} , which characterizes vibrations of ring stretching and wagging of C–H bonds. The lines at 585 and 479 cm^{-1} are responsible for the stretching vibrations of C–O bonds. The bands at 272 , 180 and 167 cm^{-1} are responsible for the torsional vibrations of the quinoline rings.

3.3. Spectrophotometric study of Alq₃ solvents

UV-visible absorption spectroscopy has been used to characterize solvents of Alq₃ in various organic solvents [22–26]. The spectra were obtained under the same conditions. Figure 7 shows the UV/VIS absorption spectra of Alq₃ in the short-wavelength region of the spectrum in the following solvents: EtOH, *i*-PrOH, TEP, toluene.

Solvents of α -Alq₃ absorb significantly in the UV region and have several absorption lines here. Table 4 shows the spectral characteristics of α -Alq₃

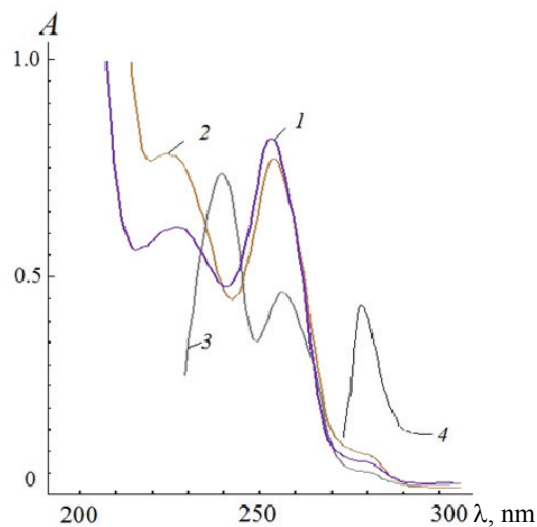


Fig. 7. UV/VIS absorption spectra of Alq₃ ($C = 8.0 \cdot 10^{-6}\text{ M}$) in organic solvents: EtOH (1), *i*-PrOH (2), TEP (3), toluene (4)

($C = 8.0 \cdot 10^{-6}\text{ M}$) in various solvents in the UV region of the spectrum. The lines of electronic transitions are located in the mid-UV region from 226 to 285 nm. The clearest absorption line is observed at 255–258 nm and has ε_{max} from ~ 59000 to $102000\text{ L}\cdot(\text{mol}\cdot\text{cm})^{-1}$.

Figure 8 shows the absorption spectra in the range of 300–500 nm of solvents of α -Alq₃ (sample IV) with a concentration of $C = 1.7 \cdot 10^{-4}\text{ M}$ in eight solvents: DMSO, CH₃CN, EtOH, *i*-PrOH, TEP, CHCl₃, 1,4-dioxane, toluene.

Table 5 shows the spectral characteristics of α -Alq₃ in various solvents ($C = 1.7 \cdot 10^{-4}\text{ M}$) in the wavelength range of 300–500 nm. The spectra contain two bands with insignificant absorption: $\lambda_{\text{max}}^{\text{I}}$ is in the range of 315–320 nm, ε^{I} takes values from 2676 to 4765 $\text{L}\cdot(\text{mol}\cdot\text{cm})^{-1}$; $\lambda_{\text{max}}^{\text{II}}$ is in the range of 330–335 nm and ε^{II} takes values from 2824 to 4412 $\text{L}\cdot(\text{mol}\cdot\text{cm})^{-1}$ (Table 4).

Table 4. Spectral characteristics of α -Alq₃ ($C = 8.0 \cdot 10^{-6}\text{ M}$) in various solvents

$\lambda_{\text{max}}, \text{ nm} / A$	EtOH	<i>i</i> -PrOH	TEP	Toluene
$\lambda_{\text{max}}^{\text{I}}, \text{ nm} / A^{\text{I}}$	228 / 0.62	226 / 0.78	241 / 0.74	
$\varepsilon^{\text{I}}, \text{ L}\cdot(\text{mol}\cdot\text{cm})^{-1}$	77500	97500	92500	
$\lambda_{\text{max}}^{\text{II}}, \text{ nm} / A^{\text{II}}$	255 / 0.82	255 / 0.77	258 / 0.47	
$\varepsilon^{\text{II}}, \text{ L}\cdot(\text{mol}\cdot\text{cm})^{-1}$	102500	96250	58750	
$\lambda_{\text{max}}^{\text{III}}, \text{ nm} / A^{\text{III}}$	285 / 0.13*	285 / 0.11*	285 / 0.10*	283 / 0.43
$\varepsilon^{\text{III}}, \text{ L}\cdot(\text{mol}\cdot\text{cm})^{-1}$	16250	13750	12500	53750
* shoulder.				

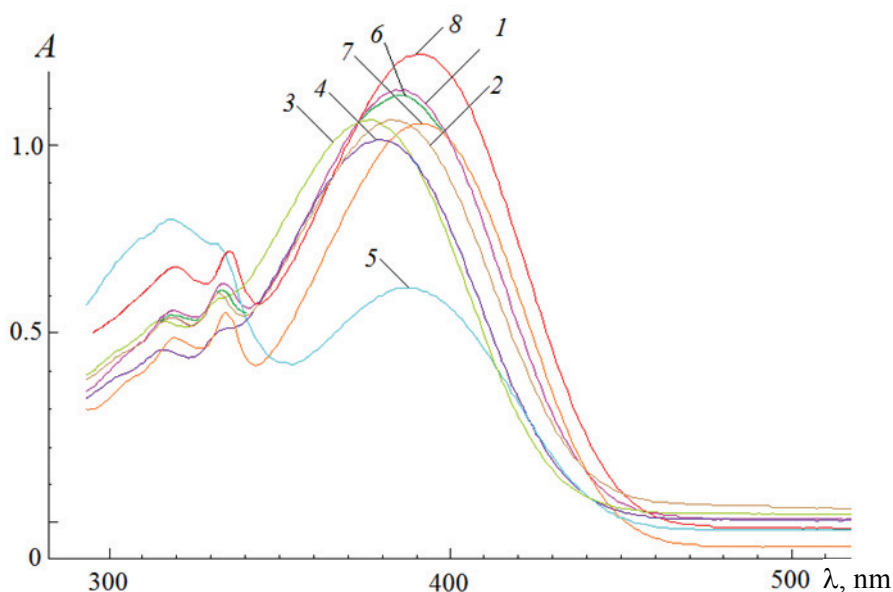


Fig. 8. UV/VIS absorption spectra of Alq₃ in the visible region of the spectrum ($C = 1.7 \cdot 10^{-4}$ M) in organic solvents: DMSO (1), CH₃CN (2), EtOH (3), *i*-PrOH (4), TEP (5), CHCl₃ (6), 1,4-dioxane (7), toluene (8)

Table 5. Spectral characteristics of α -Alq₃ ($C = 1.7 \cdot 10^{-4}$ M) in various solvents

λ_{\max} , nm / A	DMCO	CH ₃ CN	EtOH	<i>i</i> -PrOH	TEP**	CHCl ₃	1,4-dioxane	Toluene
Rel. diel. solvent permeability, ϵ	46.7	37.5	24.6	17.9	8	4.8	2.3	2.4
Dipole moment μ , D	3.9	3.45	1.68	1.66	3.03	1.15	0.45	0.43
λ_{\max}^I , nm / A^I	319 / 0.56	317 / 0.54	315 / 0.50	317 / 0.46	318 / 0.81	318 / 0.52	319 / 0.49	320 / 0.68
ϵ^I , L·(mol·cm) ⁻¹	3294	3159	2912	2676	4765	3024	2882	4000
λ_{\max}^{II} , nm / A^{II}	333 / 0.63	332 / 0.61	330 / 0.51*	330 / 0.48*	332 / 0.75	334 / 0.55	334 / 0.56	335 / 0.72
ϵ^{II} , L·(mol·cm) ⁻¹	3706	3565	3000	2824	4412	3206	3294	4235
λ_{\max}^{III} , nm / A^{III}	386 / 1.15	383 / 1.07	375 / 0.98	379 / 1.02	388 / 0.62	386 / 1.06	392 / 1.06	391 / 1.24
ϵ^{III} , L·(mol·cm) ⁻¹	6765	6265	5782	5965	3647	6206	6235	7294

* – shoulder; ** – triethylphosphate.

These bands correspond to $\pi \rightarrow \pi^*$ electronic transitions, which is due to the presence of double bonds in the ligand molecule.

Under the influence of a polar solvent, the absorption maxima caused by $\pi \rightarrow \pi^*$ transitions shift to the bathochromic (red) side. However, it is impossible to establish an unambiguous pattern in the systems under consideration. Thus, in the most polar solvent we are considering, in DMSO, $\lambda_{\max}^I = 319$ nm, and in toluene $\lambda_{\max}^I = 320$ nm. The situation is similar with the values of λ_{\max}^{II} .

The absorption bands that appear at higher wavelengths in the range 375–392 nm correspond to

$n \rightarrow \pi^*$ electronic transitions and can be classified as ligand-centered electronic transitions. These lines are characterized by a molar extinction coefficient in the range of 3647–7294 L·(mol·cm)⁻¹. In polar solvents, such absorption lines should shift hypsochromically to the blue region of the spectrum. However, for Alq₃ an unambiguous conclusion about the dependence of the shift of absorption lines on the polarity of the solvent cannot be made.

Electronic $n \rightarrow \pi^*$ transitions are a consequence of the presence of heteroatoms with a lone electron pair in the ligand structure. They are realized as a result of electron density transfer from the highest

occupied molecular orbital (HOMO), which is mainly localized on the phenoxy ring of HQ ligands, to the lowest unoccupied molecular orbital (LUMO) located on the pyridine ring.

As is known, with increasing solvent polarity, characterized by the Kirkwood function ($\epsilon - 1/2\epsilon + 1$), the lines of $\pi \rightarrow \pi^*$ transitions shift bathochromically due to greater stabilization of more polar excited states in comparison with the ground states; polar proton-donor solvents cause a blue shift of $n \rightarrow \pi^*$ transitions due to greater stabilization of the ground state due to the formation of complexes with hydrogen bonds. Apparently, the intermolecular interaction of Alq₃ in solvents of organic solvents (Sol) is of decisive importance. The nature of Alq₃-Sol intermolecular interactions ultimately determines the spectral characteristics of Alq₃ solvents.

Figure 8 shows characteristic α -Alq₃ absorption lines with maxima in the intervals: $\lambda_{\max}^{\text{I}} = 315\text{--}320$, $\lambda_{\max}^{\text{II}} = 330\text{--}335$ and $\lambda_{\max}^{\text{III}} = 375\text{--}392$ nm. The spectra were obtained for sample IV with a concentration of $C = 1.7 \cdot 10^{-4}$ M. The molar extinction coefficients are in the range: for $\lambda_{\max}^{\text{I}} = 2676\text{--}4765$, for $\lambda_{\max}^{\text{II}} = 2824\text{--}4412$ and for $\lambda_{\max}^{\text{III}} = 3647\text{--}7294$. For comparison, according to [27], a solvent of Alq₃ in CH₂Cl₂ at $\lambda_{\max} = 388$ nm is characterized by the value $\epsilon^{388} = 7000 \text{ L} \cdot (\text{mol} \cdot \text{cm})^{-1}$.

In this case, it should also be noted that with a decrease in the polarity of the solvents (from DMSO to toluene), no clearly defined bathochromic shift is observed in the absorption spectra. As a result of the solvatochromic effect, a change in the position and intensity of the absorption lines characteristic of Alq₃

quinoline ligands can be observed. Table 5 shows the wavelengths and intensities of the corresponding absorption lines.

3.4. Quantitative determination of Alq₃ in *i*-PrOH solvent

To carry out quantitative analyzes of Alq₃ solvents by the spectrophotometric method and standardize its solvents in organic solvents, a series of dilutions of a standard Alq₃ sample in *i*-PrOH was prepared in the concentration range $(1.6\text{--}15.0) \cdot 10^{-5}$ M, at which the Bouguer-Lambert-Beer law is observed. Figure 9 demonstrates the spectra of a series of dilutions of Alq₃ solvents in *i*-PrOH. Table 6 shows the data for constructing the calibration line $A = fC(\alpha\text{-Alq}_3)$ in *i*-PrOH at the analytical wavelength $\lambda_{\max} = 379$ nm.

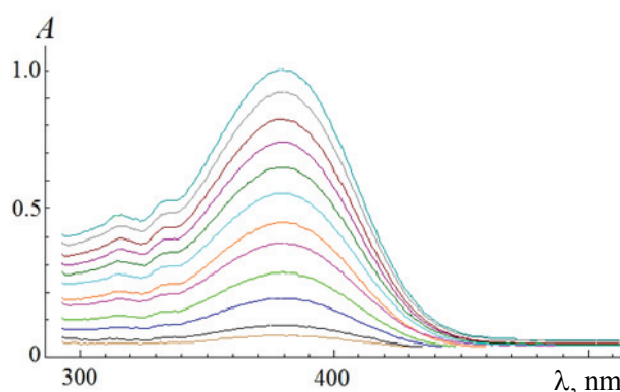


Fig. 9. UV/VIS absorption spectra of α -Alq₃ in *i*-PrOH for constructing a calibration line at $\lambda_{\max} = 379$ nm

Table 6. Data for constructing the calibration line $A = fC(\alpha\text{-Alq}_3)$ in *i*-PrOH at $\lambda_{\max} = 379$ nm. Calibration chart is on insert

A	$C \cdot 10^5, \text{M}$	A
0.08	1.57	
0.18	3.10	
0.27	4.58	
0.38	6.02	
0.45	7.41	
0.56	8.76	
0.65	10.07	
0.74	11.35	
0.82	12.59	
0.92	13.79	
1.00	14.97	

The findings show the possibility of standardizing solvents of α -Alq₃ in organic solvents and its quantification in solvents.

4. Conclusion

This work proposes a simple and original synthesis of the *mer*-isomer of the α -polymorphic modification of tris(8-hydroxyquinolate) aluminum. The phase composition of the α -phase *mer*-Alq₃ powder obtained by the new method was determined by X-ray diffraction analysis and is in good agreement with the results of Raman spectroscopy. The spectroscopic characteristics of Alq₃ in various solvents were studied. The spectrum of Alq₃ in triethyl phosphate (TEP) is of greatest interest. The spectrum is characterized by the presence of a strong absorption line at 318 nm, the intensity of which is higher than the absorption line at 388 nm. In all other solvents used in the work, the opposite picture was observed. One of the reasons for this behavior may be the formation of Alq₃-TEP complexes (solvates). The specific behavior of the Alq₃ molecule in the solvent is determined by the specific and universal solvation centers present in its structure. In accordance with the types of intermolecular interactions, it is customary to distinguish nonspecific solvation, caused by van der Waals interactions, and specific solvation, which manifests itself as a result of electrostatic interactions, coordination and hydrogen bonds. The stability of specific solvates in the Alq₃-TEP system and, as a consequence, the shape of the absorption spectrum, can be influenced by the viscosity of the solvent. In addition, in viscous solvents, the mutual transformations of different solvates are difficult. All new facts and observations obtained in this work require detailed study and explanation, which will serve as a topic for further research.

5. Funding

This study received no external funding.

6. Acknowledgements

Thanks to G.A. Gevorgyan for conducting research using a scanning electron microscope; S.S. Arsentiev, I.V. Kuzmin for participation in the processing of experimental data.

7. Conflict of interests

The authors declare no conflict of interest.

References

1. Tang CW, VanSlyke SA. Organic electroluminescent diodes. *Applied Physics Letters*. 1987;51(12):913-915. DOI:10.1063/1.98799
2. Costa JCS, Lima CFRAC, Santos LMNBF. Electron transport materials for organic light-emitting diodes: understanding the crystal and molecular stability of the tris(8-hydroxyquinolines) of Al, Ga, and In. *The Journal of Physical Chemistry C*. 2014;118(38):21762-21769. DOI:10.1021/jp503935k
3. Hongze G, Zhang H, Zhang H, Gen Y, Su ZM. Theoretical study of isomerism/phase dependent charge transport properties in tris(8-hydroxyquinolino) aluminum(III). *The Journal of Physical Chemistry A*. 2011;115(33):9259-9264. DOI:10.1021/jp202976m
4. Rajeswaran M, Blanton TN, Tang CW. et al. Structural, thermal, and spectral characterization of the different crystalline forms of Alq₃, tris(quinolin-8-olato) aluminum(III), an electroluminescent material in OLED technology. *Polyhedron*. 2009;28(4):835-843. DOI:10.1016/J.POLY.2008.12.022
5. Cherednichenko AG, Avetisov RI, Akkuzina AA, Avetisov IH. Study of the processes of synthesis and purification of aluminum, gallium and indium tri-(8-hydroxyquinolates) for the technology of organic light-emitting devices. *Vestnik Kazanskogo tekhnologicheskogo universiteta*. 2015;18(10):52-54. (In Russ.)
6. Avetisov RI, Akkuzina AA, Cherednichenko AG, Khomyakov AV, Avetisov IC. Polymorphism of tris(8-hydroxyquinoline) aluminum, gallium, and indium. *Doklady akademii nauk = Doklady Chemistry*. 2014;454(1):6-8. DOI:10.1134/S0012500814010029
7. Avetisov R, Kazmina K, Barkanov A. et al. One-step synthesis of high pure tris(8-hydroxyquinoline) aluminum for optics and photonics. *Materials (Basel)*. 2022;15(3):734-741. DOI:10.3390/ma15030734
8. Kazmina KV, Pytchenko AA, Li YaR, Tonova LD, Zakharova AV, Myagkova EV, Tashlintseva SA, Zykova MP, Avetisov RI. Synthesis and luminescent properties of aluminum tri-(8-hydroxyquinolate). *Uspekhi v khimii i khimicheskoy tekhnologii*. 2021;35(6):43-46. (In Russ.)
9. Katakura R, Koide Y. Configuration-specific synthesis of the facial and meridional isomers of tris(8-hydroxyquinolate)aluminum (Alq₃). *Inorganic Chemistry*. 2006;45(15):5730-5732. DOI:10.1021/ic060594s
10. Rulfs CL. A text-book of quantitative inorganic analysis including elementary instrumental analysis. *Inorganic Chemistry*. 1962;1(3):723-724. DOI:10.1021/ic50003a063
11. Painuly D, Mogha NK, Masram DT. et al. Phase stability and transformation of the α to ϵ -phase of Alq₃ phosphor after thermal treatment and their photo-physical properties. *Journal of Physics and Chemistry of Solids*. 2018;121:396-408. DOI:10.1016/j.jpcs.2018.05.035
12. Brinkmann M, Gadret G, Muccini M. et al. Correlation between molecular packing and optical properties in different crystalline polymorphs and amorphous thin films of *mer*-tris(8-hydroxyquinoline)

aluminum(III). *Journal of the American Chemical Society*. 2000;122:5147-5157. DOI:10.1021/JA993608K

13. Rajeswaran M, Blanton TN, Tang CW. et al. Structural, thermal, and spectral characterization of the different crystalline forms of Alq₃, tris(quinolin-8-olato) aluminum(III), an electroluminescent material in OLED technology. *Polyhedron*. 2009;28(4):835-843. DOI:10.1016/j.poly.2008.12.022

14. Fukushima T, Kaji H. Green- and blue-emitting tris(8-hydroxyquinoline)aluminum(III) (Alq₃) crystalline polymorphs: Preparation and application to organic light-emitting diodes. *Organic Electronics*. 2012;13(12):2985-2990. DOI:10.1016/j.orgel.2012.08.036

15. Rajeswaran M, Blanton TN. Single-crystal structure determination of a new polymorph (ϵ -Alq₃) of the electroluminescence OLED (organic light-emitting diode) material, tris(8-hydroxyquinoline)aluminum (Alq₃). *Journal of Chemical Crystallography*. 2005;35(1):71-76. DOI:10.1007/s10870-005-1157-4

16. Halls MD, Aroca R. Vibrational spectra and structure of tris(8-hydroxyquinoline)aluminum(III). *Canadian Journal of Chemistry*. 1998;76:1730-1736. DOI:10.1139/v98-182

17. Patel KD, Patel HS. Synthesis, spectroscopic characterization and thermal studies of some divalent transition metal complexes of 8-hydroxyquinoline. *Arabian Journal of Chemistry*. 2013;10:S1328-S1335. DOI:10.1016/j.arabj.2013.03.019

18. Hui L, Yuqin F, Linbo Z. et al. In situ route to novel fluorescent mesoporous silica nanoparticles with 8-hydroxyquinolate zinc complexes and their biomedical applications. *Microporous and Mesoporous Materials*. 2012;151:293-302. DOI:10.1016/j.micromeso.2011.10.021

19. Peng J, Zhang S-J, Wang K, Dove M. Density functional theory calculation of spectrum and excitation properties of mer-Alq₃. *Acta Physica Sinica*. 2020;69(2):023101. DOI:10.7498/aps.69.20191453

20. Dasi G, Lavanya T, Suneetha S, Vijayakumar S, Shim J-J, Thangaraju K. Raman and X-ray photoelectron

spectroscopic investigation of solution processed Alq₃/ZnO hybrid thin films. *Spectrochimica Acta Part A: Molecular and Biomolecular Spectroscopy*. 2022;265:120377. DOI:10.1016/j.saa.2021.120377

21. Sowa M, Wala M, Blacha-Grzechnik A. et al. Corrosion inhibitor-modified plasma electrolytic oxidation coatings on 6061 aluminum alloy. *Materials*. 2021;14(3):619. DOI:10.3390/ma14030619

22. Alzahrani H, Sulaiman K, Mahmoud AY, Bahabry RR. Study of organic visible-blind photodetector based on Alq₃:NPD blend for application in near-ultraviolet detection. *Optical Materials*. 2020;110:110490. DOI:10.1016/j.optmat.2020.110490

23. Alzahrani H, Sulaiman K, Muhammadsharif FF. et al. Effect of illumination intensity on a self-powered UV photodiode based on solution-processed NPD: Alq₃ composite system. *Journal of Materials Science: Materials in Electronics*. 2021;32:14801-14812. DOI:10.1007/s10854-021-06034-x

24. Omar WAE. Synthesis and photophysical properties of aluminium tris-(4-morpholine-8-hydroxyquinoline). *Journal of Advanced Research*. 2013;4(6):525-529. DOI:10.1016/j.jare.2012.09.003

25. Hoshi T, Kumagai K, Inoue K. et al. Electronic absorption and emission spectra of Alq₃ in solution with special attention to a delayed fluorescence. *Journal of Luminescence*. 2008;128(8):1353-1358. DOI:10.1016/j.jlumin.2008.01.003

26. Heiskanen JP, Tolkkio AE, Lemmetyinen HJ, Hormi OEO. Fused Alq₃ derivatives: syntheses and photophysical characteristics. *Journal of Materials Chemistry*. 2011;21(38):14766-14775. DOI:10.1039/c1jm12424b

27. Montes VA, Pohl R, Shinar J, Anzenbacher P. Effective manipulation of the electronic effects and its influence on the emission of 5-substituted tris(8-quinolinolate)aluminum(III) complexes. *Chemistry: A European Journal*. 2006;12(17):4523-4535. DOI:10.1002/chem.200501403

Information about the authors / Информация об авторах

Denis V. Belov, Cand. Sc. (Chem.), Associate Professor, Senior Researcher, Federal Research Center A.V. Gaponov-Grekhov Institute of Applied Physics of the Russian Academy of Sciences (IAP RAS), Nizhny Novgorod, Russian Federation; Leading Technologist, Institute of Physics of Microstructures of the Russian Academy of Sciences (IPM RAS), Nizhny Novgorod, Russian Federation; ORCID 0000-0001-7190-0477; e-mail: belov.denbel2013@yandex.ru

Sergey N. Belyaev, Cand. Sc. (Chem.), Researcher, Head of Laboratory, IAP RAS, Nizhny Novgorod, Russian Federation; Leading Technologist, IPM RAS, Nizhny Novgorod, Russian Federation; ORCID 0000-0003-2346-9103; e-mail: serg_belyaev@bk.ru

Белов Денис Владимирович, кандидат химических наук, доцент, старший научный сотрудник, Институт прикладной физики им. А. В. Гапонова-Грехова РАН (ИПФ РАН), Нижний Новгород, Российская Федерация; ведущий технолог, Институт физики микроструктур РАН (ИФМ РАН), Нижний Новгород, Российская Федерация; ORCID 0000-0001-7190-0477; e-mail: belov.denbel2013@yandex.ru

Беляев Сергей Николаевич, кандидат химических наук, научный сотрудник, заведующий лабораторией, ИПФ РАН, Нижний Новгород, Российская Федерация; ведущий технолог, ИФМ РАН, Нижний Новгород, Российская Федерация; ORCID 0000-0003-2346-9103; e-mail: serg_belyaev@bk.ru

Pavel A. Yunin, Cand. Sc. (Phys. and Math.), Sciences Researcher, Head of Laboratory, IPM RAS, Nizhny Novgorod, Russian Federation; ORCID 0000-0001-7081-2934; e-mail: yunin@ipmr.ru

Dmitry B. Radishev, Cand. Sc. (Phys. and Math.), Senior Researcher, IAP RAS, Nizhny Novgorod, Russian Federation; ORCID 0000-0002-8416-1738; e-mail: dibr@ipfran.ru

Юнин Павел Андреевич, кандидат физико-математических наук, научный сотрудник, заведующий лабораторией, ИФМ РАН, Нижний Новгород, Российская Федерация; ORCID 0000-0001-7081-2934; e-mail: yunin@ipmr.ru

Радищев Дмитрий Борисович, кандидат физико-математических наук, старший научный сотрудник, ИПФ РАН, Нижний Новгород, Российская Федерация; ORCID 0000-0002-8416-1738; e-mail: dibr@ipfran.ru

Received 26 July 2023; Accepted 10 October 2023; Published 15 December 2023



Copyright: © Belov DV, Belyaev SN, Yunin PA, Radishev DB, 2023. This article is an open access article distributed under the terms and conditions of the Creative Commons Attribution (CC BY) license (<https://creativecommons.org/licenses/by/4.0/>).

Multifunctional composite charcoal-containing microwave and X-ray radiation absorbers

© Olga V. Boiprav^a✉, Vadim A. Bogush^a, Nikolay N. Grinchik^b

^a Belarusian State University of Informatics and Radioelectronics,
6, P. Brovki St., Minsk, 220013, Belarus,

^b Institute of Heat and Mass Transfer named after A.V. Lykov
National Academy of Sciences of Belarus, 15, P. Brovki St., Minsk, 220072, Belarus

✉ smu@bsuir.by

Abstract: The article presents multifunctional composite absorbers of microwave and X-ray electromagnetic radiation proposed and developed by authors. Compared with the analogs, these absorbers contain powdered activated charcoal as the component absorbing microwave electromagnetic radiation energy and powdered barium sulfate as the component absorbing X-ray electromagnetic radiation energy. The absorbers are three-layer ones. It was established that microwave electromagnetic radiation absorption coefficient values of the absorbers containing the powdered activated birch charcoal vary from 0.5 rel. units up to 0.92 rel. units in the frequency bands 3.5–7.0 GHz, 10.8–14.2 GHz, and microwave electromagnetic radiation absorption coefficient values of the absorbers containing the powdered activated coconut charcoal vary within the specified limits in the frequency bands 5.0–7.5 GHz, 10.2–17.0 GHz. The values of X-ray attenuation coefficient provided by the absorbers vary from 2.0 to 8.7 rel. units. These absorbers can be used to cover the walls of rooms where X-ray machines are located. This will ensure a reduction in the degree of influence on these devices, as well as computer equipment connected to them, of microwave electromagnetic radiation from external sources, as well as a reduction in the degree of influence of X-ray radiation generated by these devices on electronic devices and on people who are outside the specified rooms.

Keywords: absorption coefficient; powdered activated charcoal; microwave electromagnetic radiation; X-ray electromagnetic radiation; barium sulfate.

For citation: Boiprav OV, Bogush VA, Grinchik NN. Multifunctional composite charcoal-containing microwave and X-ray radiation absorbers. *Journal of Advanced Materials and Technologies*. 2023;8(4):294-303. DOI: 10.17277/jamt.2023.04.pp.294-303

Многофункциональные композиционные углеродсодержащие поглотители микроволнового и рентгеновского электромагнитного излучения

© О. В. Бойправ^a✉, В. А. Богуш^a, Н. Н. Гринчик^b

^a Белорусский государственный университет информатики и радиоэлектроники,
ул. П. Бровки, 6, Минск, 220013, Республика Беларусь,

^b Институт тепло- и массообмена имени А. В. Лыкова Национальной академии наук Беларуси,
ул. П. Бровки, 15, Минск, 220072, Республика Беларусь

✉ smu@bsuir.by

Аннотация: Представлены многофункциональные композиционные поглотители микроволнового и рентгеновского электромагнитного излучения, предложенные и разработанные авторами. По сравнению с аналогами данные поглотители содержат порошкообразный активированный уголь в качестве компонента, обеспечивающего поглощение энергии микроволнового электромагнитного излучения, и порошкообразный сульфат бария в качестве компонента, обеспечивающего поглощение энергии рентгеновского электромагнитного излучения. Такие поглотители являются трехслойными. Установлено, что значения коэффициента поглощения микроволнового электромагнитного излучения поглотителей, содержащих порошкообразный активированный

березовый уголь, изменяются в пределах от 0,5 до 0,92 отн. ед. в полосах частот 3,5...7,0 ГГц, 10,8...14,2 ГГц, а значения коэффициента поглощения микроволнового электромагнитного излучения поглотителей, содержащих порошкообразный активированный кокосовый уголь, изменяются в указанных пределах в полосах частот 5,0...7,5 ГГц, 10,2...17,0 ГГц. Значения коэффициента ослабления рентгеновского излучения, обеспечиваемого поглотителями, изготовленными в соответствии с разработанной технологией, изменяются в пределах от 2,0 до 8,7 отн. ед. Данные поглотители могут быть использованы для покрытия стен помещений, где располагаются рентгеновские аппараты. При этом обеспечивается снижение степени влияния на эти аппараты и подключенные к ним средства вычислительной техники микроволнового электромагнитного излучения от внешних источников, а также снижение степени влияния рентгеновского излучения, генерируемого данными аппаратами, на приборы электронной техники и людей, которые находятся за пределами указанных помещений.

Ключевые слова: коэффициент поглощения; порошкообразный активированный уголь; микроволновое электромагнитное излучение; рентгеновское электромагнитное излучение; сульфат бария.

Для цитирования: Boiprav OV, Bogush VA, Grinchik NN. Multifunctional composite charcoal-containing microwave and X-ray radiation absorbers. *Journal of Advanced Materials and Technologies*. 2023;8(4):294-303. DOI: 10.17277/jamt.2023.04.pp.294-303

1. Introduction

Modern multifunctional materials that provide microwave electromagnetic radiation energy attenuation are characterized by the following properties: 1) thermal insulation [1–4]; 2) thermal conductivity [5, 6]; 3) sound insulation [3, 7]; 4) fire resistance [8, 9]; 5) optical transparency [3, 10]; 6) controllability of the electromagnetic radiation absorption coefficient (ERAC) value during absorber use [11]; 7) self-cleaning [1]; 8) self-healing [12].

Research interest in the development of multifunctional microwave electromagnetic radiation absorbers is increasing every year. This statement is based on information about the dynamics of changes in the share of scientific publications devoted to these absorbers from the number of scientific publications devoted to microwave electromagnetic radiation absorbers in general (Fig. 1).

We made the contribution to the research field devoted to the development of multifunctional

microwave electromagnetic radiation absorbers based on porous carbon-containing materials. This contribution consists in conducting the research aimed at the development and experimental validation of microwave and X-ray electromagnetic radiation absorbers. These absorbers were proposed and developed given the research results presented in [13, 14]. In particular, paper [13] presents composite building materials based on powdered charcoal and gypsum. It was shown that these materials provide 10.0–1000.0 times reduction of microwave electromagnetic radiation power. In [14] composite coatings based on powdered barium sulfate and sodium silicate aqueous alkaline solution were presented. It is shown that if the thickness of such coatings is 0.2 cm, then they are characterized by values of the X-ray attenuation coefficient of 2.0–8.7 rel. units (if X-ray electromagnetic radiation voltage values vary from 50.0 to 150.0 kV).

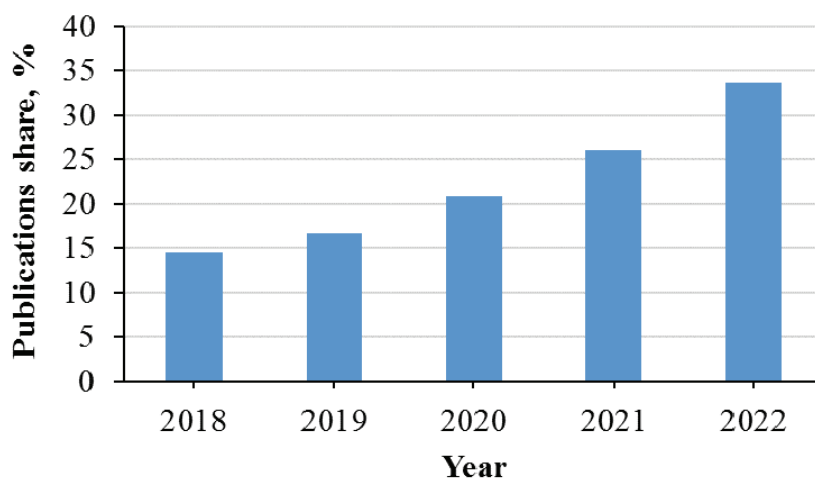


Fig. 1. Dynamics of changes in the share of scientific publications on multifunctional microwave electromagnetic radiation absorbers from the total number of those on microwave electromagnetic radiation absorbers

The urgency of the development of the indicated absorbers is due to the need to simultaneously solve two problems related to improving the conditions for the operation of X-ray machines: 1) reducing the impact of microwave electromagnetic radiation from external sources on X-ray machines, as well as computer equipment connected to them; 2) reducing the impact of radiation generated by X-ray machines on electronic devices and people who are outside the rooms where these devices are installed.

Thus, in this article, we developed and studied three-layer multifunctional composite absorbers of microwave and X-ray electromagnetic radiation. To achieve the set goal, the microwave electromagnetic radiation reflection coefficient (ERRC) and electromagnetic radiation transmission coefficient (ERTC) values of the made samples were measured; microwave ERAC values of the made samples were calculated; an analysis of the patterns of changes in the values of microwave ERAC of the made samples was carried out depending on the type of powdered activated charcoal that was used during their making.

2. Materials and Methods

2.1. Absorber production technology

The proposed absorbers were developed using the technology, comprising the following stages:

1. Cutting the (50.0 ± 5.0) microns thick foiled polymer film (KOTAR Ltd., Poland) into the fragments. Geometrical shape and size of the fragments should be relevant to the geometrical shape and size of the made absorber.

2. Cutting (0.2 ± 0.05) cm thick cellulose sheets (Spektr upakovki" factory, Belarus) into fragments.

Geometrical shape and size of the fragments should be relevant to the geometrical shape and size of the made absorber.

3. Preparing the mixture with following composition: powdered activated birch or coconut charcoal (trade mark BAU-A, standard 6217-74, Russia) or trade mark KAU-A (India), respectively – 20.0 vol. %, building gypsum (OJSC "BELGIPS", Belarus) – 30.0 vol. %, water – the rest.

4. Applying the (0.5 ± 0.1) cm thick layer of the mixture prepared during stage 3 to the one of the surfaces of the fragment of foiled polymer film cut during stage 4.

5. Preparing the mixture with the following composition: barium sulfate (OJSC "Chemical Plant named after L.Ya. Karpov", Russia) – 30.0 vol. %, sodium silicate aqueous alkaline solution (JSC "DEKART", Belarus) – the rest.

6. Applying the (0.2 ± 0.05) cm thick layer of mixture prepared during stage 5 to the one of the surfaces of the cellulose sheet fragment obtained during stage 2.

7. Fixing the cellulose sheet fragment with applied to it layer of mixture (stage 6) on the surface of the mixture applied during stage 4.

7. Drying the resulting absorber under standard conditions.

Thus, in this study, four groups of the samples were made in accordance with the presented technology.

The characteristics of the made samples are presented in Table 1. Schematic images of the made samples are presented in Fig. 2.

Table 1. Characteristics of the made samples

Name of the samples group	Composition of the sample first layer	Composition of the sample second layer	Composition of the sample third layer
Samples of group 1	Mixture of powdered activated birch charcoal, building gypsum and water	Foiled polymer film	No
Samples of group 2	Mixture of barium sulfate and sodium silicate aqueous alkaline solution	Mixture of powdered activated birch charcoal, building gypsum and water	Foiled polymer film
Samples of group 3	Mixture of powdered activated coconut charcoal, building gypsum and water	Foiled polymer film	No
Samples of group 4	Mixture of barium sulfate and sodium silicate aqueous alkaline solution	Mixture of powdered activated coconut charcoal, building gypsum and water	Foiled polymer film

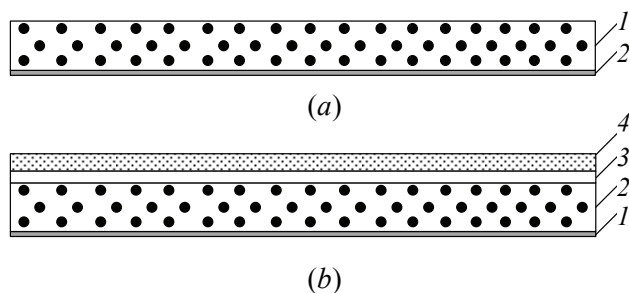


Fig. 2. Schematic images of the samples of groups 1 and 3 (a) and the samples of groups 2 and 4 (b):

1 – foiled polymer film; 2 – layer based on the mixture of powdered activated charcoal, building gypsum and water; 3 – cellulose sheet fragment; 4 – layer based on the mixture of barium sulfate and sodium silicate aqueous alkaline solution

As can be seen from Table 1 and Fig. 2, the made samples of groups 1 and 3 were two-layer ones, and the made samples of groups 2 and 4 were three-layer ones. Stages 1 and 3 of the proposed technology were used to make samples of groups 1 and 3, and 4. All stages of the proposed technology were used to make samples of groups 2 and 4. Samples of groups 1 and 3 were made to assess the degree of impact of adding the layer based on barium sulfate and sodium silicate aqueous alkaline solution to the structure of absorbers based on powdered activated charcoal on the microwave electromagnetic radiation reflection, transmission and absorption characteristics of such absorbers.

Ten samples of each group were made. The samples of each group were made in the specified quantity to create conditions for assessing the reproducibility of the results of implementing the presented technology (i.e., to assess the reproducibility of microwave ERRC, ERTC and ERAC characteristics of the absorbers made in accordance with the presented technology).

2.2. Determination of microwave ERRC, ERTC and X-ray attenuation coefficient

The microwave ERRC and ERTC of the made samples were studied using the measuring system including panoramic meter of electromagnetic radiation reflection and transmission coefficients SNA 0.01–18 (manufactured by Belarusian State University of Informatics and Radioelectronics), two horn antennas P6-23M, personal computer with special software for the measuring process management. The description of the method used in the course of the research was presented in [15]. The ERACs of the samples were calculated through the ERRC and ERTC. The calculation algorithm was described in detail in [15].

These measurements and calculations were carried out in the frequency range 2.0–17.0 GHz. This range was chosen because [16, 17]: frequencies of unwanted emissions of many modern radio-electronic devices belong to the specified range; modern devices for transmitting signals over wireless media operate in the specified range.

The X-ray attenuation coefficient of the made samples was studied using the measuring system including the X-ray calibration installation UPR-AT300 (“ATOMTECH” OJSC “MNIPI”, Belarus), the precision dosimeter DKS-AT5350 (“ATOMTECH” OJSC “MNIPI”, Belarus), the ionization chamber TM23361 (PTW Freiburg, Germany). The research methodology was described in detail in [14].

3. Results and Discussion

The ERAC frequency dependences in the range of 2.0–17.0 GHz for samples of groups 1 and 2 are presented in Fig. 3.

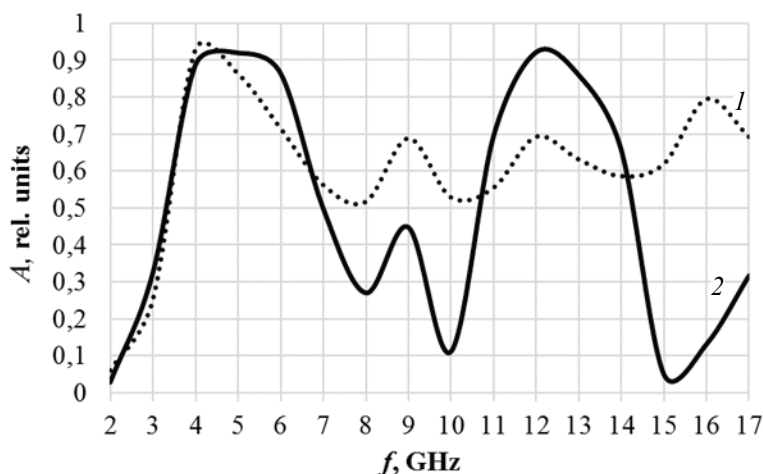


Fig. 3. ERAC frequency dependences in the range of 2.0–17.0 GHz of group 1 samples (curve 1) and group 2 samples (curve 2)

As can be seen from Fig. 3, the ERAC values in the frequency range 2.0–17.0 GHz for samples of groups 1 and 2 vary from 0.05 rel. units up to 0.92 rel. units. These samples are essentially frequency-selective microwave absorbers in the frequency range 2.0–17.0 GHz. Effective absorption band of samples of group 1 is 3.5–17.0 GHz. Effective absorption bands of samples of group 2 are 3.5–7.0 GHz, 10.8–14.2 GHz. That is, samples of group 1 are broadband microwave absorbers in the frequency range 2.0–17.0 GHz, and samples of group 2 are multiband microwave absorbers in the specified frequency range. ERAC values in the frequency bands 7.0–10.8 GHz and 14.2–17.0 GHz for samples of group 2 are lower by 0.1–0.55 rel. units than ERAC values in the indicated frequency bands of samples of group 1. This feature is due to the following:

- the ERRC values in the specified frequency bands of group 2 samples were higher by 2.0–8.0 dB than those of group 1 samples (see Fig. 4);

- the ERTC values in the specified frequency bands of groups 1 and 2 samples were practically equivalent (from –15.0 to –35.0 dB), which is due to the fact that this parameter value of the listed groups samples was influenced to the greatest extent by the foiled polymer film included in their structure.

The ERAC values in the frequency band 10.8–14.2 GHz for samples of group 2 were higher by 0.15–0.22 rel. units than the ERAC values in the specified frequency band of group 1 samples. This is due to the fact that the ERTC values in the specified frequency band of group 2 samples were lower by 1.0–7.0 dB than those of group 1 samples (see Fig. 4), provided that the ERTC values in the specified frequency band of these samples were almost completely equivalent.

The ERAC frequency dependences in the frequency range 2.0–17.0 GHz of groups 3 and 4 samples are presented in Fig. 5.

It is seen from Fig. 5 that the ERAC values in the frequency range 2.0–17.0 GHz for groups 3 and 4 samples vary from 0.1 rel. units up to 0.95 rel. units.

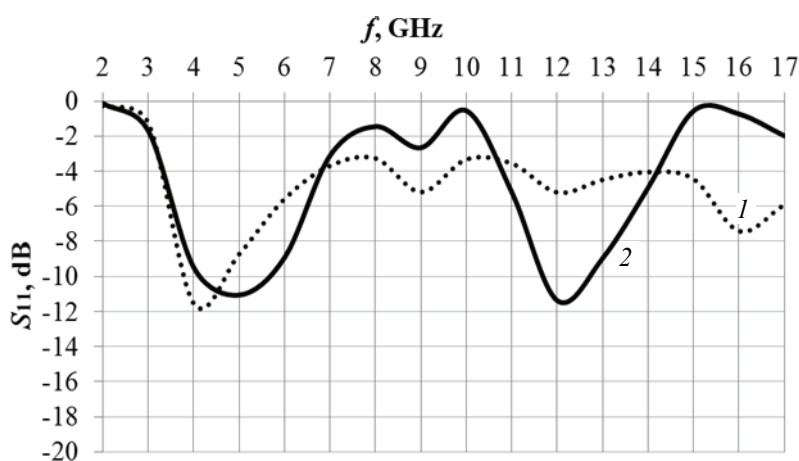


Fig. 4. ERRC frequency dependences in the range of 2.0–17.0 GHz of group 1 samples (curve 1) and group 2 samples (curve 2)

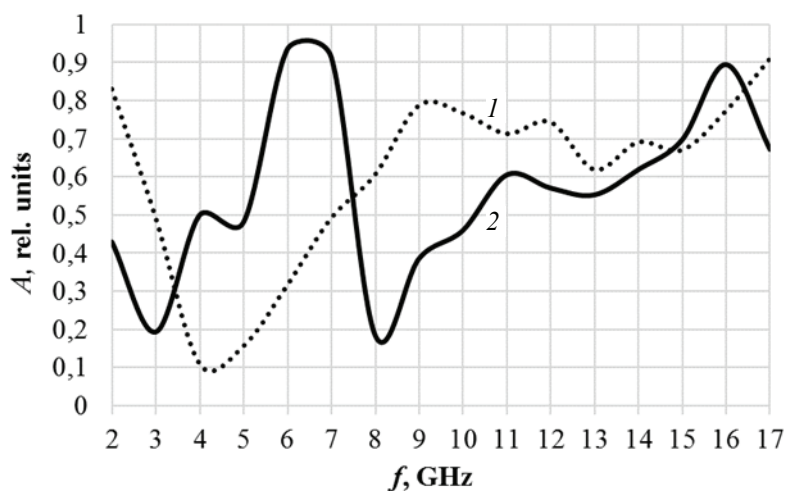


Fig. 5. ERAC frequency dependences in the range of 2.0–17.0 GHz of group 3 samples (curve 1) and group 4 samples (curve 2)

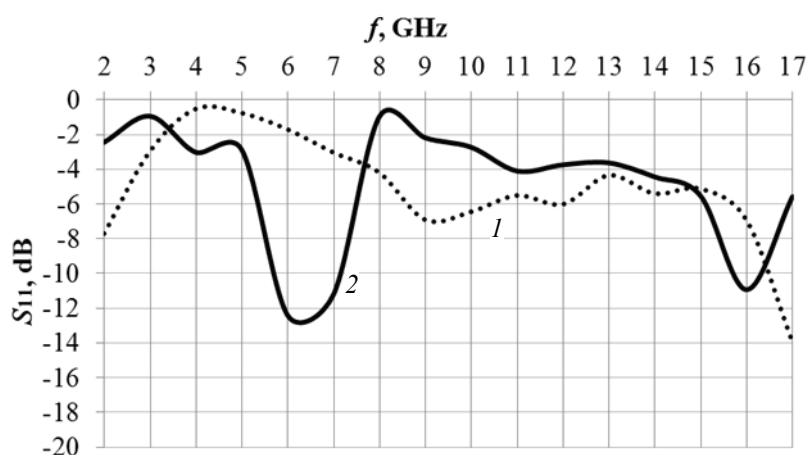


Fig. 6. ERRC frequency dependences in the range of 2.0–17.0 GHz of group 3 samples (curve 1) and group 4 samples (curve 2)

Effective absorption bands of group 3 samples are 2.0–3.0 GHz, 7.0–17.0 GHz. Effective absorption bands of group 4 samples are 5.0–7.5 GHz, 10.2–17.0 GHz. Groups 3 and 4 samples, like group 2 samples, are multiband microwave absorbers in the range of 2.0–17.0 GHz. The ERAC values in the frequency bands 2.0–3.0 GHz and 7.5–10.2 GHz for group 4 samples are lower by 0.1–0.4 rel. units than the ERAC values in the specified frequency bands of group 3 samples. This is due to the fact that the ERRC values in the specified frequency bands of group 4 samples are higher by 1.0–5.0 dB than the ERRC values in the specified frequency bands of group 3 samples (see Fig. 6), provided that the ERTC values in the specified frequency bands of these samples are almost completely equivalent. The ERAC values in the frequency bands 3.0–7.5 GHz and 15.0–16.5 GHz of samples of group 4 are higher by 0.1–0.55 rel. units than the ERAC values in the specified frequency bands of group 3 samples. This is due to the fact that the ERRC values in the specified frequency bands of group 4 samples are lower by 1.0–10.0 dB than the ERRC values in the specified frequency bands of group 3 samples (see Fig. 6), provided that the ERTC values in the specified frequency bands of these samples are almost completely equivalent.

The higher ERRC values of group 2 samples compared to those of group 1 samples in the frequency bands 7.0–10.8 GHz and 14.2–17.0 GHz and the higher ERRC values of group 4 samples compared to those of group 3 samples in frequency bands 2.0–3.0 GHz and 7.5–10.2 GHz are due to the following features of electromagnetic waves interaction with these samples:

1) electromagnetic waves reflected from the surfaces of the sample layers interact with each other;

2) the ERRC values of the samples depend on the value of energy of electromagnetic waves resulting from the interaction of electromagnetic waves reflected from the samples layers surfaces (if this energy is higher, electromagnetic radiation reflection coefficient values are higher; if this energy is lower, electromagnetic radiation reflection coefficient values are lower);

3) in the above frequency bands, the difference between the phases of electromagnetic waves reflected from the surfaces of the layers of groups 2 and 4 samples is smaller than the difference between the phases of electromagnetic waves reflected from the layer surface of groups 1 and 3 samples.

The lower ERRC values in the frequency band 10.8–14.2 GHz of group 2 samples compared to those of group 1 samples, and the lower ERRC values in the frequency bands 3.0–7.5 GHz and 15.0–16.5 GHz of group 4 samples compared to group 3 samples is due to features 1 and 2 described above, as well as the following feature:

– in the listed frequency bands, the difference between the phases of electromagnetic waves reflected from the layer surfaces of groups 2 and 4 samples is greater than the difference between the phases of electromagnetic waves reflected from the layer surface of groups 1 and 3 samples.

Table 2 presents the results of the study of X-ray attenuation coefficient of the made samples.

The proposed electromagnetic radiation absorbers are characterized by the ERAC values (A) and the width of the effective absorption band (Δf) similar to the ERAC values and the width of the effective absorption band of the analogs (microwave absorbers based on porous carbon-containing materials [18–23]) (see Table 3).

Table 2. Results of study of X-ray attenuation coefficient of the made samples

Average X-ray energy, keV	35.0	40.0	45.0	50.0	55.0	60.0	65.0	70.0	75.0	80.0
X-ray attenuation coefficient, rel. units	8.7	6.5	5.0	4.0	3.5	3.0	2.8	2.5	2.2	2.0

Table 3. Characteristics of microwave absorbers based on porous carbon-containing materials

Absorber name	d^* , cm	A , rel. units	Δf , GHz	f_c^{**} , GHz
Proposed absorbers containing powdered birch charcoal	0.9	0.5–0.92	3.5; 3.4	5.2; 12.5
Proposed absorbers containing powdered coconut charcoal	0.9	0.5–0.95	2.5; 6.8	6.2; 13.6
Absorbers based on porous carbon and carbon nanotubes [18]	0.5	$\sim 0.9^{***}$	1.5	15.5
Absorbers based on carbon obtained from wood [19]	0.5	0.5–0.9 ^{***}	6.0	9.0
Absorbers based on porous carbon obtained from biomass [20]	0.5	0.7–0.9 ^{***}	4.0	6.0
Absorbers based on carbon hollow microspheres with a designed mesoporous shell [21]	0.4	≥ 0.9	4.8	8.2
Absorbers based on three-dimensional carbon foams obtained from fish skin [22]	0.3	0.5–0.9 ^{***}	8.6	13.6
Absorbers based on nanoporous carbon obtained from walnut shells [23]	0.2	$\sim 0.9^{***}$	1.8	8.9

* d – absorber thickness value.

** f_c – value of the central frequency in the effective absorption band.

*** The values were estimated based on the energy losses of electromagnetic radiation due to its reflection.

In contrast to the analogs [18–23], the proposed absorbers provide the absorption of X-ray electromagnetic radiation energy along with the absorption of microwave electromagnetic radiation energy since their structure includes the composite coating based on barium sulfate and sodium silicate aqueous alkaline solution, which, as shown in [15], is characterized by the X-ray attenuation coefficient values of 2.0–8.7 rel. units (see Table 2). In addition, unlike carbon-containing absorbers [18–23], the proposed absorbers are multiband ones.

Thus, the main results for the experimental verification of the proposed absorbers are as follows.

1. Adding a (0.2 ± 0.05) cm thick layer based on the mixture of powdered barium sulfate and sodium

silicate aqueous alkaline solution to the structure of microwave absorbers based on powdered activated birch charcoal, gypsum and water leads to:

– a decrease by 0.1–0.55 rel. units in the ERAC values in the frequency bands 7.0–10.8 GHz and 14.2–17.0 GHz of the indicated absorbers, which is due to an increase by 2.0–8.0 dB of their ERRC values in the specified frequency bands provided that their ERTC values almost do not change.

– an increase by 0.15–0.22 rel. units of the ERAC values in the frequency band 10.8–14.2 GHz of the indicated absorbers, which is due to a decrease by 1.0–7.0 dB of their ERRC values in the specified frequency band, provided that their ERTC values almost do not change.

2. Adding a (0.2 ± 0.05) cm thick layer based on the mixture of powdered barium sulfate and sodium silicate aqueous alkaline solution to the structure of microwave absorbers based on powdered activated coconut charcoal, gypsum and water leads to:

- a decrease by 0.1–0.4 rel. units of ERAC values in the frequency bands 2.0–3.0 GHz and 7.5–10.2 GHz of the indicated absorbers, which is due to an increase by 1.0–5.0 dB of their ERRC values in the specified frequency bands provided that their ERTC values almost do not change;

- an increase by 0.1–0.55 rel. units of ERAC values in the frequency bands 3.0–7.5 GHz and 15.0–16.5 GHz of the indicated absorbers, which is due to a decrease by 1.0–10.0 dB of their ERRC values in the specified frequency bands provided that their ERTC values almost do not change.

3. Effective absorption bands of the proposed absorbers containing powdered activated birch charcoal are 3.5–7.0 GHz and 10.8–14.2 GHz. Effective absorption bands of the absorbers containing powdered activated coconut charcoal are 5.0–7.5 GHz and 10.2–17.0 GHz. The average values of the ERACs in the effective absorption bands of the first of these absorbers are practically equivalent. The average value of ERAC in the band 5.0–7.5 GHz of the second of these absorbers is higher on 0.2 rel. units than their average value of ERAC in the band 10.2–17.0 GHz.

Based on the presented features, we can conclude that proposed absorbers containing powdered activated birch charcoal are advisable to use in cases where the frequency value of electromagnetic radiation, the energy of which must be attenuated to a greater extent due to its absorption than due to reflection, belongs to the S-band. Proposed absorbers containing powdered activated coconut charcoal are advisable to use in cases where the frequency value of electromagnetic radiation, the energy of which must be attenuated to a greater extent due to its absorption than due to reflection, belongs to the Ku-band.

4. Conclusion

The results of the experimental verification of the proposed absorbers are positive. They are multifunctional multiband ones in the frequency range of 2.0–17.0 GHz. They provide absorption of X-ray electromagnetic radiation along with absorption of electromagnetic radiation energy in the specified frequency range. These absorbers can be

used to cover the walls of premises where X-ray machines are located. At the same time, these absorbers must be fixed in such a way that their layers based on foiled polymer film are adjacent to the premises wall. This will ensure: i) reflection of microwave electromagnetic radiation emitted by external sources (i.e. from sources located outside the specified premises), thus reducing the impact of this radiation on X-ray machines, as well as computer equipment connected to them; ii) absorption of X-ray electromagnetic radiation generated by X-ray machines, thus reducing the impact of this radiation on electronic devices and on people who are outside the specified premises; iii) absorption in a wide frequency band of microwave electromagnetic radiation emitted by computer equipment connected to X-ray machines, thus reducing the level of passive electromagnetic interference in the specified premises.

Based on the presented results, a patent application has been filed for methods for making microwave and X-ray electromagnetic radiation absorbers [24].

5. Funding

This study received no external funding.

6. Acknowledgments

The research was carried out within the framework of the scientific project “Development of Radio-Absorbing Composite Structures Based on Powdered Charcoal-Containing Materials” of the subprogram “Physics of Condensed Matter and the Creation of New Functional Materials and Technologies for Their Production” of the State scientific research program of the Republic of Belarus for 2021–2025 “Materials Science, New Materials and Technologies”.

7. Conflict of interests

The authors declare no conflict of interest.

References

1. Zhan B, Hao Y, Qia X, Qu Y, Ding J, Yang J-l, et al. Multifunctional cellular carbon foams derived from chitosan toward self-cleaning, thermal insulation, and highly efficient microwave absorption properties. *Nano Research*. 2023. DOI:10.1007/s12274-023-6236-7
2. Gu W, Sheng J, Huang Q, Wang G, Chen J, Ji G. Environmentally friendly and multifunctional shaddock

peel-based carbon aerogel for thermal-insulation and microwave absorption. *Nano-Micro Letters*. 2021;13(1). DOI:10.1007/s40820-021-00635-1

3. Yang C, Chen S, Niu S, Xiao L, Qu Y-c. Transparent broadband microwave metamaterial absorber with thermal insulating and soundproof. *Optoelectronic Letters*. 2021;17(2):85-89. DOI:10.1007/s11801-021-0023-8

4. Jiang C, Wang Y, Zhao Z, Ma Z, Liu Y. Multifunctional three-dimensional porous MOFs derived Fe/C/carbon foam for microwave absorption, thermal insulation and infrared stealth. *Ceramics International*. 2023;49(11):18861-18869. DOI:10.1016/j.ceramint.2023.03.008

5. Hong Z, Yu X, Xing Y, Xue M, Luo Y, Yin Z, et al. Tunable head-conducting microwave-absorbing multifunctional composites with excellent microwave absorption, thermal conductivity and mechanical properties. *Journal of Composite Science*. 2023;7(1):15. DOI:10.3390/jcs7010015

6. Fan B, Xing L, Yang K, Zhou F, He Q, Tong G, et al. Synergistically enhanced heat conductivity-microwave absorption capabilities of g-C₃N₄@Fe@C hollow micro-polyhedra via interface and composition modulation. *Chemical Engineering Journal*. 2023;451:138492. DOI:10.1016/j.cej.2022.138492

7. Qu S, Sheng P. Microwave and acoustic absorption metamaterials. *Physical Review Applied*. 2022;17(4):047001. DOI:10.1103/PhysRevApplied.17.047001

8. Wu S, Hou H, Xue X. Quad-band microwave absorbers based on MoO_{3-x}@MWCNT with tunable morphologies for multifunctional multiband absorption. *Carbon*. 2023;201:1160-1173. DOI:10.1016/j.carbon.2022.10.012

9. Sun H, Zhang Y, Wu Y, Zhao Y, Zhou M, Liu L, et al. Broadband absorption of macro pyramid structure based flame retardant absorbers. *Journal of Materials Science & Technology*. 2022;128:228-238. DOI:10.1016/j.jmst.2022.04.030

10. Li D, Hu X, Gao B, Yin W-Y, Chen H, Qian H. Highly transparent tunable microwave perfect absorption for broadband microwave shielding. *Progress in Electromagnetics Research*. 2023;176:35-44. DOI:10.2528/PIER22101901

11. Li X, Zhu L, Kasuga T, Nogi M, Koga H. Frequency-tunable and absorption/transmission-switchable microwave absorber based on a chitin-nanofiber-derived elastic carbon aerogel. *Chemical Engineering Journal*. 2023;469:144010. DOI:10.1016/j.cej.2023.144010

12. Kang S, Qiao S, Cao Y, Hu Z, Li N, Yu J, et al. Multifunctional tubular carbon nanofibers/polyurethane electromagnetic wave absorber with room-temperature self-healing and recyclable performance. *Nano Research*. 2023;16:33-44. DOI:10.1007/s12274-022-4743-2

13. Boiprav OV, Belousova ES, Ahmetdinova ES, Bogush NV. Charcoal-containing building materials for electromagnetic radiation shielding. *Magazine of Civil Engineering*. 2023;117(1):11709. DOI:10.34910/MCE.117.9

14. Boiprav OV, Grinchik NN, Guzov VD, Penialosa Ovalies DI. Study of the influence of the layer thickness of composite coatings based on barium sulphate on the attenuation of X-ray radiation. *Medicinskaya radiologiya i radiacionnaya bezopasnost*. 2022;67(2):69-72. DOI:10.33266/1024-6177-2022-67-2-69-72 (In Russ.)

15. Boiprav O, Ayad H, Abdaljlil SA, Lynkou L, Abdulmawlay M. Charcoal- and foil-containing materials for radio electronic control systems protection from electromagnetic interferences. *Institute of Electrical and Electronics Engineers (IEEE)*. 2023:299-304. DOI:10.1109/STA56120.2022.10019059

16. Shukla V. Review of electromagnetic interference shielding materials fabricated by iron ingredients. *Nanoscale Advances*. 2019;5:1640-1671. DOI:10.1039/c9na00108e

17. Pandey SP. Is it possible that the radiation emitted from electronic devices used in daily life can affect our DNA? *Iconic Research and Engineering Journals*. 2022;6(1):120-125.

18. de Medeiros LI, de Faria Lopes Medeiros NC, Lenz e Silva GFB, de Lima RGA, Amaral-Labat G, et al. Improved microwave absorption performance with sustainable porous carbon/carbon nanotube composites. *Materials Research*. 2022;25. DOI:10.1590/1980-5373-MR-2022-0169

19. Xi J, Zhou E, Liu Y, Gao W, Ying J, Chen Z, et al. Wood-based straightway channel structure for high performance microwave absorption. *Carbon*. 2017;124:492-498. DOI:10.1016/j.carbon.2017.07.088

20. Wu Z, Tian K, Huang T, Hu W, Xie F, Wang J, et al. Hierarchically porous carbons derived from biomasses with excellent microwave absorption performance. *ACS Applied Materials and Interfaces*. 2018;10(13):11108-11115. DOI:10.1021/acsami.7b17264

21. Xu H, Yin X, Zhu M, Han M, Hou Z, Li X, et al. Carbon hollow microspheres with a designable mesoporous shell for high-performance electromagnetic wave absorption. *ACS Applied Materials and Interfaces*. 2017;9(7):6332-6341. DOI:10.1021/acsami.6b15826

22. Zhou X, Jia Z, Feng A, Wang X, Liu J, Zhang M. Synthesis of fish skin-derived 3D carbon foams with broadened bandwidth and excellent electromagnetic wave absorption performance. *Carbon*. 2019;152:827-836. DOI:10.1016/j.carbon.2019.06.080

23. Qiu X, Wang L, Zhu H, Guana Y, Zhang Q. Lightweight and efficient microwave absorbing materials based on walnut shell-derived nanoporous carbon. *Nanoscale*. 2017;9:7408-7418. DOI:10.1039/C7NR02628E

24. Boiprav OV, Grinchik NN. *Methods for manufacturing absorbers of radio wave and X-ray radiation and absorbers of radio wave and X-ray radiation made in accordance with these methods*. Application for invention No. 20220063 (Republic of Belarus). 21 March 2022 (In Russ.)

Information about the authors / Информация об авторах

Olga V. Boiprav, Cand. Sc. (Eng.), Associate Professor, Associate Professor of Information Protection Department, Belarusian State University of Informatics and Radioelectronics (BSUIR), Minsk, Republic of Belarus; ORCID 0000-0002-9987-8109; e-mail: smu@bsuir.by

Vadim A. Bogush, D. Sc. (Phys. and Math.), Professor, Professor of Information Protection Department, BSUIR, Minsk, Republic of Belarus; ORCID 0000-0001-7516-4841; e-mail: bogush@bsuir.by

Nikolay N. Grinchik, D. Sc. (Phys. and Math.), Associate Professor, Leader Researcher, Institute of Heat and Mass Transfer named after A.V. Lykov National Academy of Sciences of Belarus, Minsk, Republic of Belarus; ORCID 0000-0002-1369-4983; e-mail: nngrin@yandex.by

Бойправ Ольга Владимировна, кандидат технических наук, доцент, доцент кафедры защиты информации, Белорусский государственный университет информатики и радиоэлектроники (БГУИР), Минск, Республика Беларусь; ORCID 0000-0002-9987-8109; e-mail: smu@bsuir.by

Богущ Вадим Анатольевич, доктор физико-математических наук, профессор, профессор кафедры защиты информации, БГУИР, Минск, Республика Беларусь; ORCID 0000-0001-7516-4841; e-mail: bogush@bsuir.by

Гринчик Николай Николаевич, доктор физико-математических наук, доцент, ведущий научный сотрудник, Институт тепло- и массообмена имени А. В. Лыкова Национальной академии наук Беларуси, Минск, Республика Беларусь; ORCID 0000-0002-1369-4983; e-mail: nngrin@yandex.by

Received 29 September 2023; Accepted 03 November 2023; Published 15 December 2023



Copyright: © Boiprav OV, Bogush VA, Grinchik NN, 2023. This article is an open access article distributed under the terms and conditions of the Creative Commons Attribution (CC BY) license (<https://creativecommons.org/licenses/by/4.0/>).

AlMg6–AlMg6 weld interface: microstructure and mechanical properties after explosive welding

© Andrey Yu. Malakhov^a, Ivan V. Saikov^a, Igor V. Denisov^a,
Alexander A. Berdychenko^b, Sergey G. Ivanov^b, Nemat N. Niyozbekov^a✉

^a Merzhanov Institute of Structural Macrokinetics and Materials Science RAS (ISMAN),
8, Academician Osipyan St., Chernogolovka, 142432, Russian Federation,
^b Polzunov Altai State Technical University, 46, Lenin Ave., Barnaul, 656038, Russian Federation

✉ nemat199595@mail.ru

Abstract: Due to their low density, high strength, and resistance to corrosion, Al-Mg alloys are widely used in the railcar construction and shipbuilding, and other industries. The aim of this study was to carry out a detailed analysis of the microstructure of the AlMg6–AlMg6 weld interface after explosive welding (EW). The results of this study are important for a better understanding of the joint formation process in EW of AlMg6 with other metals and alloys. The study included optical and electron microscopy of metallographic specimens with etched surfaces. Vickers hardness tests and tear strength tests were carried out to determine the mechanical properties of the joint. Optical and electron microscopy revealed a large number of adiabatic shear bands (ASBs) formed during EW and dark-etching structures formed after etching. An increase in explosive welding parameters leads to an increase in ASBs in the flyer plate and parent plate. The dark-etching structures are most likely the accumulations of structural defects and intermetallic compound fragments. The tear testing of the weld joint showed that higher EW parameters lead to much higher tear strength with a non-uniform distribution along the length of the plates. It was concluded that in order to achieve a joint between AlMg6 and other alloys and metals with the highest strength, plastic deformation in the weld interface must be sufficiently high, while heating must be minimal. The maximum joint strength was 150 MPa in mode 2 and 242 MPa in mode 3, respectively.

Keywords: Al–Mg alloys; explosive welding; weld interface; microstructure.

For citation: Malakhov AYu, Saikov IV, Denisov IV, **Berdychenko AA**, Ivanov SG, Niyozbekov NN. AlMg6–AlMg6 weld interface: microstructure and mechanical properties after explosive welding. *Journal of Advanced Materials and Technologies*. 2023;8(4):304-315. DOI: 10.17277/jamt.2023.04.pp.304-315

Граница соединения АМг6–АМг6: микроструктура и механические свойства после сварки взрывом

© А. Ю. Малахов^a, И. В. Сайков^a, И. В. Денисов^a,
А. А. Бердыченко^b, С. Г. Иванов^b, Н. Н. Нийзбеков^a✉

^a Институт структурной макрокинетики и проблем материаловедения
им. А. Г. Мерджанова РАН, ул. Академика Осипьяна, 8, Черноголовка, 142432, Российская Федерация,
^b Алтайский государственный технический университет им. И.И. Ползунова,
пр. Ленина, 46, Барнаул, 656038, Российская Федерация

✉ nemat199595@mail.ru

Аннотация: Сплавы системы Al–Mg широко используются в судостроении, вагоностроении и других отраслях промышленности благодаря низкой плотности, высокой прочности и коррозионной стойкости. Цель работы – проведение детального исследования микроструктуры границы соединения АМг6–АМг6 после сварки взрывом. Результаты исследования позволили лучше понимать процесс формирования соединений при сварке взрывом сплава АМг6 с другими металлами и сплавами. Металлографические исследования образцов проводили

с помощью оптической и электронной микроскопии. Для исследования механических свойств проведены испытания прочности на отрыв и измерена микротвердость слоев. Оптическая и электронная микроскопия показала, что в процессе сварки взрывом в материалах образуются полосы адиабатического сдвига. Увеличение параметров сварки взрывом приводит к увеличению полос адиабатического сдвига в метаемом и основном слое. Также на границе соединения были обнаружены темнотравящиеся структуры. Предположительно такие структуры представляют собой скопления дефектов и интерметаллических соединений. Установлено, что для получения прочного соединения АМг6 с другими металлами и сплавами необходимо обеспечить пластическую деформацию свариваемых поверхностей при минимальном нагреве зоны соединения. Максимальная прочность соединения составила 150 МПа по режиму 2 и 242 МПа по режиму 3, соответственно.

Ключевые слова: сплав АМг6; сварка взрывом; граница соединения; микроструктура.

Для цитирования: Malakhov AYu, Saikov IV, Denisov IV, Berdychenko AA, Ivanov SG, Niyozbekov NN. AlMg6–AlMg6 weld interface: microstructure and mechanical properties after explosive welding. *Journal of Advanced Materials and Technologies*. 2023;8(4):304-315. DOI: 10.17277/jamt.2023.04.pp.304-315

1. Introduction

The metals and alloys that contribute to reducing the weight of constructions have been in high demand in the aerospace, shipbuilding, automotive and railcar industries. Aluminum alloys are the most commonly used materials for such applications due to their light weight, suitable mechanical properties and corrosion resistance, as well as good weld ability and workability. Wrought non-heat treatable aluminum alloys of the Al–Mg system are currently widely used because of their good corrosion resistance in many acids and seawater, as well as their high tensile strength (up to 420 MPa). These excellent performance properties are due to solid solution strengthening.

It is not always advisable to make constructions entirely of Al–Mg alloys due to their low stiffness and low melting points compared to steel or titanium. Therefore, the elements of a construction that undergo significant mechanical stresses are often made of steel or other alloys. For example, in the shipbuilding industry, the ship hull is made of steel, whereas chimney casings, wheelhouses and deck bridges are made of Al–Mg alloys. This reduces the overall ship weight up to 50–60 %, thus increasing the deadweight tonnage and improving the overall ship performance [1, 2]. In particular, the hovercraft hulls are made entirely of Al–Mg alloys. In the automotive industry, Al–Mg alloys are used in manufacturing various parts of suspension, transmissions, etc. [3]. This reduces the automobile's weight and fuel consumption and minimizes CO₂ emissions [4]. In addition, Al–Mg alloys are used in the production of cryogenic equipment used in the transportation of liquefied gases [5].

Nowadays, various fusion welding methods are used for joining Al–Mg alloys to steel work pieces [6].

Pressure welding produces stronger joints between Al–Mg alloys and steels compared to fusion

welding. This is due to the fact that the joint is formed in the solid phase, which significantly reduces the number of brittle Fe_xAl_y IMCs at the weld interface. The joint between Al–Mg alloy and steel can be made by friction welding [7, 8], diffusion welding [9], ultrasonic welding [10], cold rolling [11], magnetic-pulse welding [12], hot isostatic pressing [13], and explosive welding (EW) [14–16].

All those studies have shown that the welding of aluminum alloys with steels poses a number of challenges. These challenges are associated with brittle Fe_xAl_y IMCs, the differences in the melting points of the two metals, their physical properties and thermal expansion coefficients. Therefore, bimetallic transition joints (BTJ) are used to meet these challenges [17]. Consequently, the properties of the BTJs used in the process of welding will define a construction's overall performance properties.

Nowadays, EW is a promising technique for the BTJs manufacturing [17, 18]. For example, G. Costanza et al. welded a BTJ consisting of 5086 aluminum alloy and A516 steel with an intermediate layer of pure aluminum [19]. A new method of EW of 5083 aluminum alloy with Q345 steel was studied in [20], where dovetail grooves were employed. The tensile shear strength of 5083/Q345 clad plate was 167.6 MPa, that is higher than that of 5083 aluminum alloy. However, the dovetail grooves trapped the compressed gas in the gap between the base and flyer plates, which led to the formation of pores in the weld interface.

Microstructure and morphology of the weld interface are important characteristics in EW studies. The weld interface morphology is divided into wavy interface [21] and straight interface [22, 23]. The weld interface microstructure can vary significantly in depth due to the non-uniform heat distribution, namely, the heat does not have time to dissipate from locally heated zones, which are formed

Table 1. Mechanical properties and chemical composition of commercial AlMg6 alloy under EN 10204 3.2 certificate

Tensile strength, MPa		Yield strength, MPa		Elongation, %		Density, kg·m ⁻³					
353-356		193-221		16.6–19.3		2640					
Composition, wt. %											
Al		Mg		Mn		Zn		Fe		others	
92.73		5.80–5.87		0.86		0.18		0.16		0.20	

due to highly intensive deformation of the weld interface. Also, this deformation causes very high grain refinement near the weld interface [24], thus the process of structure fragmentation takes place [25]. The structure fragmentation was studied in detail in [26]. In addition, numerous deformation twins, dislocations and adiabatic shear bands (ASBs) near the weld interface were observed in many studies [27–29]. EW of dissimilar metals produces brittle IMCs and solid solutions at the weld interface [30], which, in most cases, significantly reduce the strength of the welded joint [31].

The main objective in the BTJ production is to achieve the tensile strength comparable to that of AlMg6. Obtaining a strong joint between steel and pure aluminum does not pose many difficulties. On the other hand, the strong joint between steel and Al–Mg alloys cannot be achieved if the magnesium content is greater than 5 % [32, 33]. As is known, magnesium is the main factor that defines the mechanical properties of AlMg6 [34].

Resolving these issues requires detailed study of the structure of the weld interface in the AlMg6 bimetal. Such a scheme excludes the formation of Fe_xAl_y IMCs, thus allowing to determine the effects of magnesium on the weld interface formation. This scheme of joining similar metals was applied in [35] where the EW of Al to Al was performed.

This study examined the EW of AlMg6 with AlMg6. It presented the results of the microstructural study of the AlMg6–AlMg6 weld interface after EW and the results of the mechanical testing of the joint. These results will be used in further studies to determine the parameters of the EW of AlMg6 alloy with steels.

2. Materials and Methods

2.1. Initial materials

The initial materials used in this study were 4-mm-thick plates of AlMg6 alloy, whose composition and properties are listed in Table 1.

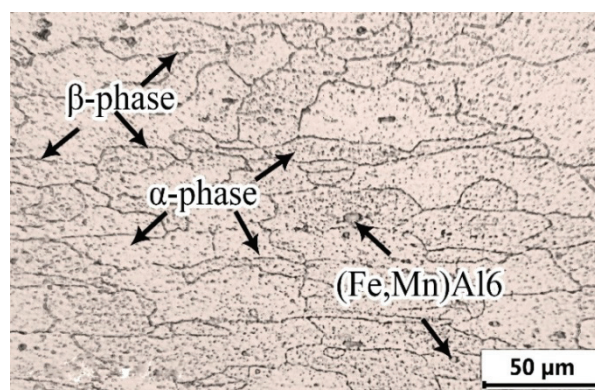
**Fig. 1.** The initial microstructure of the AlMg6

Figure 1 shows the microstructure of the initial AlMg6 plate. The grains of α -solid solution (α -phase) are elongated along the rolling direction. Small (Fe, Mn)Al₆ inclusions are inside the grains, whereas β -phase (Mg₂Al₃) is along the grain boundaries [36].

2.2. Explosive welding

The EW experiments were conducted in the parallel plate configuration shown in Fig. 2a. Before assembling, the surfaces of the plates were cleaned from oxide films and rust. The explosive used was a 96 : 4 mixture of microporous ammonium nitrate and diesel oil ($d = 780 \text{ kg·m}^{-3}$). The top surface of the flyer plate was covered with a protective polythene layer. The layer of the explosive was spread over the configuration, placed in a formwork (Fig. 2b), and exploded with a detonator.

The EW parameters were calculated from the equations taken from [37]. The equation for the flyer plate velocity is given as follows:

$$V_0 = 1.2D \frac{\sqrt{1 + \frac{32}{27}r - 1}}{\sqrt{1 + \frac{32}{27}r + 1}}, \quad (1)$$

where D is the detonation velocity, m·s^{-1} ; r is the ratio of the explosive mass to the flyer plate mass:

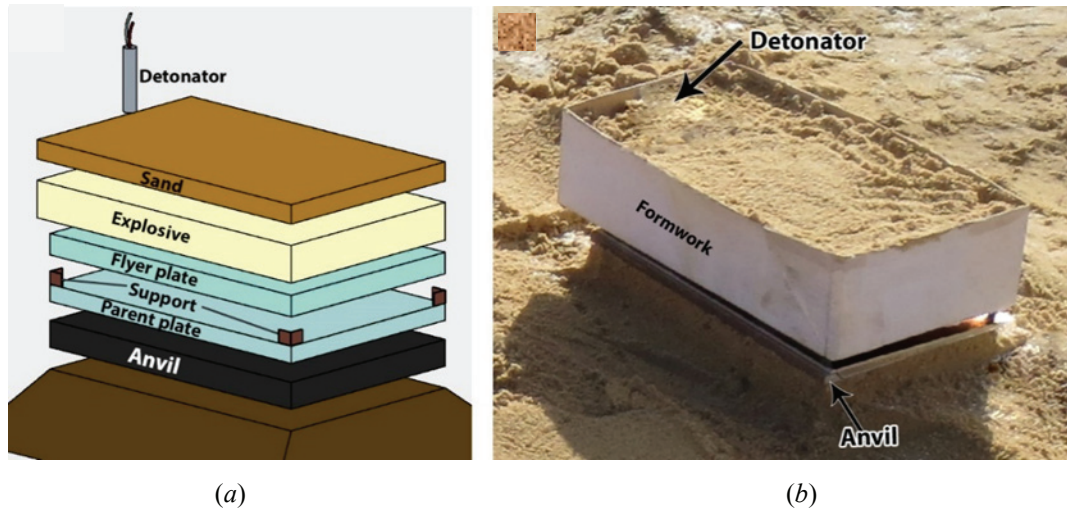


Fig. 2. Configuration of the experiment (a) and actual view of the experiment (b)

$$r = \frac{m_e}{m_{pl}}, \quad (2)$$

where m_e is the explosive mass, kg; m_{pl} is the flyer plate mass, kg.

The collision angle was calculated from the following equation:

$$\gamma = 2 \arcsin \left(\frac{V_0}{2D} \right). \quad (3)$$

2.3. Microstructural study

The tear strength specimens and metallographic specimens were prepared according to Fig. 3.

The specimens with approximate dimensions of $30 \times 30 \times 8$ mm were cut from zone B, the specimens with approximate dimensions of $10 \times 20 \times 8$ mm – from zones A.

The metallographic specimens were embedded into a BAKELIT GF conductive compound with graphite filler using a METAPRESS-P metallographic

press. Grinding and polishing were performed using a DIGIPREP machine. Grinding was carried out using emery papers of grit sizes 320, 800, 1500 and 2500. Polishing was carried out using two water-based suspensions. One suspension contained $3 \mu\text{m}$ diamond particles, while the other contained $1 \mu\text{m}$ diamond particles. Super finishing was carried out in an acid suspension of colloidal silicon oxide with a particle size of $0.05 \mu\text{m}$. The identification of microstructural elements was performed by successive etching with Keller's reagent for 5–15 s and then with Vek's reagent for 60 s [38–40].

The metallographic studies were performed with a Carl Zeiss Axio Observer Z1m inverted metallographic microscope using a Thixomet Pro software package according to the procedure given in [41–44]. The SEM/EDS analysis was carried out with a Zeiss Ultraplus microscope equipped with an INCA 350 Oxford accessory.

2.4. Mechanical testing

The microhardness (HV) was measured using a PMT-3 Vickers hardness tester and MMS software. Loads of 50 g were applied for 10 s. Figure 4 shows a microhardness measurement diagram.

The tear testing of the weld joint after EW was conducted on an Instron 1195 universal testing machine as shown in Fig. 5.

Then tear strength σ_t was calculated from the following equation:

$$\sigma_t = \frac{4P}{\rho(d_2^2 - d_1^2)}, \quad (4)$$

where P is the applied load, N; d_1 is the inner diameter, mm; d_2 is the outer diameter, mm.

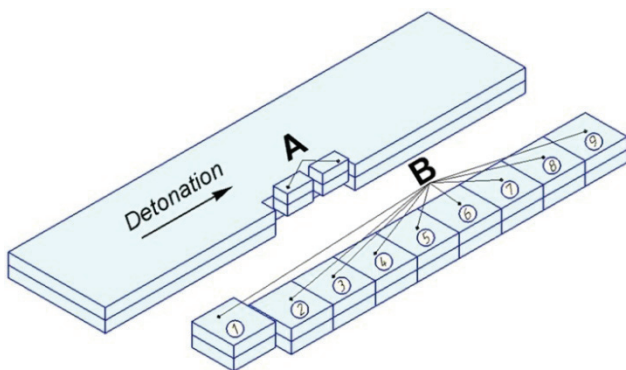


Fig. 3. Specimens for metallographic studies:
A – specimens for metallographic study;
B – specimens for tear strength study

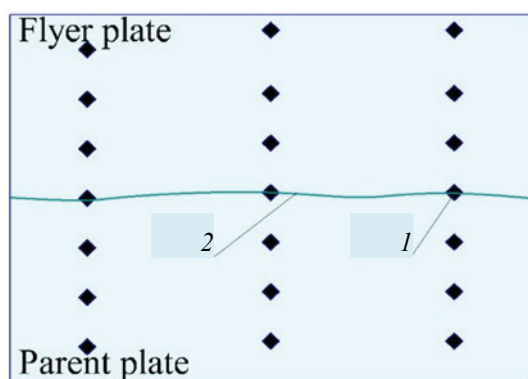


Fig. 4. Microhardness measurement diagram:
1 – indentation; 2 – weld interface

3. Results and Discussion

3.1. Preliminary microstructural analysis

The calculated parameters for three different EW modes and the detonation velocities (D) are listed in Table 2.

The mode 1 parameters did not produce a joint due to the insufficient plastic deformation of the surfaces and the insufficient pressure of the detonation products on the surface of the flyer plate.

Figure 6 shows the microstructure of the weld interface after etching for modes 2, 3. The weld interface produced by mode 2 (specimen 2) is in the shape of a nearly straight line (Fig. 6a), and the weld produced by mode 3 (specimen 3) is in the shape of a wave (Fig. 6b). Dark-etching structures were found along the weld interface (Figs. 6c and 6d). Supposedly, these structures are the accumulations of significantly deformed structures, which indicates the

Table 2. EW parameters

Mode	r	D , m·s ⁻¹	V_0 , m·s ⁻¹	γ , °
1	1.5	2000	600	17.2
2	2.6	2700	1100	23.6
3	3.7	3200	1535	27.8

presence of dislocations. The width of the dark-etching structures is 3–4 μm (Fig. 6c and 6e) in specimen 2 and 7–9 μm (Figs. 6d and 6f) in specimen 3.

Specimen 2 and especially specimen 3 show the presence of ASBs, which branch off from the weld interface into the material in both directions as shown by blue arrows in Figs. 6a and 6b. The ASBs are narrow regions of intense shear and plastic instability. They appear in materials after severe deformation.

In specimen 3, the number of ASBs increases due to higher impact velocity and higher deformation. In all the specimens, the angles between the ASBs and the weld interfaces are about 30°.

3.2. EDS measurements

A detailed EDS analysis of the specimens before etching (points 6, 7 in specimens 2 in Fig. 7a and points 3–5 in specimens 3 in Fig. 7b) revealed structures with high Mg content (20.9–47.9 %), indicating the presence of β -phase in these structures. The Mg content in the α -phase is about 7 % (points 1, 2 in specimen 2 in Fig. 7a and points 6 and 7 in Fig. 7b). Also, numerous (Fe, Mn)Al₆ inclusions (points 3 and 5 in Fig. 7a and points 1 and 2 in Fig. 7b) were observed.

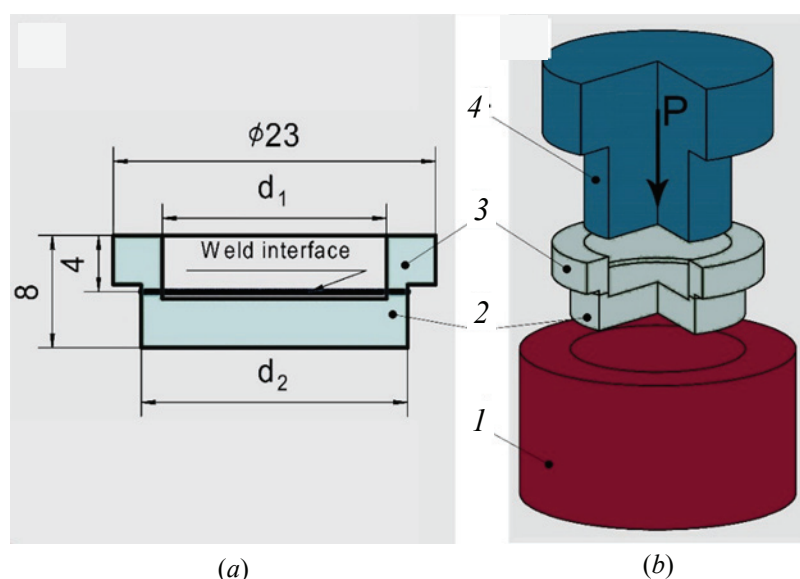


Fig. 5. Tear specimen (a) and tear testing diagram (b): 1 – mold; 2 – base layer; 3 – flyer layer; 4 – male die

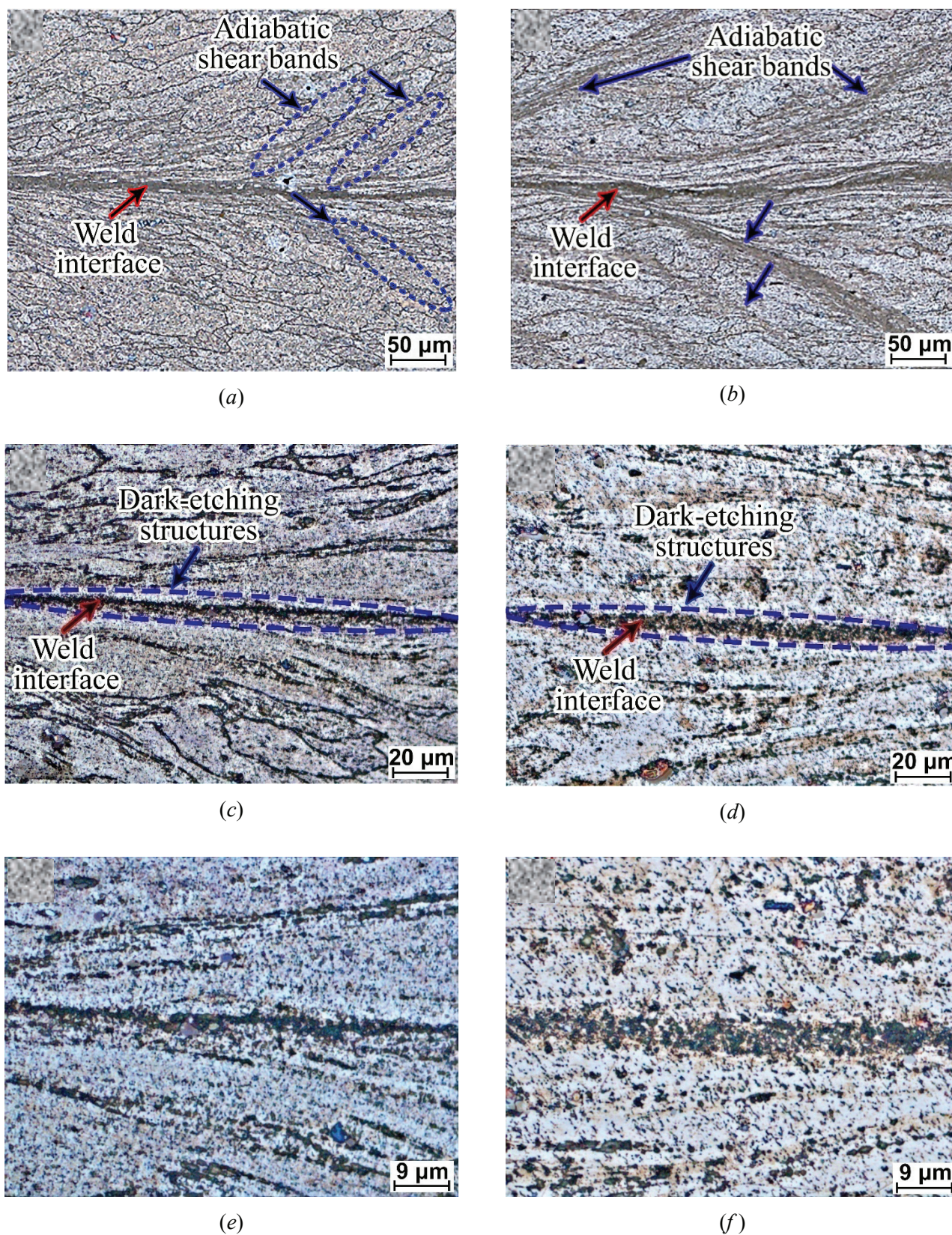
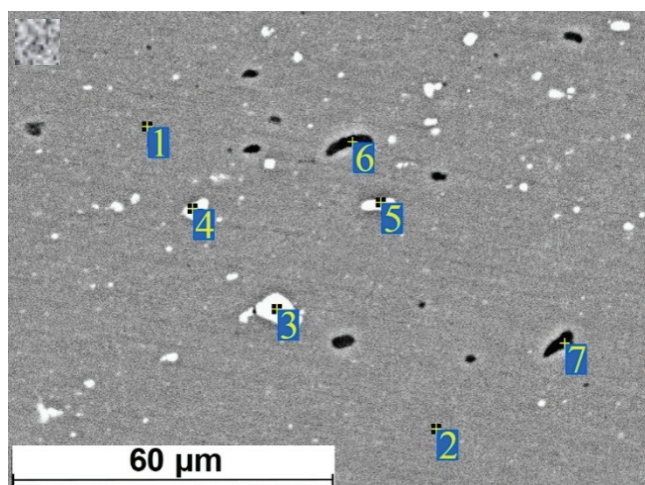
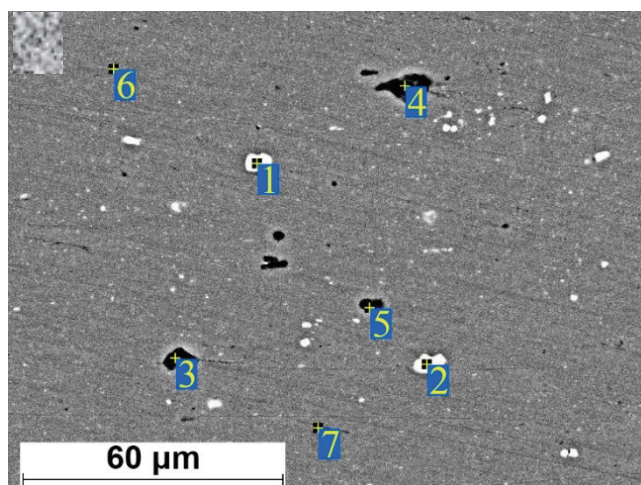


Fig. 6. Microstructure of the weld interface: specimen 2 (*a, c, e*) and specimen 3 (*b, d, f*)



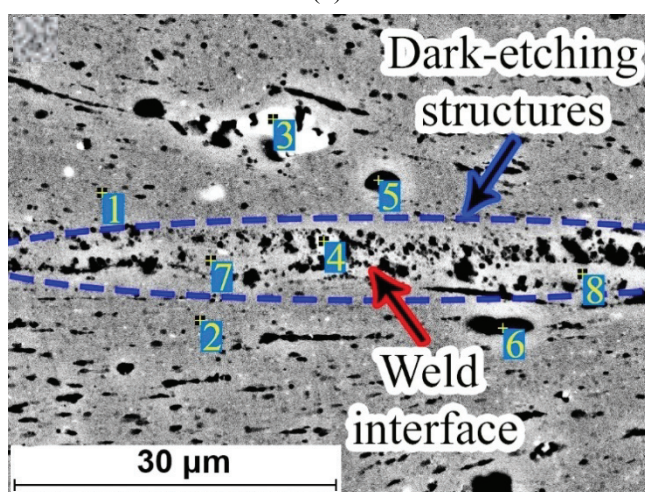
No.	O	Mg	Si	Mn	Fe	Al
Element content, at. %						
1	1.3	6.9	—	0.3	—	Balance
2	1.5	6.8	—	0.3	—	
3	1.5	0.6	1.7	6.8	7.8	
4	1.2	2.7	0.6	7.4	4.1	
5	2.1	2.2	2.7	5.6	7.5	
6	19.8	20.9	13.8	0.1	0.1	
7	28.6	32.4	18.3	—	0.1	

(a)



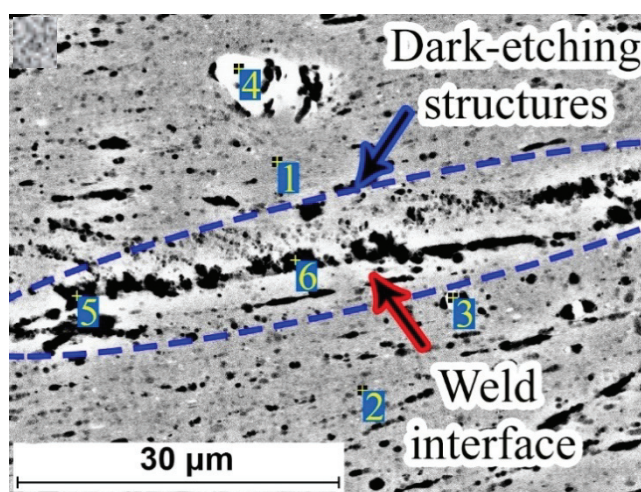
No.	O	Mg	Si	Mn	Fe	Al
Element content, at. %						
1	1.5	1.0	2.8	6.7	8.4	Balance
2	0.9	0.6	3.3	7.6	8.9	
3	24.0	15.9	15.1	0.1	0.1	
4	23.1	47.9	21.2	0.1	0.1	
5	24.7	35.1	17.1	—	—	
6	1.3	6.9	—	0.3	—	
7	0.8	6.9	—	0.3	—	

(b)



No.	O	Mg	Si	Mn	Fe	Al
Element content, at. %						
1	1.2	6.7	—	0.3	—	Balance
2	1.2	6.6	—	0.3	—	
3	1.3	2.0	0.8	4.4	6.9	
4	3.3	4.1	0.2	3.7	4.1	
5	0.4	7.1	0.1	0.5	0.1	
6	35.5	3.0	10.7	0.1	—	
7	1.0	6.7	0.1	0.4	—	
8	1.4	6.7	—	0.2	—	

(c)



No.	O	Mg	Si	Mn	Fe	Al
Element content, at. %						
1	1.2	6.5	—	0.3	—	Balance
2	1.3	6.6	—	0.2	—	
3	1.1	5.0	—	2.5	2.5	
4	1.4	1.3	2.6	6.3	7.7	
5	3.8	6.6	0.7	0.4	—	
6	4.2	6.6	0.1	0.3	—	

(d)

Fig. 7. SEM images of weld interface and the results of point EDS analysis: specimen 2 (a, c) and specimen 3 (b, d)

Figure 8 shows the points of microhardness distribution along the thickness of the specimens according to the diagram shown in Fig. 3. The dashed lines show the microhardness of the initial plate of AlMg6. The blue points indicate the microhardness of AlMg6–AlMg6 bimetal after EW. Both specimens exhibit a sharp decrease in microhardness at the weld interface. In some points, the microhardness is lower than in the initial plate. This decrease suggests that a dynamic recrystallization of the grains and an ageing of AlMg6 occurred due to extreme heating followed by rapid cooling of the weld interface. The sources of the heat are shock-compressed gas in the gap and severe plastic deformation of the surfaces during the collision. The recrystallization decreases the

dislocation density and therefore reduces the strength of the material [34].

After EW, the microhardness near the weld interface was approximately 200 HV, which was 20 % higher than that of the initial plate. This higher microhardness was due to work hardening in the initial plate. The width of the work-hardened zone was approximately 5 mm in specimen 1 and 2 mm in specimen 2.

The average tear strength in specimen 2 was (80 ± 10) MPa, and in specimen 3 it was (230 ± 10) MPa. The mechanical testing revealed three distinct zones of tear strength values. The first zone (Fig. 9) in specimens 2 and 3 had low tear strength (≤ 76 MPa). This is due to the fact that it takes some

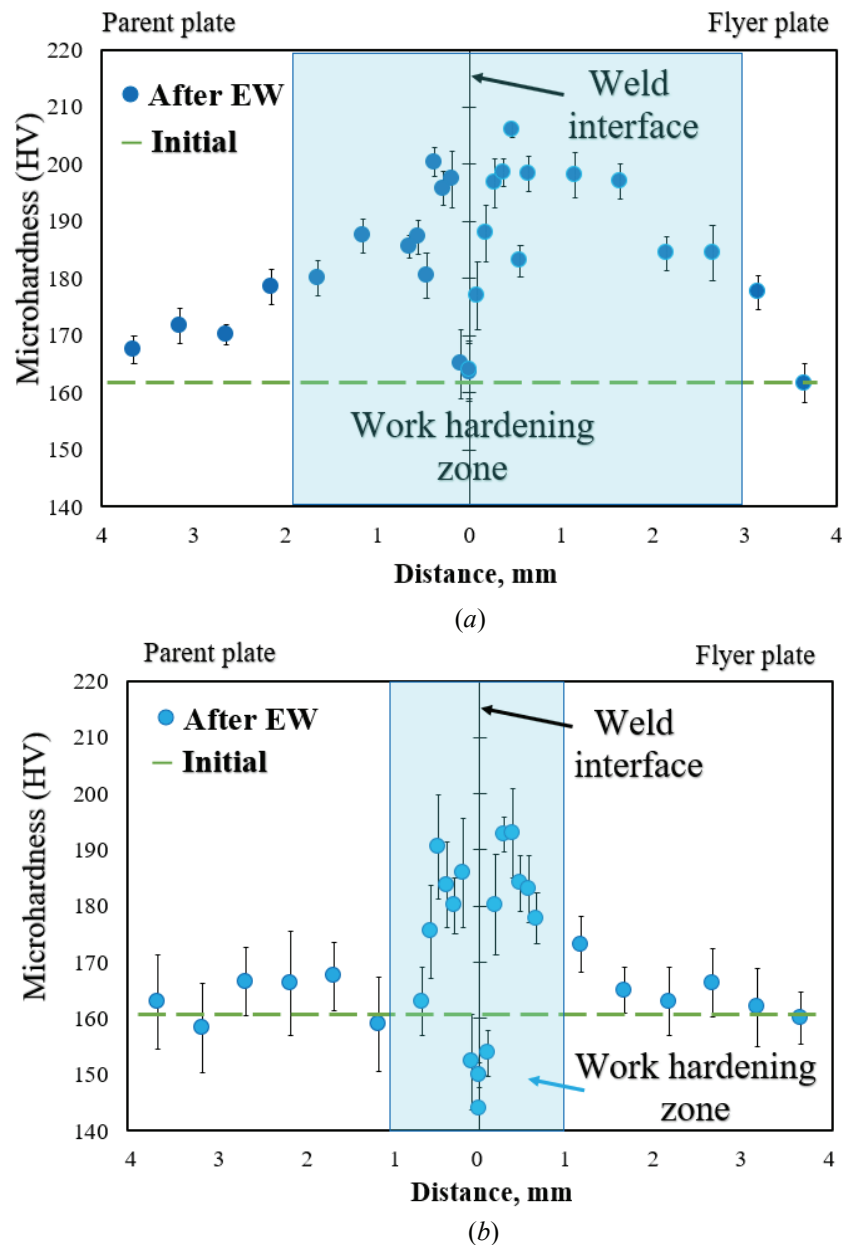


Fig. 8. Microhardness distribution in specimen 2 (a) and specimen 3 (b)

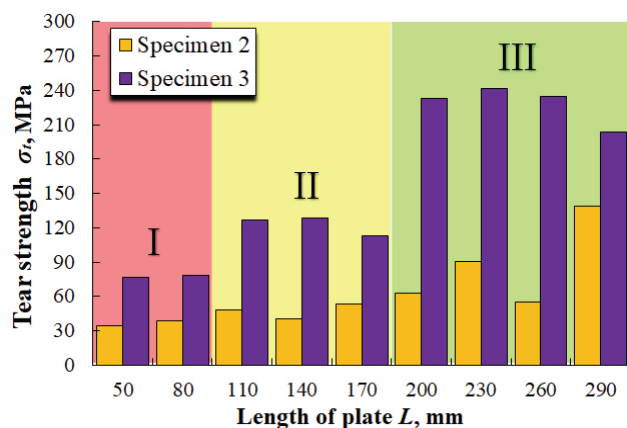


Fig. 9. The tear strength values distribution along the bimetal plates

time for the pressure to achieve the values that are necessary to form a strong joint. It is generally known that the high pressure and temperature in the welding gap provide removing both the oxide films and contaminants from the welded surfaces that make it possible for the atoms of two materials to meet at interatomic distance. Also, the pressure must be higher than the dynamic elastic limit of the materials for the deformation of the weld interface. At the beginning of the explosive welding process (it corresponds to the first zone) the pressure and temperature were not enough that to cleaning and deform the welded surfaces. The second zone shows a uniform tear strength distribution (113–128 MPa). The third zone had the highest tear strength values (204–242 MPa) and the average tear strength in this zone was 228 MPa, which was 35 % lower than the ultimate tensile strength of the initial AlMg6 plate.

As was noted earlier, welding a high-quality joint between Al–Mg alloys and stainless-steel using EW poses certain difficulties, which are caused by the formation of brittle intermetallic compounds at the weld interface and by β -phase (Mg_2Al_3) along the boundaries of α -phase [36]. In Al–Mg alloys, Mg provokes the formation of ASBs during deformation, which are zones of stress concentrations. ASBs then can transform into microcracks, which substantially reduces the strength of the material and its corrosion resistance. It should also be noted that with higher Mg content, ASBs form under lower deformations. In our previous studies [32], the EW joints between AlMg6 and 08Cr18Ni10Ti had the average tear strength of 120 MPa at most, which is not sufficient for the use as BTJs.

At present, much research has been focused on the use of friction stir welding (FSW) for obtaining BTJs, although this method has sample size restrictions [7]. EW does not have sample size restrictions; however, its pulse character of loading

substantially deforms the grains in the material and changes the structure of the weld interface.

In this study, EW experiments were carried out to study the evolution of the deformed microstructure of the weld interface as well as to detect the possible presence of diffusion of Mg from α -phase and δ -phase towards the weld interface. The possibility of diffusion of particles (atoms, impurity elements, etc.) under dynamic loading was explored in [45]. Moreover, EW of similar materials prevents forming IMCs and minimizes residual stresses at the weld interface.

The EW experiments with the parameter $r = 1.5$ (specimen 1) did not result in an AlMg6–AlMg6 joint. This is probably due to the fact that a substantial amount of the explosive charge got scattered in the EW process thus reducing the pressure of the detonation products. This reduced pressure in its turn reduces the plastic deformation in the weld interface. The refractory oxide film on the AlMg6 surface also reduces the amount of plastic deformation. On the other hand, the parameters $r = 2.6$ (specimen 2) and $r = 3.7$ (specimen 3) produced an AlMg6–AlMg6 joint. The study of the microstructure of the weld interface shows that specimen 2 has a weld interface in the shape of an almost straight line (Fig. 6a), whereas specimen 3 has a weld interface in the shape of a wave. This wavy profile is due to higher EW parameters and as a result, stronger deformation of the weld interface in specimen 3. Chemical etching revealed dark-etching structures both in the weld interface and in the ASBs. The formation of ASBs is characteristic of Al–Mg alloys and with increasing Mg content their number usually increases.

Apparently, the dark-etching structures in the weld interface are accumulations of ultrafine IMCs. These IMCs before welding were along the grain boundaries, but the collision of the plates during the process of EW welding resulted in their accumulation in the weld interface. The etching revealed hollow surfaces of the dark-etching structures (Figs. 7c and 7d). These pits formed due to a higher solubility of nonmetallic inclusions in the etchant in areas with local accumulations of dislocations and the pitting of the surfaces of the specimens during grinding, which crushes the IMCs and dislodges them from the specimen surfaces.

Presumably, the plastic deformation caused by the EW process crushes the IMCs and move the fragments to the weld interface and to the zone adjacent to it. Notably, the highest concentration of the fragments is in the weld interface and it gradually decreasing further away from it.

The tear strength distribution along the bimetal plate (Fig. 9) shows that the average tear strength is not sufficiently high in specimen 2, thus mode 2 is not suitable for producing bimetals with an AlMg6 layer. On the other hand, the average tear strength is higher by 60 % in specimen 3, although its distribution along its length is not uniform.

4. Conclusion

Optical and electron microscopy have revealed the presence of a large number of ASBs and dark-etching structures formed during EW. The number of the ASBs and dark-etching structures is roughly the same in both layers. The ASBs formed in the zones of maximum compressive stresses; the dark-etching structures are probably the accumulations of structural defects and IMC fragments. Tear testing of the weld joint has shown that higher EW parameters lead to much higher tear strength with a non-uniform distribution along the plate, which is attributed to the non-uniform impact of gaseous detonation products and the thermodynamic parameters of the shock-compressed gas. In order to achieve a joint between AlMg6 and various other alloys and metals with the highest strength possible, plastic deformation in the weld interface must be sufficiently high while the heating must be minimal. Based on the results of this study, optimal EW parameters could be developed in further studies to achieve a joint between AlMg6 and 08Cr18Ni10Ti steel with the strength close to that of AlMg6.

5. Funding

This study received no external funding.

6. Acknowledgements

This research was funded in accordance with the state task of Merzhanov Institute of Structural Macrokinetics and Materials Science of Russian Academy of Sciences (ISMAN). This research was performed using the set of modern scientific instruments available for multiple access at ISMAN Center of Shared Services. This research was performed using the set of modern scientific instruments available for multiple access at Polzunov Altai State Technical University Center of Shared Services.

7. Conflict of interests

The authors declare no conflict of interest.

References

1. Wahid MA, Siddiquee AN, Khan ZA. Aluminum alloys in marine construction: characteristics, application, and problems from a fabrication viewpoint. *Marine Systems & Ocean Technology*. 2020;(15):70-80. DOI:10.1007/s40868-019-00069-w
2. Hosseinabadi OF, Khedmati MR. A review on ultimate strength of aluminium structural elements and systems for marine applications. *Ocean Engineering*. 2021;(232):109153. DOI:10.1016/j.oceaneng.2021.109153
3. Hirsch J. Aluminium in innovative light-weight car design. *Materials Transactions*. 2011;(52):818-824. DOI:10.2320/matertrans.L-MZ201132
4. Del Pero F, Delogu M, Berzi L, Dattilo CA, Zonfrillo G, Pierini M. Sustainability assessment for different design solutions within the automotive field. *Procedia Structural Integrity*. 2019;(24):906-925. DOI:10.1016/j.prostr.2020.02.080
5. Senkov ON, Bhat RB, Senkova SV. High strength aluminum alloys for cryogenic applications. *Metallic Materials with High Structural Efficiency*. 2004;146:151-162. DOI:10.1007/1-4020-2112-7_15
6. Atabaki MM, Nikodinovski M, Chenier P, Ma J, Harooni M, Kovacevic R. Welding of aluminum alloys to steels: An overview. *Journal for Manufacturing Science and Production*. 2014;14(2):59-78. DOI:10.1515/jmsp-2014-0007
7. Ahmed MMZ, Jouini N, Alzahrani B, El-Sayed Seleman MMES, Jhaheen M. Dissimilar friction stir welding of AA2024 and AISI 1018: Microstructure and mechanical properties. *Metals*. 2021;(11):330. DOI:10.3390/met11020330
8. Vincze G, Simões F, Butuc M. Asymmetrical rolling of aluminum alloys and steels: A review. *Metals*. 2020;(10):1126. DOI:10.3390/met10091126
9. Shi H, Qiu R, Tu Y, Yu H, Yin D. Study on the joining characteristics of diffusion welding lap joint with various temperatures between aluminum alloy and stainless steel. *Advanced Materials Research*. 2011;291-294:1003-1006. DOI:10.4028/www.scientific.net/AMR.291-294.1003
10. Zhang C, Li H, Liu Q, Huang C, Zhou K. Ultrasonic welding of aluminum to steel: A review. *Metals*. 2023;13:29. DOI:10.3390/met13010029
11. Poddar VS, Rathod MJ. Evaluation of mechanical properties of cold roll bonded mild steel and aluminum. *Materials Today Proceedings*. 2021;43:3014-3022. DOI:10.1016/j.matpr.2021.01.363
12. Yu H, Tong Y. Magnetic pulse welding of aluminum to steel using uniform pressure electromagnetic actuator. *The International Journal of Advanced Manufacturing Technology*. 2017;91(5-8):2257-2265. DOI:10.1007/s00170-016-9928-y
13. Makhina DN, Nikulin SA, Denisov VN, Klyatskin AS. Effect of the production conditions on the structure and strength of the AlMg6 Alloy – 12Kh18N10T steel bimetallic joint. *Russian Metallurgy (Metally)*. 2020;(10):1095-1101. DOI:10.1134/S003602952010016X

14. Palaci Y, Olgun M. Influences of heat treatment on mechanical behavior and microstructure of the explosively welded grade steel / EN AW 5083 aluminium joint. *Archives of Metallurgy and Materials*. 2021;66(2):373-380. DOI:10.24425/amm.2021.135868
15. Carvalho GHSFL, Galvão I, Mendes R, Leal RM, Loureiro A. Explosive welding of aluminium to stainless steel using carbon steel and niobium interlayers. *Journal of Materials Processing Technology*. 2020;283:116707. DOI:10.1016/j.jmatprotec.2020.116707
16. Wang J, Zhang Y. A study on weldability of aluminum alloy-aluminum-steel transition joints. *Advanced Materials Research*. 2013;631-632:713-716. DOI:10.4028/www.scientific.net/AMR.631-632.713
17. Boroński D, Skibicki A, Maćkowiak P, Płaczek D. Modeling and analysis of thin-walled Al/steel explosion welded transition joints for shipbuilding applications. *Marine Structures*. 2020;74:102843. DOI:10.1016/j.marstruc.2020.102843
18. Matteis P, Gullino A, D'Aiuto F, Puro CM, Scavino G. Welding between aluminum alloy and steel sheets by using transition joints. *Journal of Materials Engineering and Performance*. 2020;29:4840-4853. DOI:10.1007/s11665-020-04595-2
19. Costanza G, Crupi V, Guglielmino E, Sill A, Tata ME. Metallurgical characterization of an explosion welded aluminum/steel joint. *Metallurgia Italiana*. 2016;108(11):17-22.
20. Li X, Ma H, Shen Z. Research on explosive welding of aluminum alloy to steel with dovetail grooves. *Materials & Design*. 2015;87:815-824. DOI:10.1016/j.matdes.2015.08.085
21. Wang J, Li X-Jie, Yan H-Hao, Wang X-Hong, Wang Y-Xin. Research on titanium-copper explosive welding interface with different welding parameters. *International Journal of Advanced Manufacturing Technology*. 2022;122(9-10):3595-3606. DOI:10.1007/s00170-022-10102-9
22. Raj P, Ramya DG, Manoj Kumar VK, Sukesh OP. Tensile and shear strength evaluation in joining dissimilar plates of mild steel with aluminum alloy through explosive cladding approach. *Materials Today*. 2023;80:2753-2759. DOI:10.1016/j.matpr.2021.07.032
23. Chen X, Inao D, Tanaka S, Mori A, Li X, Hokamoto K. Explosive welding of Al alloys and high strength duplex stainless steel by controlling energetic conditions. *Journal of Manufacturing Processes*. 2020;58:1318-1333. DOI:10.1016/j.jmapro.2020.09.037
24. Kwiecien M, Kopyscianski M, Bloniarz R, Muszka K, Majta J. Influence of deformation conditions on the in homogeneity of plastic flow of structurally graded bimetal systems. *Procedia Manufacturing*. 2018;15:1649-1655. DOI:10.1016/j.promfg.2018.07.272
25. Grinberg BA, Ivanov MA, Rybin VV, Elkina OA, Patselov AM, Antonova OV, Inozemtsev AV, Tolmachev TP. Fragmentation processes during explosion welding (review). *Russian Metallurgy (Metally)*. 2013;727-737. DOI:10.1134/S0036029513100030
26. Greenberg BA, Ivanov MA, Kuzmin SV, Lysak VI. *Explosive welding: Processes and structures*. 1st ed. Boca Raton: CRC Press; 2019. 242 p. DOI:10.1201/9780429340550
27. Rouzbeh A, Sedighi M, Hashemi R. Comparison between explosive welding and roll-bonding processes of AA1050/Mg AZ31B bilayer composite sheets considering microstructure and mechanical properties. *Journal of Materials Engineering and Performance*. 2020;29:6322-6332. DOI:10.1007/s11665-020-05126-9
28. Fang Z, Shi C, Shi H, Sun Z. Influence of explosive ratio on morphological and structural properties of Ti/Al clads. *Metals*. 2019;9:119. DOI:10.3390/met9020119
29. Zerui S, Changgen S, Zhonghang F, Hang S. A dynamic study of effect of multiple parameters on interface characteristic in double-vertical explosive welding. *Materials Research Express*. 2020;7:016541. DOI:10.1088/2053-1591/ab6538
30. Bugajska M, Maj L, Jarzebska A, Terlicka S, Faryna M, Szulc Z, Wojewoda-Budka J. Variety of aluminum/steel interface microstructures formed in explosively welded clads followed by the weld's thermal expansion response. *Journal of Materials Engineering and Performance*. 2022;31:7088-7097. DOI:10.1007/s11665-022-07027-5
31. Sherpa BB, Kumar PD, Upadhyay A, Kumar A, Agarwal A, Tyagi S. Effect of explosive welding parameters on Al/LCS interface clad by low velocity of detonation explosive welding (LVEW) process. *International Journal of Advanced Manufacturing Technology*. 2021;113(11-12):3303-3317. DOI:10.1007/s00170-021-06800-5
32. Malakhov AY, Saikov IV, Denisov IV, Niyezbekov NN. AlMg6 to titanium and AlMg6 to stainless steel weld interface properties after explosive welding. *Metals*. 2020;(10):1500. DOI:10.3390/met10111500
33. Trikov YP, Gurevich VG, Shmorgunov VG. *Layered composites based on aluminum and its alloys*. Moscow: Metallurgizdat; 2004. 230 p. (In Russ.)
34. Ambroziak A, Korzeniowski M, Kustron P, Winnicki M, Sokołowski P, Harapinska E. Friction welding of aluminium and aluminium alloys with steel. *Advances in Materials Science and Engineering*. 2014;1-15. DOI:10.1155/2014/981653
35. Grignon F, Benson D, Vecchio KS, Meyers MA. Explosive welding of aluminum to aluminum: analysis, computations and experiments. *International Journal of Impact Engineering*. 2004;30:1333-1351. DOI:10.1016/j.ijimpeng.2003.09.049
36. Ren L, Gu H, Wang W, Wang S, Li C et al. Effect of mg content on microstructure and properties of Al-Mg alloy produced by the wire arc additive manufacturing method. *Materials*. 2019;(12):4160. DOI:10.3390/ma12244160
37. Saikov IV, Malakhov AY, Saikova GR, Denisov IV, Gulyaev PYu. Influence of explosive welding parameters on the structure of interface in brass-invar thermobimetal. *Inorganic Materials: Applied Research*. 2020;(11):448-452. DOI:10.1134/S2075113320020331
38. George F, Vander V. *ASM Handbook: Metallography and Microstructures*. 9th ed. United States: ASM International; 2004. 1184 p.

39. Thomas J, Bruno Dehua Y, Mueller E, George F, Vander V, Jeffrey AJ, Magdefrau N, Deacon R. *Materials characterization*. 10nd ed. United States: ASM International; 2019. 800 p.

40. Berdychenko AA, Guryev AM, Ivanov SG, Guryev MA, Sitnikov AA. Morphology of layered metal composites, obtained in various ways. *Fundamental'nyye problemy sovremennogo materialovedeniya*. 2021;2:216-223. (In Russ.)

41. Kazakov AA, Ryaboshuk SV, Lyubochko DA, Chigintsev LS. Research on the origin of nonmetallic inclusions in high-strength low-alloy steel using automated feature analysis. *Microscopy and Microanalysis*. 2015;(21):1755-1756. DOI: 10.1017/S1431927615009551

42. Vander Voort GF, Pakhomova O, Kazakov A. Evaluation of normal versus non-normal grain size

distributions. *Materials Performance and Characterization*. 2016;5(5). DOI:10.1520/MPC20160001

43. Kazakov AA, Kiselev D. Industrial application of thixomet image analyzer for quantitative description of steel and alloy's microstructure. *Metallography, Microstructure, and Analysis*. 2016;5(4):294-301. DOI:10.1007/s13632-016-0289-6

44. Kazakov AA, Kovalev P, Ryaboshuk S. Metallurgical expertise as the base for determination of nature of defects in metal products. *CIS Iron and Steel Review*. 2007;(1-2):7-13.

45. Buravova SN, Petrov EV. Acceleration of mass transfer under dynamic loading. *Russian Journal of Physical Chemistry B*. 2018;12:120-128. DOI:10.1134/S1990793118010153

Information about the authors / Информация об авторах

Andrey Yu. Malakhov, Cand. Sc. (Eng.), Senior Researcher, Merzhanov Institute of Structural Macrokinetics and Materials Science Russian Academy of Sciences (ISMAN), Chernogolovka, Russian Federation; ORCID0000-0002-0567-7307; e-mail: sir.malahov2009@yandex.ru

Ivan V. Saikov, Cand. Sc. (Eng.), Leading Researcher, Deputy director of the ISMAN, Chernogolovka, Russian Federation; ORCID 0000-0003-1473-2854; e-mail: revan.84@mail.ru

Igor V. Denisov, Cand. Sc. (Eng.), Researcher, ISMAN, Chernogolovka, Russian Federation; ORCID 0000-0002-1065-3318; e-mail: ingener.denisov@yandex.ru

Alexander A. Berdychenko, Cand. Sc. (Eng.), Associate Professor, Head of the Department of the Polzunov Altai State Technical University (ASTU), Barnaul, Russian Federation; e-mail: berd50@mail.ru

Sergey G. Ivanov, D. Sc. (Eng.), Leading Researcher of the ASTU, Barnaul, Russian Federation; ORCID 0000-0002-5965-0249; e-mail: serg225582@mail.ru

Nemat N. Niyozbekov, Junior Researcher, ISMAN, Chernogolovka, Russian Federation; ORCID0000-0003-1812-2930; e-mail: nemat199595@mail.ru

Малахов Андрей Юрьевич, кандидат технических наук, старший научный сотрудник, ФГБУН «Институт структурной макрокинетики и проблем материаловедения им. А. Г. Мерджанова Российской академии наук (ИСМАН), Черноголовка, Российская Федерация; ORCID 0000-0002-0567-7307; e-mail: sir.malahov2009@yandex.ru

Сайков Иван Владимирович, кандидат технических наук, ведущий научный сотрудник, заместитель директора по научной работе ИСМАН, Черноголовка, Российская Федерация; ORCID 0000-0003-1473-2854; e-mail: revan.84@mail.ru

Денисов Игорь Владимирович, кандидат технических наук, научный сотрудник, ИСМАН, Черноголовка, Российская Федерация; ORCID 0000-0002-1065-3318; e-mail: ingener.denisov@yandex.ru

Бердыченко Александр Анатольевич, кандидат технических наук, доцент, заведующий кафедрой современных специальных материалов, Алтайский государственный технический университет им. И. И. Ползунова (АлтГТУ), Барнаул, Российская Федерация; e-mail: berd50@mail.ru

Иванов Сергей Геннадьевич, доктор технических наук, ведущий научный сотрудник, АлтГТУ, Барнаул, Российская Федерация; ORCID 0000-0002-5965-0249; e-mail: serg225582@mail.ru

Нийёзбеков Нёмат Нийёзбекович, младший научный сотрудник, ИСМАН, Черноголовка, Российская Федерация; ORCID 0000-0003-1812-2930; e-mail: nemat199595@mail.ru

Received 18 September 2023; Accepted 03 November 2023; Published 15 December 2023



Copyright: © Malakhov AY, Saikov IV, Denisov IV, Berdychenko AA, Ivanov SG, Niyozbekov NN, 2023. This article is an open access article distributed under the terms and conditions of the Creative Commons Attribution (CC BY) license (<https://creativecommons.org/licenses/by/4.0/>).

Evaluation of the effect of a complex nanomodifying additive “lignosulfonate / graphene oxide” on the non-autoclaved aerated concrete hydration process

© Dhafer Z. M. Aljaboobi^a, Irina V. Burakova^a✉, Alexander E. Burakov^a, Vladimir O. Yarkin^a

^a Tambov State Technical University,
Bld. 2, 106/5, Sovetskaya St., Tambov, 392000, Russian Federation

✉ iris_tamb68@mail.ru

Abstract: The article evaluates the influence of various plasticizing and structure-forming additives on the hydration process of non-autoclaved aerated concrete (NAC). The authors have developed a method for the NAC formation with the introduction of the following modifiers: lignosulfonate (LS), graphene oxide (GO) (1 % aqueous suspension) and a complex additive – GO/LS. The formation of the structure and the study of new mineral formations in cement stone as a result of hydration were carried out by X-ray diffraction and differential thermal analysis. According to XRD-analysis, gas blocks of all compositions contain quartz, tobermorite, calcium hydrogarnets, xonotlite, C–S–H(I), and calcite. The diffraction pattern of the sample with the addition of GO/LS shows that NAC contains, first of all, high-intensity reflections of tobermorite, xonotlite, as well as C–S–H and calcite. All other NAC samples are characterized by a lower intensity of reflections of the indicated calcium hydrosilicates. TG- and DSC-curves for all studied gas blocks have a similar character – 3 stages of weight loss, except for the control sample. Aerated concrete without additives at temperatures up to 100 °C loses 0.96 % of its weight, with the addition of LS – 1.20 %, GO – 1.35 %, and complex additive – 1.72 %. In the temperature range of 400–500 °C, an endothermic effect appears, which indicates the dehydration of weakly crystallized gel-like hydrosilicates and calcium hydrogarnets. It is this peak that is absent in the control sample. Thus, based on the diagnostic results, it was established that the complex modifying additive allow to increase of the hydration product crystallinity of the hardened NAC. The results suggest that the modified NAC containing a complex additive is more stable and functional during operation than comparative samples of concrete of a traditional composition without this additive.

Keywords: non-autoclaved aerated concrete; lignosulfonate; graphene oxide; complex additive; X-ray diffraction; differential thermal analysis; calcium hydrosilicate; binding material hydration.

For citation: Aljaboobi DZM, Burakova IV, Burakov AE, Yarkin VO. Evaluation of the effect of a complex nanomodifying additive “lignosulfonate/graphene oxide” on the non-autoclaved aerated concrete hydration process. *Journal of Advanced Materials and Technologies*. 2023;8(4):316-323. DOI: 10.17277/jamt.2023.04.pp.316-323

Оценка влияния комплексной наномодифицирующей добавки «лигносульфонат / оксид графена» на процесс гидратации неавтоклавного газобетона

© Д. З. М. Альджабуоби^a, И. В. Буракова^a✉, А. Е. Бураков^a, В. О. Яркин^a

^a Тамбовский государственный технический университет,
ул. Советская, 106/5, пом. 2, Тамбов, 392000, Российская Федерация

✉ iris_tamb68@mail.ru

Аннотация: Проведена оценка влияния различных пластифицирующих и структурообразующих добавок на процесс гидратации неавтоклавного газобетона (НГБ). Разработана методика формирования НГБ с введением следующих модификаторов: лигносульфоната (ЛС), оксида графена (ОГ) (1 % водная суспензия) и комплексной добавки – ОГ/ЛС. Формирование структуры и исследование минеральных новообразований в цементном камне в результате гидратации проводились методом рентгеноструктурного и дифференциально-термического анализа.

Согласно рентгеновской дифрактометрии, газоблоки всех составов содержат кварц, тоберморит, гидрогранаты кальция, ксонотлит, C–S–H(I), кальцит. Дифрактограмма образца с добавкой ОГ/ЛС показывает, что НГБ содержит, прежде всего, высокоинтенсивные отражения тоберморита, ксонотлита, а также C–S–H и кальцита. Для всех остальных образцов НГБ характерна более низкая интенсивность рефлексов указанных гидросиликатов кальция. ТГ- и ДСК-кривые для всех исследуемых газоблоков имеют схожий характер – 3 ступени потери массы, кроме контрольного образца. Газобетон без добавок при температуре около 100 °С теряет 0,96 % массы, с добавкой ЛС – 1,20 %, ОГ – 1,35 %, комплексной добавки – 1,72 %. В интервале температур 400...500 °С появляется эндотермический эффект, который говорит о дегидратации слабозакристаллизованных гелеобразных гидросиликатов и гидрогранатов кальция. Именно этот пик отсутствует у контрольного образца. Таким образом, по результатам диагностики установлено, что комплексная модифицирующая добавка увеличивает кристалличность продуктов гидратации затвердевшего НГБ. Результаты позволяют предположить, что модифицированный НГБ, содержащий комплексную добавку, является более стабильным и функциональным в процессе эксплуатации, чем сравнительные образцы бетона традиционного состава без такой добавки.

Ключевые слова: неавтоклавный газобетон; лигносульфонат; оксид графена; комплексная добавка; рентгеновская дифрактометрия; дифференциально-термический анализ; гидросиликат кальция; гидратация вяжущего.

Для цитирования: Aljaboobi DZM, Burakova IV, Burakov AE, Yarkin VO. Evaluation of the effect of a complex nanomodifying additive “lignosulfonate/graphene oxide” on the non-autoclaved aerated concrete hydration process. *Journal of Advanced Materials and Technologies*. 2023;8(4):316-323. DOI: 10.17277/jamt.2023.04.pp.316-323

1. Introduction

The use of materials with thermal insulation properties is an urgent task and is of great importance for the development of the construction industry. For these purposes, so-called cellular concrete is successfully used, the category of which includes foam concrete, foam aerated concrete, autoclaved and non-autoclaved aerated concrete, etc. Aerated concrete is successfully used for wall construction – both external and internal (blocks, panels), floors (slabs), fences, etc., as well as for construction of frame structures [1, 2].

Autoclave gas blocks are produced only in factory conditions in accordance with Russian Standard 31360-2007 using high-pressure reactors – autoclaves. Non-autoclaved aerated concrete is produced in accordance with Russian Standard 25485-89 without the use of expensive equipment at the construction site. As is known, average density and strength are the main parameters by which the choice of thermal insulation building material is made. At the same density, non-autoclaved aerated concrete will exhibit lower mechanical characteristics than autoclaved one, which primarily affects its load-bearing capacity. Therefore, the urgent task is to develop the composition of a non-autoclaved aerated concrete mixture that provides high strength indicators along with good thermal insulation properties [3].

The mechanical properties of concrete materials are greatly influenced by micro- and nanoscale reactions occurring in the cement paste during the hydration process. A number of studies have proven that the addition of nanodispersed particles can

improve the properties of concrete due to the fact that nanoparticles act as nucleation sites for the growth of the C–S–H gel framework. The nucleation of hydration products on nanoparticles promotes and accelerates the hydration of cement [4–8].

In [9], the authors obtained compositions of non-autoclaved aerated concrete with the addition of carbon nanomaterial (CNM) and a composite binder – fly ash. It has been proven that the introduction of CNM leads to an increase in the strength characteristics of aerated concrete by 15–20 % due to changes in the hydration process and the formation of additional amounts of calcium hydrosilicates according to IR spectroscopy.

The authors [10] studied autoclaved silicate aerated concrete modified with ultrafine mineral additives with a concentration of 5–10 % and a dispersion of multi-walled carbon nanotubes (MWCNTs) up to 0.001–0.005 % by weight of the binder. In this way, products were obtained from autoclaved aerated concrete with a density of 540–580 kg·m⁻³ with a compressive strength of 3.4–3.9 MPa, i.e. an improvement in the strength characteristics of products up to 30 % is achieved compared to the control sample.

The introduction of MWCNTs dispersion in an amount of 0.002 % by weight of Portland cement in the production of autoclaved aerated concrete [11] contributed to the production of samples with a density of 180–200 kg·m⁻³ with a compressive strength of 0.7–0.9 MPa, a thermal conductivity of 0.046 was 0.048 W·(m·°C)⁻¹. The authors of [11] state that the addition of nanoparticles leads to a change in the morphology of hydration products,

which are intertwined plate-like and needle-shaped crystals of low-basic calcium hydrosilicates. Thanks to this, a strong spatial frame of the composite is formed, less susceptible to cracking and destruction.

A team of authors [12] published a study of the effect of a 1–2 % MWCNTs suspension using carboxymethylcellulose as a surfactant on the quality and characteristics of autoclaved (AAC) and non-autoclaved aerated concrete (NAC). It has been established that modification makes it possible to increase the bending strength of NAC to 11.23 %, AAC – up to 25.00 %; and compressive strength of NAC – up to 11.03 %, AAC – up to 24.50 %.

There are works aimed at modifying cement stone with graphene oxide (GO), graphene nanoplates, etc. [13–15]. Research results [16] show that the addition of multilayer graphene can achieve an increase in compressive strength by 54 % and flexural strength by 21 % for cementitious composites, respectively. The addition of 0.03 % GO [17] makes it possible to increase the flexural strength of cement stone by 77 % and compressive strength by 47.6 % for compositions aged 28 days. The results of modification with nanographene (multilayer graphene with a number of layers of 5–10) in an amount of 0.8 % of autoclaved aerated concrete [18] show an increase in compressive and tensile strength, as well as impact resistance by 45, 81 and 130 % compared to the control sample. At the same time, the water absorption of the samples was reduced to 61 %.

Thus, nanotechnologies and nanomaterials as modifying additives can be effectively used to improve the properties of concrete, increase their mechanical characteristics, thermal insulation capacity, and, as a result, increase the durability of building structures built on their basis.

The purpose of this work is to identify the influence of additives, in particular, based on GO and lignosulfonate, on non-autoclaved aerated concrete by studying cement stone using X-ray diffraction and differential thermal analysis.

2. Materials and Methods

2.1. Materials

To obtain NAC samples, Portland cement M500 (Paladium, Zhukovsky, Russia), dry sand Russian Standard 8736-2014, slaked construction carbonate-lime flour (LLC “StroyKomplekt”, Voronezh, Russia), aluminum powder, tap water (ratio water/cement was 0.4) were taken. To modify NAC, powdered lignosulfonate (AKVAKHIM LLC, Kazan, Russia) and a 1 % aqueous GO suspension (NanoTechCenter LLC, Tambov) were used.

2.2. Preparation of GO/LS non-autoclave aerated concrete specimens

Samples of aerated blocks were prepared with an GO/LS content of 0.0002 wt. % and 0.16 wt. % LS by weight of cement. NAC samples were also obtained only with the addition of GO at the indicated concentration and separately with the addition of 0.16 wt. % LS. To prepare the modifying additive, the following procedure was developed:

a) at the first stage, an aqueous solution of lignosulfonate was obtained: the required amount of lignosulfonate powder was added to distilled water heated to 80 °C and stirred continuously for 10–15 minutes;

b) the pH of the aqueous GO suspension was adjusted to 10 by adding 1 M NaOH solution. The pH was measured using a HI 2210 benchtop pH meter (HANNA Instruments, Woonsocket, USA);

c) a suspension of GO was added to LS solution cooled to room temperature and kept at 90 °C.

2.3. Test methods and specimens

For each cement composition, cubes measuring 70×70×70 mm were cast to determine compressive strength and 40×40×160 mm to assess flexural strength. The compaction of the aerated concrete mixture was carried out on a vibration platform in accordance with Russian Standard 17674-72 with the mandatory presence of a vertical component of vibrations. On the 7th day of hardening, the cubes were removed to continue strengthening (28 days). To determine the compressive strength, an IP-500 press with a maximum force of 50 tons (JSC ZIPO, Armavir) was used, and the bending strength was determined using a uniaxial testing machine with a power of 2000 kN and an applied load of 0.4 MPa·s⁻¹.

2.4. Analytic methods

The study of new mineral formations in cement stone was carried out by X-ray phase analysis using a Thermo Scientific ARL Equinox 1000 X-ray diffractometer (TechTrend Science Co., Ltd., Taiwan) (wavelength $\lambda = 0.1540562$ nm (copper anode). Determination of weight change under temperature influence were carried out using a NETZSCH STA 449 F3 Jupiter instrument (NETZSCH-Feinmahltechnik GmbH, Selb, Germany) with simultaneous thermogravimetric analysis (TGA) and differential scanning calorimetry (DSC) (measurement in the air atmosphere at a heating rate of 10 K·min⁻¹).

3. Results and Discussion

It is well known that the hydration process of Portland cement represents a series of chemical transformations [19]. When water interacts with cement grains, a chemical reaction occurs, due to which needle-shaped crystals appear on the surface of the grains and in the water. Over a short time, the volume of these new formations increases, and the cement grains form a developed spatial network among themselves. After 8–10 hours, the gelation process continues and the entire volume, in which cement grains gradually decrease, is filled with calcium hydrosilicates, aluminates, sulfoaluminates, ferrites, sulfoferrites and hydrogarnets (depending on hydration conditions, the composition of the concrete mixture, etc.). The remaining voids are filled, although not so intensively, with hydration products, i.e. clinker minerals. The resulting silicate structure turns into cement stone and after a day begins to

displace the aluminate structure. After completion of the hydration process, the cement stone hardens and becomes strong [20].

The formation of the cellular structure of aerated concrete occurs as a result of a chemical reaction between the gas-forming agent and the component actively acting on it with the release of gas. The expansion of the forming micropores continues as a result of the pressure that the gas exerts on the pore walls and the concrete mixture in contact with them. In this work, aluminum powder was used as a gas generator; when interacting with calcium hydroxide, hydrogen is formed.

According to XRD-analysis (Fig. 1), NAC samples – both original and modified – contain the following compounds: quartz (β -SiO₂); tobermorite ($5\text{CaO} \cdot 3\text{SiO}_2 \cdot \text{H}_2\text{O}$); calcium hydrogarnets ($3\text{CaO} \cdot x\text{Al}_2\text{O}_3 \cdot x\text{SiO}_2 \cdot (6-2x)\text{H}_2\text{O}$); xonotlite ($6\text{CaO} \cdot 6\text{SiO}_2 \cdot x\text{H}_2\text{O}$); C–S–H(I); calcite CaCO_3 .

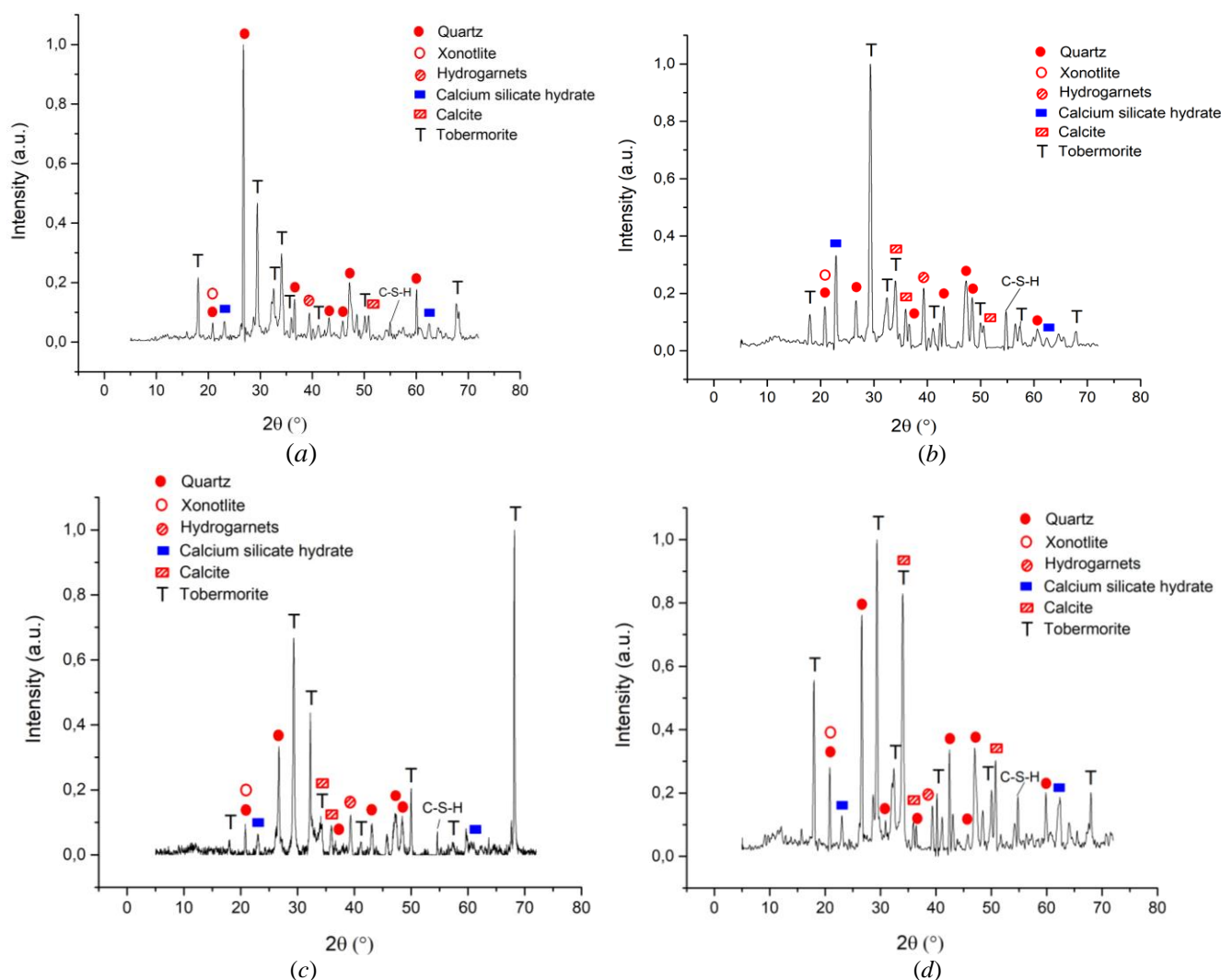


Fig. 1. X-ray diffraction patterns of NAC samples: *a* – control; *b* – modified LS; *c* – modified GO; *d* – modified with a complex additive

The X-ray spectrum of unmodified NAC shows reflections of quartz with high intensity peaks at $2\theta = 26.5, 37, 46.5, 60^\circ$ (Fig. 1, *a*). Peaks of calcium hydrosilicates, such as tobermorite and xonotlite, have a lower intensity value. The resulting diffraction pattern suggests an insufficient degree of crystallinity and heterogeneity of new formations that are formed as a result of hydration of cement stone. Also, the diffraction pattern of the control sample contains low-intensity reflections corresponding to hydrogarnets and calcite.

Aerated concrete samples modified with lignosulfonate (Fig. 1, *b*), according to XRD-analysis, contain large quantities of reflections related to low-basic calcium hydrosilicates, in particular, tobermorite, C–S–H, and xonotlite. It is noteworthy that the introduction of LS significantly increased the intensity of the tobermorite peaks, especially at $2\theta = 29^\circ$, and the intensity of the quartz peak at $2\theta = 26.5^\circ$ decreased several times. The intensity of the peak corresponding to xonotlite also increased (at $2\theta = 21^\circ$). The observed changes in the crystalline pattern in gas silicate are explained by the fact that heterogeneous reactions of calcium hydroxide and silicon-containing components in the aerated concrete mixture occur more fully [19].

The introduction of graphene oxide into the composition of the aerated concrete mixture (Fig. 1, *c*) also contributes to a change in the crystal structure of mineral new formations, as does the addition of drugs. Compared to the control sample, the intensity of diffraction reflections of tobermorite, xonotlite and hydrogarnets increases in NAC modified with GO. It is known that calcium hydrogarnets also participate in the structure formation of aerated concrete mixtures and increase the durability of products.

The X-ray diffraction pattern of NAC (Fig. 1, *d*), modified with a complex additive of GO/LS, shows a significant difference in the diffraction pattern of this sample from the previous ones. The difference lies in the high intensity of reflections primarily from tobermorite, xonotlite, as well as C–S–H and calcite. This fact suggests that the mineral new formations formed during the NAC hydration are well crystallized and form a strong framework of hydration products, thereby increasing the strength of aerated concrete due to the strengthening of inter pore partitions [19].

The results obtained during the differential thermal analysis of the NAC samples studied in the article are presented in Fig. 2.

According to TG- and DSC-curves, at temperatures up to 100–150 °C, water is removed

from low-basic calcium hydrosilicates of the tobermorite type, which is accompanied by heat absorption [12].

A pronounced endothermic effect in the temperature range of 400–450 °C indicates the dehydration of gelled hydrosilicates and calcium hydrogarnets. Small endo-effects at temperatures from 550–900 °C arise due to the decomposition of calcium bicarbonates formed during the carbonization of aerated concrete [21].

In general, the TG- and DSC-curves for all studied materials have a similar character as described above – 3 stages of weight loss, except for the control sample.

Aerated concrete without additives at a temperature of about 100 °C loses 0.96 % of its weight, with the addition of LS – 1.20 %, GO – 1.35 %, complex additive – 1.72 %. An increase in the percentage of residual weight in a given area indicates that the volume of water adsorbed by the sample is increasing. This fact allows us to assert that the introduction of a complex GO/LS additive increases the porosity of aerated concrete [12].

At the next stage in the temperature range of 400–450 °C, which is observed only in modified NAC samples, a slight weight loss of about 1 % is recorded for all samples. Recording of weight loss stops at 1098 °C. Up to this point, in the range of 550–700 °C, the weight of the modified samples decreases by an average of 4 %. The lowest value of the residual weight of NAC is observed for the control sample – 84.47 %, with the addition of LS – 86.40 %, GO – 87.10 %, complex additive – 87.57 %. This fact suggests that NAC with the addition of GO/LS is more durable and less susceptible to thermal influences.

Thus, as a result of X-ray diffraction and differential thermal analysis of cellular concrete samples, the effectiveness of introducing a complex GO/LS additive has been proven, which has a positive effect on the structure formation of cement stone and the morphology of hydration products – new formations of gas silicate.

It should also be noted that the patterns found as a result of the physical and structural analysis are correlated with the data of mechanical tests of the gas blocks under consideration (Table 1) [22].

It has been established that the complex additive allows to obtain the highest values of the mechanical characteristics of NAC: an increase in bending strength by 30 % and compressive strength by 35 % is achieved.

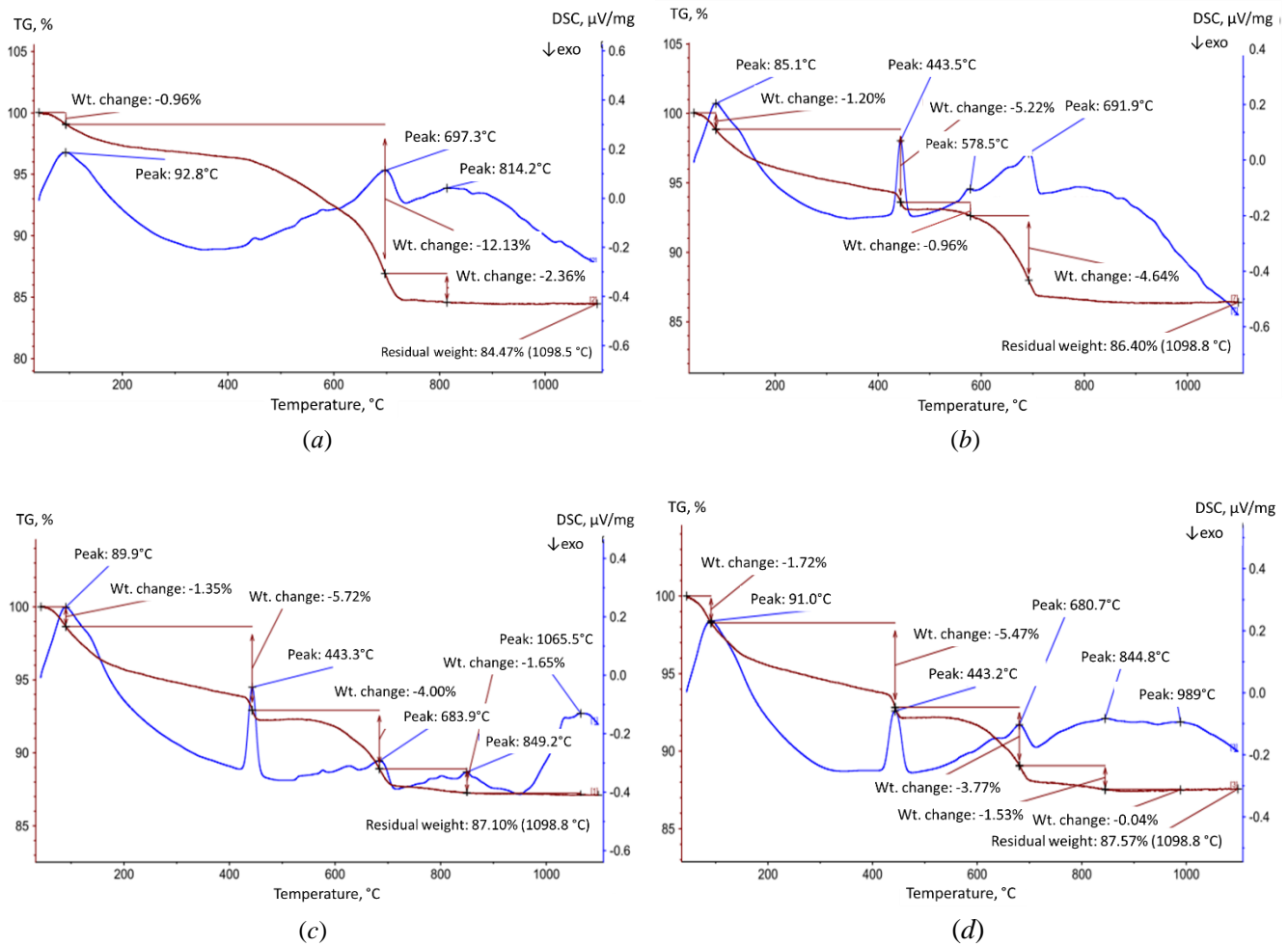


Fig. 2. TG- and DSC-curves of NAC samples: *a* – control; *b* – modified LS; *c* – modified GO; *d* – modified with a complex additive

Table 1. Flexural and compressive strength values of NAC

Samples	Control	LS additive	GO additive	GO/LS additive
Bending strength, MPa	1.15	1.38	1.27	1.67
Compressive strength, MPa	1.25	1.45	1.53	1.92

4. Conclusion

Using the methods of differential thermal and X-ray diffraction analysis, the quantitative and qualitative content of hydration products of cement stone of NAC samples modified with additives of LS, GO and the complex composition of GO/LS was assessed. XRD-analysis made it possible to determine the phase composition of new formations that arise during the hydration of the binder, as well as to

evaluate the influence of various types of additives on the NAC crystallization. It was established that all the obtained gas blocks contain quartz, tobermorite-like calcium hydrosilicates, calcium hydrogarnets, xonotlite, C–S–H(I), calcite CaCO_3 . When modifying NAC with a complex additive of GO/LS, an increase in the reflections of tobermorite, xonotlite and C–S–H(I) is observed, which allows to speak about an increase in the crystallinity degree of new mineral formations of cement stone. According to the results of TG- and DSC-analysis, endothermic effects caused by dehydration of calcium hydrosilicates and destruction of their structure were discovered. The thermograms of all samples revealed three main endo-effects associated with the removal of adsorbed water from gel-like hydration products, dehydration of low-basic calcium hydrosilicates, and decomposition of calcium carbonate. The obtained XRD and TG/DSC analysis data are in good agreement with strength tests demonstrating the effectiveness of using the complex GO/LS additive for modifying NAC.

5. Funding

This study received no external funding.

6. Acknowledgments

This work was done using facilities of the shared access center "Production and application of multifunctional nanomaterials" (Tambov State Technical University).

7. Conflict of interests

The authors declare no conflict of interest.

References

1. Narayanan N, Ramamurthy K. Structure and properties of aerated concrete: A review. *Cement and Concrete Composites*. 2000;22(5):321-329. DOI:10.1016/S0958-9465(00)00016-0
2. Mousa MA, Uddin N. Experimental and analytical study of carbon fiber- reinforced polymer (FRP)/autoclaved aerated concrete (AAC) sandwich panels. *Engineering Structures*. 2009;31(10):2337-2344. DOI:10.1016/j.engstruct.2009.05.009
3. Qu X, Zhao X. Previous and present investigations on the components, microstructure and main properties of autoclaved aerated concrete – A review. *Construction and Building Materials*. 2017;135:505-516. DOI:10.1016/j.conbuildmat.2016.12.208
4. Sldozian RJ, Tkachev AG, Burakova IV, Mikhaleva ZA. Improve the mechanical properties of lightweight foamed concrete by using nanomodified sand. *Journal of Building Engineering*. 2020;34:101923. DOI:10.1016/j.job.2020.101923
5. Yakovlev GI, Pervushin GN, Polyanskikh IS, Kerene Ya, Machulaitis R, Pudov IA, Senkov SA, Politaeva AI, Gordina AF, Shaibadullina AV. *Nanostructuring of composites in construction materials science*. Izhevsk: IzhSTU im. M.T. Kalashnikov Publ. house; 2014. 196 p. (In Russ.)
6. Tolchikov YuN, Aljaboobi DZM. Research into the process of synthesis of carbon nanomaterials on the cement binder. *Journal of Advanced Materials and Technologies*. 2022;7(4):290-298. DOI:10.17277/jamt.2022.04.pp.290-298
7. Geraldo V, Oliveira S, Silva EE, Souza Oliveira CA, Almeida Cunha RM, Pontes de Oliveira RF, et al. Synthesis of carbon nanotubes on sand grains for mortar reinforcement. *Construction and Building Materials*. 2020;252:119044. DOI:10.1016/j.conbuildmat.2020.119044
8. Du S, Wu J, Alshareedah O, Shi X. Nanotechnology in cement-based materials: A review of durability, modeling, and advanced characterization. *Nanomaterials*. 2019;9(9):1213. DOI:10.3390/nano9091213
9. Ajen NM, Akmalayuly K. Application of composite binders and carbon nanomaterials for the production of aerated concrete. *Nauka i innovatsionnyye tekhnologii*. 2022;2(23):91-98. DOI:10.33942/sititpr202257 (In Russ.)
10. Yakovlev GI, Pervushin GN, Kerene Ya, Polyanskikh IS, Pudov IA, Khazeev DR, Senkov SA. Complex additive based on carbon nanotubes and microsilica for modifying autoclaved gas silicate. *Stroitel'nyye materialy*. 2014;1-2:3-7. (In Russ.)
11. Leontyev SV, Golubev VA, Shamanov VA, Kurzanov AD, Yakovlev GI, Khazeev DR. Modification of the structure of heat-insulating autoclaved aerated concrete with a dispersion of multi-walled carbon nanotubes. *Stroitel'nyye materialy*. 2016;1-2:76-83. (In Russ.)
12. Keriene J, Kligys M, Laukaitis A, Yakovlev G, Špokauskas A, Aleknevičius M. The influence of multi-walled carbon nanotubes additive on properties of non-autoclaved and autoclaved aerated concretes. *Construction and Building Materials*. 2013;49:527-535. DOI:10.1016/j.conbuildmat.2013.08.044
13. Mohammadi MR, Ahmadi J, Mohammadi S. The effect of graphene nano particle on the mechanical and durability properties of Portland cement concrete. *Concrete Research*. 2020;12(1):109-118. DOI:10.22124/jcr.2019.9173.1249
14. Devi SC, Khan RA. Mechanical and durability performance of concrete incorporating graphene oxide. *Journal of Materials and Engineering Structures*. 2019;6:201-214.
15. Strokova VV, Laketich SK, Nelyubova VV, Zhenmao YE. Graphene oxide as a modifier for cement systems: analysis of the state and development prospects. *Stroitel'nyye materialy*. 2021;1-2:37-90. DOI:10.31659/0585-430X-2021-788-1-2-37-89 (In Russ.)
16. Han B, Zheng Q, Sun S, Dong S, Zhang L, Yu X, Ou J. Enhancing mechanisms of multi-layer graphenes to cementitious composites. *Composites Part A: Applied Science and Manufacturing*. 2017;101:143-150. DOI:10.1016/j.compositesa.2017.06.016
17. Indukuri CSR, Nerella R. Enhanced transport properties of graphene oxide-based cement composite material. *Journal of Building Engineering*. 2021;37:102174. DOI:10.1016/j.job.2021.102174
18. Seddighi F, Pachideh G, Salimbahrami SB. A study of mechanical and microstructures properties of autoclaved aerated concrete containing nano-graphene. *Journal of Building Engineering*. 2021;43:103106. DOI:10.1016/j.job.2021.103106
19. MacLeod AJN, Collins FG, Duan W, Gates WP. Quantitative microstructural characterisation of Portland cement-carbon nanotube composites using electron and X-ray microscopy. *Cement and Concrete Research*. 2019;123:105767. DOI:10.1016/j.cemconres.2019.05.012
20. Marchon D, Flatt RJ. Mechanisms of cement hydration. In: *Science and Technology of Concrete*

Admixtures. Elsevier Inc.; 2016. p. 129-145.
DOI:10.1016/B978-0-08-100693-1.00008-4

21. Makarova IA, Lokhova NA. *Physico-chemical methods for studying building materials*. Bratsk State University Publ. house; 2011. 139 p. (In Russ.)

22. Aljaboobi DZM, Burakova IV, Burakov AE, Sldozian RJ, Tkachev AG. Production of non-autoclaved aerated concrete with graphene oxide and plasticizer additives. *Izvestiya vysshikh uchebnykh zavedeniy. Stroitel'stvo*. 2023;(3):52-60. DOI:10.32683/0536-1052-2023-771-3-52-60 (In Russ.)

Information about the authors / Информация об авторах

Dhafer Z. M. Aljaboobi, Engineer, AMA LLC, PhD candidate, Tambov State Technical University (TSTU), Tambov, Russian Federation; ORCID 0000-0002-8248-5050; e-mail: aldjabubi.dzm@mail.tstu.ru

Irina V. Burakova, Cand. Sc. (Eng.), Associate Professor, TSTU, Tambov, Russian Federation; ORCID 0000-0003-0850-9365; e-mail: iris_tamb68@mail.ru

Alexander E. Burakov, Cand. Sc. (Eng.), Associate Professor, TSTU, Tambov, Russian Federation; ORCID 0000-0003-4871-3504; e-mail: m-alex1983@yandex.ru

Vladimir O. Yarkin, Student, TSTU, Tambov, Russian Federation; e-mail: sttstu90@gmail.com

Альджабуи Дхафер Зейд Мохаммед, инженер, ООО «АМА», соискатель, Тамбовский государственный технический университет (ТГТУ), Тамбов, Российская Федерация; ORCID 0000-0002-8248-5050; e-mail: aldjabubi.dzm@mail.tstu.ru

Буракова Ирина Владимировна, кандидат технических наук, доцент, ТГТУ, Тамбов, Российская Федерация; ORCID 0000-0003-0850-9365; e-mail: iris_tamb68@mail.ru

Бураков Александр Евгеньевич, кандидат технических наук, доцент, ТГТУ, Тамбов, Российская Федерация; ORCID 0000-0003-4871-3504; e-mail: m-alex1983@yandex.ru

Яркин Владимир Олегович, студент, ТГТУ, Тамбов, Российская Федерация; e-mail: sttstu90@gmail.com

Received 13 September 2023; Accepted 26 October 2023; Published 15 December 2023



Copyright: © Aljaboobi DZM, Burakova IV, Burakov AE, Yarkin VO, 2023. This article is an open access article distributed under the terms and conditions of the Creative Commons Attribution (CC BY) license (<https://creativecommons.org/licenses/by/4.0/>).

Synthesis of the TiC + 20 % NiCr composite from a granular mixture

© Nail I. Abzalov^a, Boris S. Seplyarskii^a✉, Roman A. Kochetkov^a,
Tatiana G. Lisina^a, Mikhail I. Alymov^a

^a Merzhanov Institute of Structural Macrokinetics and Materials Science RAS (ISMAN),
8, Academician Osipyan St., Chernogolovka, 142432, Russian Federation

✉ seplb1@mail.ru

Abstract: For the first time, the synthesis of the TiC + 20 % NiCr composite from a granular mixture with titanium of different dispersion, containing different amounts of impurity gases, was carried out. The features of the combustion process of a granular charge are explained by its structure – the presence of physically separated cells (granules) with a powder mixture, which can ignite because of conductive heat transfer from granule to granule or convective heating by gas released from the charge. The combustion front in the powder and granular charge based on titanium with a smaller characteristic size of titanium particles propagated at a higher rate, despite the higher content of impurity gases in it. The effect of impurity gas release on the combustion rate of powder mixtures is explained using a convective-conductive combustion model. It is shown that the combustion of the studied mixtures with granules 0.6 and 1.7 mm in size took place in a safe conductive mode, making it possible to scale the process. X-ray phase analysis of the combustion products showed that the phase composition of the synthesis products did not depend on the size of the granules. When using a granular mixture containing finely dispersed titanium powder, synthesis products were obtained without side phases of intermetallic compounds, which were easily crushed to micron sizes and could be used for plasma spraying of wear-resistant coatings.

Keywords: combustion synthesis; protective coating; granules; titanium particle size; impurity outgassing.

For citation: Abzalov NI, Seplyarskii BS, Kochetkov RA, Lisina TG, Alymov MI. Synthesis of the TiC + 20 % NiCr composite from a granular mixture. *Journal of Advanced Materials and Technologies*. 2023;8(4):324-332. DOI: 10.17277/jamt.2023.04.pp.324-332

Синтез композита TiC + 20 % NiCr из гранулированной шихты

© Н. И. Абзалов^a, Б. С. Сеплярский^a✉, Р. А. Кочетков^a,
Т. Г. Лисина^a, М. И. Алымов^a

^a Институт структурной макрокинетики и проблем материаловедения
им. А. Г. Мерджанова Российской академии наук (ИСМАН),
ул. Академика Осипяна, 8, Черноголовка, Московская область, 142432, Российская Федерация

✉ seplb1@mail.ru

Аннотация: Впервые проведен синтез композита TiC + 20 % NiCr из гранулированной шихты с титаном разной дисперсности, содержащим разное количество примесных газов. Особенности процесса горения гранулированной шихты объяснены ее структурой – наличием физически выделенных ячеек (гранул) с порошковой смесью, воспламенение которых может происходить вследствие кондуктивной передачи тепла от гранулы к грануле или конвективного нагрева газом, выделяющимся из шихты. Фронт горения в порошковой и гранулированной шихте на основе титана с меньшим характерным размером частиц титана распространялся с более высокой скоростью, несмотря на более высокое содержание примесных газов в ней. Влияние примесного газовыделения на скорость горения порошковых смесей объяснено с использованием конвективно-кондуктивной модели горения. Показано, что горение исследованных смесей с гранулами размером 0,6 и 1,7 мм проходило в безопасном кондуктивном режиме, позволяющем масштабировать процесс. Рентгенофазовый анализ продуктов горения показал, что фазовый состав продуктов синтеза не зависел от размера гранул. При использовании гранулированной шихты, содержащей мелкодисперсный порошок титана, получены продукты синтеза без побочных фаз интерметаллидов,

которые легко дробились до микронных размеров и могут быть использованы для плазменного напыления износостойчивых покрытий.

Ключевые слова: СВС; защитное покрытие; гранулы; размер частиц титана; примесное газовыделение.

Для цитирования: Abzalov NI, Seplyarskii BS, Kochetkov RA, Lisina TG, Alymov MI. Synthesis of the TiC + 20 % NiCr composite from a granular mixture. *Journal of Advanced Materials and Technologies*. 2023;8(4):324-332. DOI: 10.17277/jamt.2023.04.pp.324-332

1. Introduction

Materials based on transition metal carbides with metal binders are increasingly used as a substitute for hard alloys based on tungsten and chromium carbides [1–14]. To reduce brittleness and increase adhesion during spraying of protective coatings, metal binders such as Ni, Mo, NiCr, Cu, etc. are introduced into titanium carbide-based powders. [15–19]. A promising area of application of TiC–NiCr composite powders is their use for protective coatings on parts of industrial equipment and machinery to protect against wear and corrosion [20]. The addition of NiCr to carbide coatings increases their resistance in oxidizing environments as Cr_2O_3 is formed, which is especially important for the use of parts at high temperatures [21, 22]. Self-propagating high-temperature synthesis (SHS, also called “combustion synthesis”) is one of the methods of producing such powders [23]. SHS is characterized by a combination of low energy consumption, high process speed, purity and homogeneity of the product obtained in one technological cycle [24–40]. In the process of synthesis, easily fusible metal binder is melted, which provides melt spreading and dispersion of initial reagents in the products. The microstructure of coatings obtained by sputtering of synthesized powders is characterized by the spherical shape of carbide grains and their homogeneous distribution over the volume of the metal matrix, which reduces the pitting of carbide inclusions [25, 41]. However, refractory and strong sintered materials produced by SHS from powder components must be crushed to micron sizes for use in sputtering [25], which requires significant energy inputs and additional operations for cleaning from the substance of grinding bodies.

Scaling up the process of obtaining composite materials by SHS requires reproducibility of combustion parameters, predictability of the properties of the obtained products, and reduction of the cost of milling the synthesis products. These objectives can be achieved by changing the structure of the mixture from powder to granular, which levels the influence of the content of impurity gases and moisture in the charge and ensures the stability of the properties of the obtained products [42]. When using granular mixtures based on titanium, the phase

composition of synthesis products depended on the dispersity and morphology of titanium powder particles [43–45]. The brittle sinter obtained as a result of synthesis was easily separated into separate granules, their grinding was not difficult and was not accompanied by contamination of grinding bodies [46]. However, depending on the content of gas-emitting components in the charge and the organic binder used in granulation, combustion can switch to a convective mode, in which the combustion rate depends quadratically on the gas mass flow [45, 47]. Since the combustion time of granules behind the ignition front is almost independent of the gas flow rate, there is a positive feedback between the combustion rate and the flow of gas filtered through the front: the higher the combustion rate, the greater the gas flow, and vice versa [48]. Therefore, in order to avoid uncontrolled growth of the combustion rate, it is necessary to carry out synthesis in the conductive mode. The authors formulated the critical conditions for the transition of combustion to the convective mode in [49].

There are no data on synthesis of titanium carbide with nichrome bond from granular mixtures (Ti + C) + 20 % NiCr in scientific literature. Therefore, the aim of the present work is, firstly, in one process operation to synthesize metal-ceramics of TiC + 20 % NiCr composition, and secondly, to find out the influence of dispersity and morphology of titanium powder and granule size on combustion modes of Ti + C + 20 % NiCr mixtures with titanium of different dispersity, phase composition of their synthesis products and the possibility of their grinding.

2. Materials and Methods

2.1. Experimental method

The combustion patterns were studied using the original experimental setup (Fig. 1).

The experiments were carried out according to the following procedure: the mixture under study 8 was poured into a vertically mounted transparent quartz tube (outer diameter – 19 mm, height – 90 mm, wall thickness – 2 mm), on a substrate of mineral wool (Al_2O_3 base) 9.

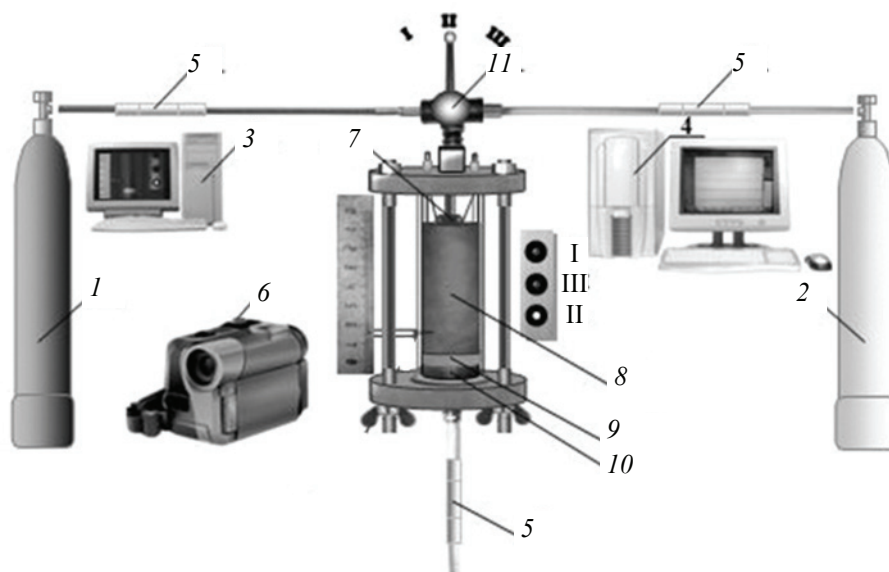


Fig. 1. Diagram of the experimental setup:

1 – cylinder with nitrogen; 2 – cylinder with argon; 3 – computer for recording the video; 4 – computer for recording sensor readings with an ADC; 5 – flow and pressure sensors; 6 – digital video camera; 7 – electric element for igniting a mixture; 8 – charge; 9 – layer of mineral wool; 10 – metal grid; 11 – gas switch (position I, nitrogen; II, argon; III, supply of gas is blocked)

Signals from sensors 5 and LEDs informing about the position of the gas supply switch 11 were fed to the computer 4 via ADC in real time mode. The thermal pulse from the tungsten spiral 7 started the combustion process from the upper end of the sample. Before each experiment, the sample was purged with a stream of argon at a pressure drop of 1 atm to avoid shrinkage of the unburned part of the backfill during combustion and to obtain stable results. The height of the initial mixture (both powder and granular) after blowing was (40 ± 5) mm.

The combustion process was recorded using a digital video camera 6 SONY FDR AX-700 (shooting speed 100–250 fps). Based on the frame-by-frame processing of the video recordings, the velocity of the combustion front was calculated.

2.2. Starting materials

The Russia-manufactured powders used in this work and their brief characteristics are given in Table 1.

Figure 2 shows the particle size distribution of the initial metal components in percentage of the total mass of the investigated powder. Further in the text and in calculations of the necessary and sufficient conditions for heating the particles of powder mixture components, their values at the point of maximum of the distribution function are used as characteristic sizes: $d(\text{Ti}) = 60$ and $120 \mu\text{m}$, $d(\text{NiCr}) = 90 \mu\text{m}$.

The external view of titanium particles with $d(\text{Ti}) = 60$ and $120 \mu\text{m}$, obtained using scanning electron microscopy, is shown in Fig. 3.

Table 1. Substances and reagents used

Components	Grade	Particle size, μm	
		up to 50 wt. %	up to 90 wt. %
Titanium:			
$d = 60 \mu\text{m}$	PTM	< 54	< 86
$d = 120 \mu\text{m}$	(Polema, Tula)	< 105	< 169
Soot	P-803	< 2.5	< 4
	(YATU, Yaroslavl)		
Nichrome,	Ni80Cr20	< 75	< 142
$d = 90 \mu\text{m}$	(Polema, Tula)		
Polyvinylbutyral (POLYMER-DZ, Dzerzhinsk)			
Ethyl alcohol technical 95 % (Ferein, Elektrogorsk)			

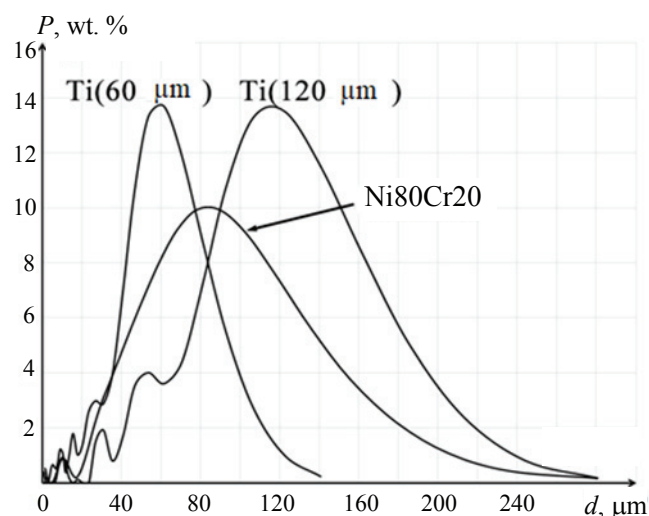


Fig. 2. Particle size distribution of the initial metal components as a percentage of the total mass of the powder under study

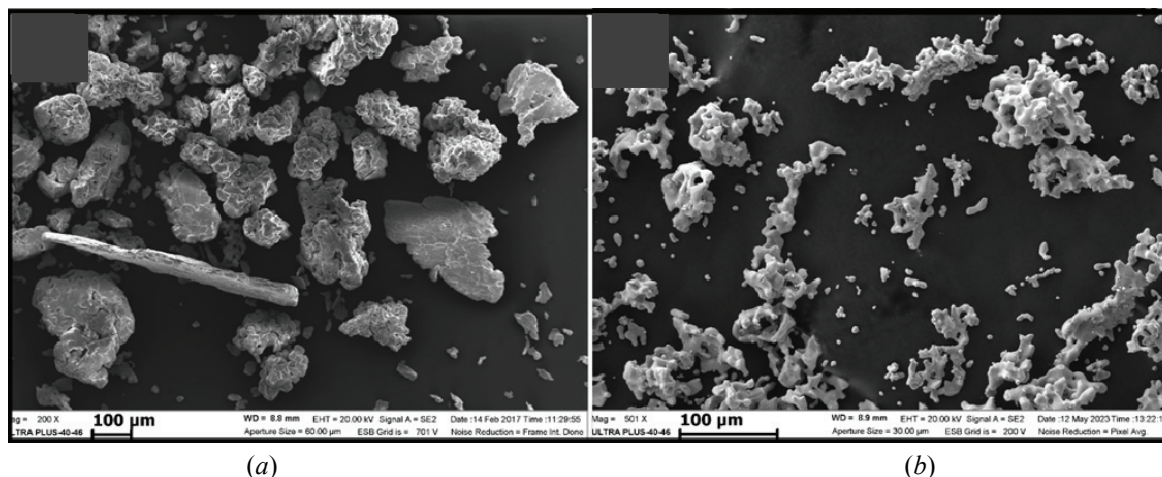


Fig. 3. Micrographs of titanium powders with $d(\text{Ti}) = 120 \mu\text{m}$ (a) and with $d(\text{Ti}) = 60 \mu\text{m}$ (b)

As can be seen from the photographs, titanium particles with $d(\text{Ti}) = 120 \mu\text{m}$ have a lentil-like shape, which is smoother than that of dendritic particles with $d(\text{Ti}) = 60 \mu\text{m}$. To determine the amount of impurity gases in titanium powders of different dispersity, a sample weighing $(100 \pm 0.01) \text{ g}$ was placed in a vacuum chamber under standard conditions and the pressure was reduced to 2.6 Pa. At 300 °C, the sample was kept in vacuum for 40 min. The sample was then heated to 850 °C and held at this temperature for 60 minutes. After the chamber had cooled to room temperature, the sample was removed and reweighed to determine the mass loss during processing.

2.3. Granulation

Granulation of the compositions was carried out as follows: preliminary initial powder mixture was mixed for 4 h in a gravity-type mixer. Then a four per cent (wt.) solution of polyvinyl butyral in ethyl alcohol was added to the obtained mixture. The paste-like mass obtained after mixing was rubbed through a sieve with mesh size of 1.25 and 1.6 mm. The obtained particles were rolled on a rotating horizontal surface to give them spherical shape. The particles were then air dried for 10 h and dispersed on a vibrating screen. The content of polyvinyl butyral in the dry mixture was about 1 %. Granules with sizes of 0.4–0.8 and 1.4–2.0 mm were used for the experiments. The half sum of the upper and lower size limits, i.e., 0.6 and 1.7 mm, respectively, was taken as the characteristic size of the granule fraction.

The stoichiometry of initial mixtures was calculated for obtaining metal-ceramics of 80 % TiC + 20 % NiCr composition. Thermodynamic calculations were performed using the THERMO software package (<http://www.ism.ac.ru/thermo/>). The calculated maximum combustion temperature of the mixture $T_{\text{ad}} = 2890 \text{ K}$.

2.4. Methods of analysis

To determine the particle size distribution of the components, a laser analyser Microsizer-201C (VA Instalt, St. Petersburg, Russia) was used. The phase composition of the final product was studied on X-ray diffractometer DRON-3M (IC Bourevestnik, St. Petersburg, Russia) using monochromatic $\text{CuK}\alpha$ -radiation. The diffractograms were taken in step-scanning mode in the range of angles $2\theta = 20\text{--}80^\circ$ with an imaging step of 0.2° . The obtained data were analysed using PDF-2 database. Microstructure of titanium powders was investigated by SEM method on Ultra Plus microscope by Carl Zeiss (Germany). The obtained synthesis products were milled in a planetary mill Pulverisette by Fritsch (Germany) for 5 minutes with zirconium oxide balls of 8 mm diameter with a weight ratio of balls and mixture 30:1, rotor speed 320 rpm.

3. Results and Discussion

At the first stage, initial titanium powders used in the mixtures were thermovacuum-treated. The mass loss due to heat treatment was about 0.7 wt.% at $d(\text{Ti}) = 60 \mu\text{m}$ and 0.2 % at $d(\text{Ti}) = 120 \mu\text{m}$.

The external view and combustion shots of titanium-based powder and granulated charge at $d(\text{Ti}) = 60 \mu\text{m}$ are shown in Fig. 4. The mixtures with $d(\text{Ti}) = 120 \mu\text{m}$ look almost the same.

The rate of propagation of the combustion front is the most important macrokinetic parameter of the combustion process. Synthesis of mixtures with $d(\text{Ti}) = 60 \mu\text{m}$ (a) and $120 \mu\text{m}$ (b), both powder and granular mixtures was carried out in steady-state regime. The shape of the combustion front is flat, which allowed reliable measurement of the position of the combustion front at different moments of time and determination of its propagation rate.

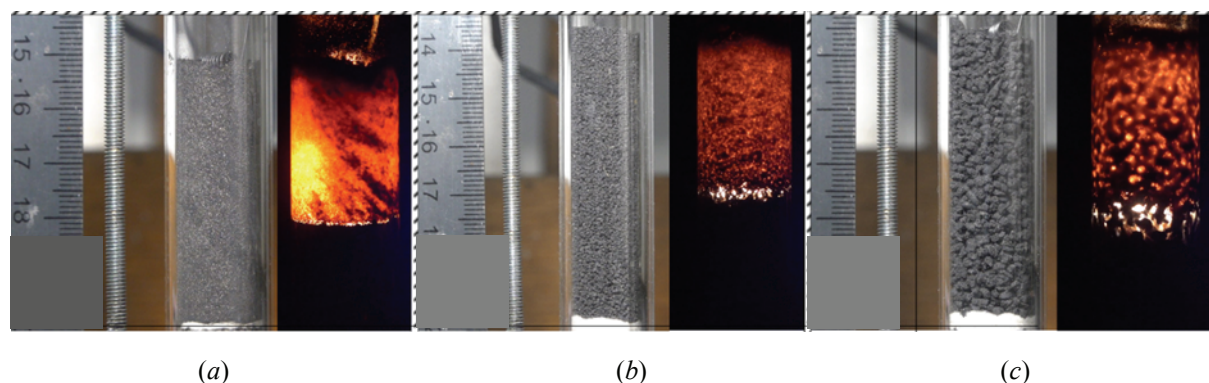


Fig. 4. External view of a quartz tube and frames of combustion of (Ti + C) + 20 % NiCr mixtures with $d(\text{Ti}) = 60 \mu\text{m}$ (a) and $120 \mu\text{m}$ (b, c): the initial powder mixture (a), granular mixture with $D = 0.6 \text{ mm}$ (b), and granular mixture with $D = 1.7 \text{ mm}$ (c)

Table 2. Combustion rates U_p of powder and $U_{gr}(D)$ mixtures with granules of size D ; combustion rate U_{com} of the substance of the granules

$d(\text{Ti}), \mu\text{m}$	$U_p, \text{mm}\cdot\text{s}^{-1}$	$U_{gr}(0.6 \text{ mm}), \text{mm}\cdot\text{s}^{-1}$	$U_{gr}(D = 1.7 \text{ mm}), \text{mm}\cdot\text{s}^{-1}$	$U_{com}, \text{mm}\cdot\text{s}^{-1}$	U_{com}/U_p
60	20	32	39	44	2.2
120	8	17	20.5	23	2.9

The values of combustion rates used in the calculations are averages from 3–4 experiments, the value spread is not more than 10 %. Table 2 shows the experimental values of combustion rates of powder and granular mixtures of 80 % (Ti + C) + 20 % NiCr with titanium particles of 60 and 120 μm in size.

At the same nichrome content, the combustion rates of titanium-based powder mixtures with $d(\text{Ti}) = 60 \mu\text{m}$ are almost twice as high as those with $d(\text{Ti}) = 120 \mu\text{m}$. To explain the difference in the combustion rates of powder mixtures with titanium particles of different sizes, we shall use the convective-conductive combustion model (CCCM) [50]. In accordance with this model, the propagation of the combustion wave front in a powder mixture is the movement of the melt of a fusible component under the action of capillary forces and pressure difference of impurity gases in front of and behind the melt layer. An increase in the pressure of impurity gases in front of the reaction front leads to a decrease in the combustion rate, and a decrease in pressure leads to an increase in the combustion rate. Usually, the influence of impurity gas emitted behind the melt layer (combustion front) can be neglected because it does not create increased pressure due to the high gas permeability of combustion products [51].

In accordance with [52], we consider that in a powder mixture the particles of initial components

have time to heat up and release impurity gas before the combustion front if two conditions are simultaneously fulfilled:

$$d < L, \quad (1)$$

$$t_h < t. \quad (2)$$

Here d is the characteristic particle size of the powder mixture, $L = a_c/U_p$ is the width of the heating zone, U_p is the experimental combustion rate, a_c is the thermal diffusivity coefficient of the heterogeneous powder mixture, $t_h(d) = d^2/4a$ is the thermal relaxation time of the particle, a is the thermal diffusivity coefficient of the particle substance and $t = L/U_p = a_c/U_p^2$ is the characteristic time of the particle in the heating zone [1]. During calculations, the value of a_c was assumed to be the same, equal to $a_c = 10^{-6} \text{ m}^2\cdot\text{s}^{-1}$ [53].

Calculation of the heating condition (1) showed that for titanium particles ($a(\text{Ti}) = 8 \cdot 10^{-6} \text{ m}^2\cdot\text{s}^{-1}$ [54], the width of the heating zone $L = 50 \mu\text{m}$ for mixtures with $d(\text{Ti}) = 60 \mu\text{m}$ and $L = 125 \mu\text{m}$ for mixtures with $d(\text{Ti}) = 120 \mu\text{m}$. Thus, $L < d(\text{Ti})$ for 60 μm titanium particles and $L > d(\text{Ti})$ for 120 μm titanium particle sizes. Soot particles ($d(\text{C}) = 3\text{--}4 \mu\text{m}$, $a(\text{C}) = 2 \cdot 10^{-7} \text{ m}^2\cdot\text{s}^{-1}$ [55]) are heated and release impurity gas ahead of the combustion front in both cases. Nichrome contains 80 % Ni, and Ni particles release negligible amounts of impurity gas compared to

titanium and soot [42], so the effect of outgassing from nichrome can be neglected. The heating condition (2) is fulfilled for all components. Thus, inhibition of the combustion front by impurity gases from titanium for mixtures with $d(\text{Ti}) = 120 \text{ }\mu\text{m}$ and its absence for mixtures with $d(\text{Ti}) = 60 \text{ }\mu\text{m}$ explains the difference in the combustion rate of powder mixtures 80 % (Ti + C) + 20 % NiCr. A quantitative assessment of the influence of impurity outgassing on the combustion rates of these mixtures can be obtained by comparing them with the combustion rates of granular mixtures.

Table 2 shows that the combustion rates of granular mixtures were higher than those of powder mixtures of the same composition. This is due to a different mechanism of propagation of the combustion front in granular mixtures, in which the combustion rate is determined by both the combustion rate of individual granules and the rate of heat transfer from granule to granule. A granular mixture consists of individual cells (granules) containing the powder mixture and the pore space between them. It is precisely because of the discrete nature of granular mixtures and the difference in the size of the granules and grains of the resulting product that surface tension forces prevent the melt from flowing beyond the individual granules. Therefore, the high gas permeability of such charge practically does not change during the combustion process. Since the size of granules (about 1 mm) is much larger than the particle size of the initial powders, the combustion process of an individual granule can be considered similar to the combustion process of a powder mixture [44]. However, the granule has better conditions for the removal of impurity gases from the combustion zone compared to the powder charging, since the length of the filtration zone does not exceed half of the granule diameter D . In combination with the high gas permeability of the entire charging, this leads to an insignificant influence of the impurity gas release both on the combustion process of the granules themselves and on the whole sample [44]. However, a granule has better conditions for the removal of impurity gases from the combustion zone compared to a powder sample, since the length of the filtration zone does not exceed half the diameter of the granule D . In combination with the high gas permeability of the entire sample, this leads to a slight effect of impurity gas release on both levels of the combustion process: the granules themselves and the sample [56]. If in the powder mixture there is no gas release in the heating zone, granulation will lead to a decrease in the combustion rate of the sample. This is due to the presence of a granule to granule combustion transfer stage. In contrast, for the

composition where impurity gases are released in the heating zone and have an inhibitory effect, granulation leads to an increase in the combustion rate. Consequently, the observed ratio $U_{\text{gr}} > U_{\text{p}}$ (Table 2) results from the levelling of the impurity gas influence, which is released before the melt layer from soot particles, and in the mixture with $d(\text{Ti}) = 120 \text{ }\mu\text{m}$ – also from titanium particles.

During the combustion process, the granules of the studied mixtures retained their size and sintered lightly with each other. Therefore, it is assumed that the heat transfer between them occurred mainly at the contact points of the granules and is determined by a conductive mechanism. An upper estimate of the granule heating depth $H = (a_c D / U_{\text{gr}})^{1/2}$ by the time of ignition [44] gives $H = 0.19 \text{ mm}$ for granules of size $D = 0.6 \text{ mm}$ and $H = 0.17 \text{ mm}$ for $D = 1.7 \text{ mm}$, that is, $H < D$. Therefore, the heating of the granule up to the moment of ignition is described by the semi-infinite body model. Then the combustion rate of the granule substance U_{com} and the time of transfer of combustion between granules t_{ig} can be considered the same for granules of different sizes. Considering that the total burning time of the granule $t_{\text{b}} = D / U_{\text{gr}}$ is the sum of the combustion time of the granule substance D / U_{com} and the combustion transfer time from granule to granule t_{ig} , i.e.

$$t_{\text{b}} = D / U_{\text{com}} + t_{\text{ig}}, \quad (3)$$

we obtain an expression relating U_{com} and t_{ig} to the combustion rate of the granular mixture U_{gr} [44]:

$$U_{\text{gr}} = U_{\text{com}} / (1 + U_{\text{com}} t_{\text{ig}} / D). \quad (4)$$

By solving the system of two equations with two unknowns, obtained by successive substitution of D and U_{gr} values for two fractions of granules of the same composition into (4), the values $U_{\text{com}} = 44 \text{ mm}\cdot\text{s}^{-1}$, $t_{\text{ig}} = 5 \text{ ms}$ for $d(\text{Ti}) = 60 \text{ }\mu\text{m}$, and $U_{\text{com}} = 23 \text{ mm}\cdot\text{s}^{-1}$, $t_{\text{ig}} = 9 \text{ ms}$ for $d(\text{Ti}) = 120 \text{ }\mu\text{m}$ are obtained. These results allow to assume that a conductive combustion mechanism is realized in the investigated sample-scale mixtures.

The ratio of the combustion rate of the granule substance and the powder mixture gives a quantitative estimate of the inhibitory effect of impurity gas release on the combustion rate of the powder mixture: $U_{\text{com}} / U_{\text{p}} = 2.2$ and 2.9 at $d(\text{Ti}) = 60$ and $120 \text{ }\mu\text{m}$, respectively. These estimates are close, and it is due to the rather low impurity gas content in titanium with $d(\text{Ti}) = 120 \text{ }\mu\text{m}$ (0.2 %), which inhibits the combustion.

The data of X-ray phase analysis (XRF) of combustion products of powder and granular mixtures are shown in Fig. 5.

It was found that the phase composition of the synthesis products of 80 % (Ni + C) + 20 % NiCr mixtures is strongly influenced by the particle size of the initial titanium powder and the type of mixture. Thus, for $d(\text{Ti}) = 60 \mu\text{m}$ the composition of combustion products of powder and granular charge was the same and included phases TiC and Ni_3Cr , which coincides with the data of thermodynamic calculations. So, the observed difference in the dependence of combustion rates of powder and granular mixtures cannot be explained by a change in the phase composition of the combustion products, thus supporting the proposed explanation – the influence of impurity gas released during combustion from the components of the mixtures. In turn, $d(\text{Ti}) = 120 \mu\text{m}$ is characterized by faint Ni_3Cr bond peaks, as well as by-product phases of intermetallides, which are particularly abundant in the

powder mixture. As in [43], there is a correlation between the smaller titanium particle size, higher combustion rate of the mixture, and the absence of intermetallic side phases.

Combustion products' samples from granules of different sizes for titanium-based mixtures of the same dispersity had similar phase composition (Fig. 6).

Thus, to obtain the target phase composition of combustion products of the studied mixtures, as in the case of nickel-bonded titanium carbide [44], it is necessary to use granular mixtures based on finely dispersed titanium powder. For the studied mixture, a safe conductive mode of combustion is realised irrespective of the granule size in the range of 0.6–1.7 mm.

As in the case of previously investigated Ti–C–Ni mixtures [57], synthesis from the granular mixture yields a sample in which the granules retain their dimensions, fuse only at the contact points, and are easily separated from each other (Figs. 7, 8).

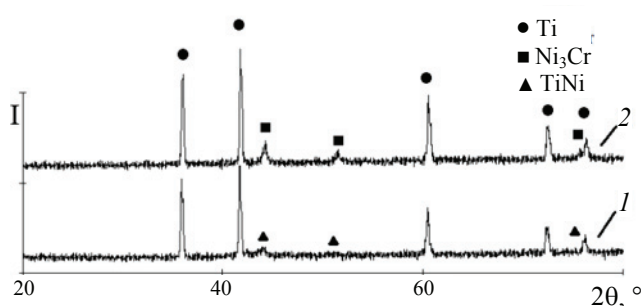


Fig. 5. Results of X-ray phase analysis of combustion products of a granular mixture of Ti + C + 20 % NiCr with 1.7 mm granules at $d(\text{Ti}) = 120 \mu\text{m}$ (1) and at $d(\text{Ti}) = 60 \mu\text{m}$ (2)

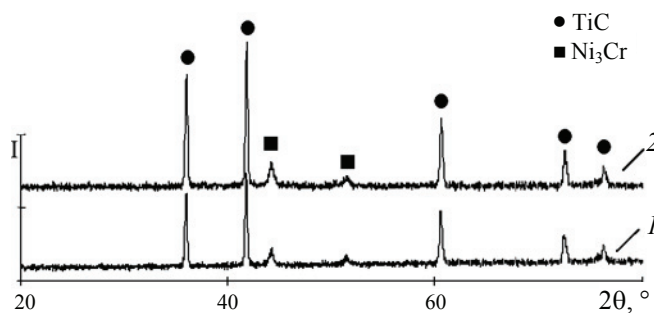


Fig. 6. Results of X-ray phase analysis of the combustion products of the Ti + C + 20 % NiCr granular mixture based on titanium with $d(\text{Ti}) = 60 \mu\text{m}$: 1 – 0.4–0.8 fraction granules; 2 – 1.4–2.0 fraction granules

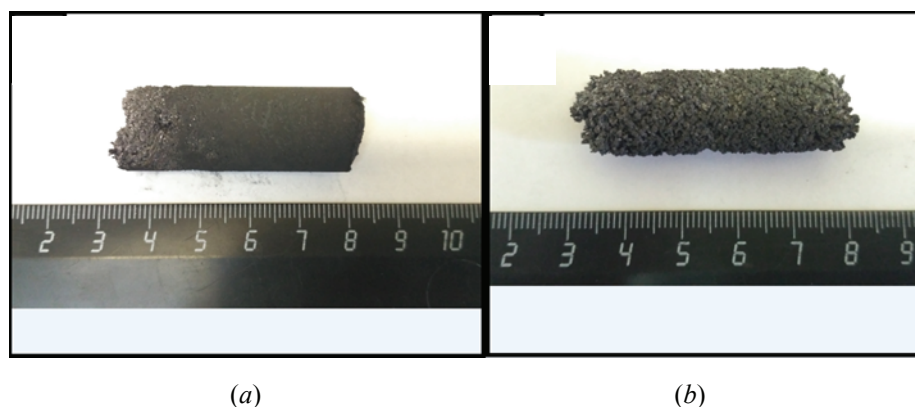


Fig 7. Samples of powder (a) and granular (b) mixtures with $D = 1.7 \text{ mm}$ after combustion

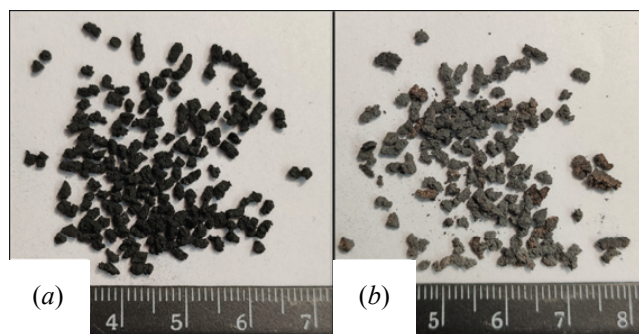


Fig. 8. Photographs of a granular mixture of 80 % (Ti + C) + 20 % NiCr composition with $D = 1.7$ mm before (a) and after (b) synthesis

After the synthesis of composites from powder and granular mixtures, a comparison of the milling efficiency of the obtained products was performed. The samples were milled in a planetary mill for 5 minutes, with a rotor speed of 320 rpm. At milling of the combustion product of titanium-based powder mixture with $d(\text{Ti}) = 60 \mu\text{m}$ the yield of fraction $< 250 \mu\text{m}$ was 5 %, and from the granular one with granules of size $D = 1.7$ mm – 94 % of the total mass of the sample.

4. Conclusion

The studies have shown that granulation of the initial charge 80 % (Ti + C) + 20 % NiCr (granule size 0.6–1.7 mm) on the basis of titanium with a specific particle size of $60 \mu\text{m}$ provides the synthesis of titanium carbide with nichrome bonding in a safe conductive mode, i.e. provides the possibility of scaling the process. Facilitated micron-size crushing of synthesis products from granular charges makes the process attractive for obtaining fine powders for wear-resistant coatings [3].

5. Funding

This study received no external funding.

6. Acknowledgements

The study was carried out using the equipment of the Distributed Core Facility Centre of the Merzhanov Institute of Structural Macrokinetics and Materials Science.

7. Conflict of interests

The authors declare no conflict of interest.

References

1. Liu Y, Yu BH, Guan DH, Wang Z-B, Bi J. Microstructure and properties of TiC/NiCr cermets produced by partial liquid-phase sintering. *Journal of*

Materials Science Letters. 2001;20:619-620. DOI:10.1023/A:1010965216385

2. Chesnokov AE, Filippov AA. Study of physical properties of Ti–C–NiCr cermet compacts obtained by hot pressing. *Journal of Applied Mechanics and Technical Physics*. 2022;63(2):329-334. DOI:10.1134/S002189442202016

3. Bolell G, Colella A, Lusvarghi L, Morelli S, Puddu P, Righetti E, Sassatelli P, Testa V. TiC–NiCr thermal spray coatings as an alternative to WC–CoCr and Cr_3C_2 –NiCr. *Wear*. 2020;450-451:203273(1-23). DOI:10.1016/j.wear.2020.203273

4. Kiryukhantsev-Korneev PV, Sytchenko AD, Levashov EA. Comparative study of coatings formed by electrospray alloying using TiC–NiCr and Ti–C–NiCr– Eu_2O_3 electrodes. *Russian Journal of Non-Ferrous Metals*. 2019;60:662-672. DOI:10.3103/S1067821219060099

5. Cordoba JM, Chicardi E, Gotor FJ. Liquid-phase sintering of Ti (C, N)-based cermets. The effects of binder nature and content on the solubility and wettability of hard ceramic phases. *Journal of Alloys and Compounds*. 2013; 559:34-38. DOI:10.1016/j.jallcom.2013.01.046

6. Sahoo P, Davim JP. Tribology of ceramics and ceramic matrix composites. In: *Tribology for Scientists and Engineers*. New York: Springer; 2013. p. 211-31. DOI:10.1007/978-1-4614-1945-7

7. Caccia M, Tabandeh-Khorshid M, Itskos G, Strayer AR, et al. Ceramic–metal composites for heat exchangers in concentrated solar power plants. *Nature*. 2018;562:406-409. DOI:10.1038/s41586-018-0593-1

8. Rajabi A, Ghazali M, Junaiddi S, Daud A. Development and application of tool wear: a review of the characterization of TiC-based cermets with different binders. *Chemical Engineering Journal*. 2014;255:445-452. DOI:10.1016/j.cej.2014.06.078

9. Guo X, Yang H, Zhu X, Zhang L. Preparation and properties of nano-SiC-based ceramic composites containing nano-TiN. *Scripta Materialia*. 2013;68:281-284. DOI:10.1016/j.scriptamat.2012.10.042

10. Aslantas K, Uzun I, Cicek A. Tool life and wear mechanism of coated and uncoated Al_2O_3 /TiCN mixed ceramic tools in turning hardened alloy steel. *Wear*. 2012;274:442-451. DOI:10.1016/j.wear.2011.11.010

11. Singh P, Singh B, Kumar M, Kumar A. One step reduction of boric acid to boron carbide nanoparticles. *Ceramics International*. 2014;40:15331-15334. DOI:10.1016/j.ceramint.2014.06.101

12. Toth L. *Transition metal carbides and nitrides*: Elsevier; 2014. 296 p.

13. Funamori N, Sato T. A cubic boron nitride gasket for diamond-anvil experiments. *Review of Scientific Instruments*. 2008;79:053903. DOI:10.1063/1.2917409

14. Muguthu JN, Gao D. Profile fractal dimension and dimensional accuracy analysis in machining metal matrix composites (MMCs). *Materials and Manufacturing Processes*. 2013;28:1102-1109. DOI:10.1080/10426914.2013.823501

15. Komratov GN. Kinetics of oxidation SHS of titanium carbide and titanium and chromium double carbide powders in air. *Powder Metallurgy and Metal Ceramics*. 1993;32(6):509-511. DOI:10.1007/BF00560730
16. Aramian A, Sadeghian Z, Prashanth KG, Berto F. In situ fabrication of TiC–NiCr cermets by selective laser melting. *International Journal of Refractory Metals and Hard Materials*. 2019;87:105171. DOI:10.1016/j.jirmhm.2019.105171
17. Delbar SA, Sabahi Namini A, Shahedi Asl M. Hybrid Ti matrix composites with TiB₂ and TiC compounds. *Materials Today Communications*. 2019;20:100576. DOI:10.1016/j.mtcomm.2019.100576
18. Qi Q, Liu Y, Zhang H, Zhao J, Huang Z. The adjustment of microstructure and properties of TiC/Ni–Cr composites by Mo addition applied for intermediate temperature solid oxide fuel cell interconnects. *Journal of Alloys and Compounds*. 2016;678:375-382. DOI:10.1016/j.jallcom.2016.03.301
19. Yerui F, Yongfeng G, Zongfeng L. Experimental investigation of EDM parameters for TiC/Ni cermet machining. In: *Procedia CIRP*. Elsevier; 2016; p. 18-22.
20. Zhang W, Sui ML, Zhou YZ, Guo JD, He GH, Li DX. Evolution of microstructure in TiC/NiCr cermet induced by electropulsing. *Journal of Materials Research*. 2003;18:1543-1550. DOI:10.1557/JMR.2003.0213
21. Borisov YS, Borisova AL, Kolomytsev MV, Masyuchok OP, Timofeeva II, Vasilkovskaya MA. High-velocity air plasma spraying of (Ti, Cr)C–32 wt. % Ni clad powder. *Powder Metallurgy and Metal Ceramics*. 2017;56(5-6):305-315. DOI:10.1007/s11106-017-9898-0
22. Andreev AV, Litovchenko IY, Korotaev AD, Borisov DP. Thermal stability of Ti–C–Ni–Cr and Ti–C–Ni–Cr–Al–Si nanocomposite coatings. *Journal of Physics: Conference Series*. 2015;652:012057. DOI:10.1088/1742-6596/652/1/012057
23. Borisova AL, Borisov YS. Self-propagating high-temperature synthesis for the deposition of thermal-sprayed coatings. *Powder Metallurgy and Metal Ceramics*. 2008;47:80-94. DOI:10.1007/s11106-008-0012-5
24. Bartuli C, Smith RW. Comparison between Ni–Cr–40 vol. % TiC wear-resistant plasma sprayed coatings produced from self-propagating high-temperature synthesis and plasma densified powders. *Journal of Thermal Spray Technology*. 1996;5:335-342. DOI:10.1007/BF02645885
25. Bartuli C, Smith RW, Shtessel E. SHS powders for thermal spray applications. *Ceramics International*. 1997; 23(1):61-68. DOI:10.1016/S0272-8842(95)00141-7
26. Kunrath AO, Upadhaya K, Reimanis IE, Moore JJ. Synthesis and application of composite TiC–Cr₃C₂ targets. *Surface and Coatings Technology*. 1997;94-95:237-241. DOI:10.1016/S0257-8972(97)00349-6
27. Wang BQ, Verstak A. Elevated temperature erosion of HVOF Cr₃C₂/TiC–NiCrMo cermet coating. *Wear*. 1999;233-235:342-351. DOI:10.1016/S0043-1648(99)00242-2
28. Steinhäuser S, Wielage B, Hofmann U, Schnick Th, Ilyuschenko A, Azarova T. Plasma-sprayed wear-resistant coatings with respect to ecological aspects. *Surface and Coatings Technology*. 2000;131:365-371. DOI:10.1016/S0257-8972(00)00817-3
29. Jones M, Horlock AJ, Shipway H, McCartney DG, Wood JV. Microstructure and abrasive wear behavior of FeCr–TiC coatings deposited by HVOF spraying of SHS powders. *Wear*. 2001;249:246-253. DOI:10.1016/S0043-1648(01)00560-9
30. Jones M, Horlock AJ, Shipway PH, McCartney DG, Wood JV. A comparison of the abrasive wear behaviour of HVOF sprayed titanium carbide and titanium boride-based cermet coatings. *Wear*. 2001;251:1009-1016. DOI:10.1016/S0043-1648(01)00702-5
31. Horlock AJ, McCartney DG, Shipway PH, Wood JV. Thermally sprayed Ni(Cr)–TiB coatings using powder produced by self-propagating high temperature synthesis: Microstructure and abrasive wear behavior. *Materials Science and Engineering*. 2002;A336:88-98. DOI:10.1016/S0921-5093(01)01918-9
32. Degnan CC, Shipway PH. A comparison of the reciprocating sliding wear behavior of steel-based metal matrix composites processed from self-propagating high-temperature synthesized Fe–TiC and Fe–TiB₂ master alloys. *Wear*. 2002;252(9-10):832-841. DOI:10.1016/S0043-1648(02)00051-0
33. Licheri R, Orru R, Cao G, Crippa A, Scholz R. Self-propagating combustion synthesis and plasma spraying deposition of TiC–Fe powders. *Ceramics International*. 2003;29:519-526. DOI:10.1016/S0272-8842(02)00196-7
34. Licheri R, Orru R, Locci AM, Cao G. Combustion synthesis of TiC-metal composites and related plasma spraying deposition. *International Journal of Materials and Product Technology*. 2004;20:464-478. DOI:10.1504/IJMPT.2004.004791
35. Dercz G, Formanek B, Prusik K, Pajak L. Microstructure of Ni(Cr)–TiC–Cr₃C₂–Cr₇C₃ composite powder. *Journal of Materials Processing Technology*. 2005;162-163:15-19. DOI:10.1016/j.jmatprotec.2005.02.004
36. Borisova AL, Borisov YuS. Self-propagating high-temperature synthesis for the deposition of thermal-sprayed coatings. *Powder Metallurgy and Metal Ceramics*. 2008;47:80-94. DOI:10.1007/s11106-008-0012-5
37. Munir Z, Anselmi-Tamburini V. Self-propagating exothermic reactions: the synthesis of high-temperature materials by combustion. *Materials Science Reports*. 1989;3:277-365. DOI:10.1016/S0920-2307(89)80002-7
38. Talako T, Ilyuschenko A, Letsko A. SHS powders for thermal spray coating. *KONA Powder and Particle Journal*. 2009;27:55-72. DOI:10.14356/kona.2009008
39. Kunrath AO, Reimanis IE, Moore JJ. Microstructural evolution of titanium carbide-chromium carbide (TiC–Cr₃C₂) composites produced via combustion synthesis. *Journal of the American Ceramic Society*. 2004; 85(5):1285-1290. DOI:10.1111/j.1151-2916.2002.tb00259.x

40. Han JC, Zhang X.-H, Wood J. In-situ combustion synthesis and densification of TiC-xNi cermets. *Materials Science and Engineering: A*. 2000;280(2):328-333. DOI:10.1016/S0921-5093(99)00606-1
41. Solonenko OP, Ovcharenko VE, Ulianitsky VYu, Chesnokov AE, Batraev IS. Effect of the microstructure of SHS powders of titanium carbide-nichrome on the properties of detonation coatings. *Journal of Surface Investigation: X-ray, Synchrotron and Neutron Techniques*. 2016;10(5):1040-1047. DOI:10.1134/S1027451016050402
42. Seplyarskii BS, Kochetkov RA. Granulation as a tool for stabilization of SHS reactions. *International Journal of Self-Propagating High-Temperature Synthesis*. 2017;26(2):134-136. DOI: 10.3103/S106138621702011X
43. Seplyarsky BS, Kochetkov RA, Lisina TG, Abzalov NI. The effect of synthesis conditions on phase composition and structure of combustion products of nickel-bonded titanium carbide. *Advanced Materials and Technologies*. 2017;4:22-28. DOI:10.17277/amt.2017.04.pp.022-028
44. Seplyarskii BS, Kochetkov RA, Lisina TG, Rubtsov NM, Abzalov NI. Explanation of increase in combustion velocity of Ti + C powder mixture upon dilution with nickel using convective-conductive combustion model. *International Journal of Self-Propagating High-Temperature Synthesis*. 2022;31(4):195-206. DOI:10.3103/S1061386222040100
45. Seplyarskii BS, Abzalov NI, Kochetkov RA, Lisina TG. Effect of the polyvinyl butyral content on the combustion code of the (Ti + C) + xNi granular mixture. *Russian Journal of Physical Chemistry B*. 2021;15(2):242-249. DOI:10.1134/S199079312102010X
46. Seplyarskii BS, Kochetkov RA, Abzalov NI, Kovalev ID, Lisina TG. Influence of granulation and Ni-containing binder composition on the self-propagating high-temperature synthesis of carbides in the Ti-Cr-C system. *Inorganic Materials*. 2020;56(9):909-917. DOI:10.1134/S0020168520080142
47. Seplyarskii BS, Kochetkov RA, Lisina TG, Alymov MA. The conditions for the implementation of the convective mode of combustion for granular mixtures of Ti + xC. *IOP Conference Series: Materials Science and Engineering*. 2019;558:012045. DOI:10.1088/1757-899X/558/1/012045
48. Gusachenko LK, Zarko VE, Rychkov AD, Shokina NYu. Filtration combustion of an energetic material in a concurrent flow of its combustion products. critical combustion conditions. *Combustion, Explosion and Shock Waves*. 2003;39:694-700. DOI:10.1023/B:CESW.0000007683.81353.91
49. Seplyarskii BS, Abzalov NI, Kochetkov RA, Lisina TG. Effect of the content of polyvinyl butyral on the synthesis and phase composition of products of combustion of Ti-Cr-C granular mixture. *Russian Journal of Physical Chemistry A*. 2021;95(12):2408-2414. DOI:10.1134/S0036024421120189
50. Seplyarskii BS. The nature of the anomalous dependence of the velocity of combustion of "gasless" systems on the sample diameter. *Doklady Physical Chemistry*. 2004;396(4-6):130-133. DOI:10.1023/B:DOPC.0000033505.34075.0a
51. Azatyan TS, Mal'tsev VM, Merzhanov AG, Seleznev VA. Spectral-optical investigation of the mechanism of the combustion of mixtures of titanium and carbon. *Combustion, Explosion and Shock Waves*. 1977;13(2):156-158. DOI:10.1007/BF00754993
52. Seplyarskii BS, Kochetkov RA, Lisina NG, Rubtsov NM, Abzalov NI. Macrokinetic analysis of the combustion patterns in the transition from powder to granulated mixtures by the example of 5Ti + 3Si and Ti + C compositions. *Combustion and Flame*. 2022;236:111811. DOI:10.1016/j.combustflame.2021.111811
53. Zenin AA, Merzhanov AG, Nersisyan GA. Thermal wave structure in SHS processes. *Combustion, Explosion and Shock Waves*. 1981;17(1):63-71. DOI:10.1007/BF00772787
54. Slezak T, Zmywaczyk J, Koniorczyk P. Thermal diffusivity investigations of the titanium grade 1 in wide temperature range. *AIP Conference Proceedings*. 2019;2170(1):020019. DOI:10.1063/1.5132738
55. Korol'chenko IA, Kazakov AV, Kukhtin AS, Krylov VL. Experimental determination of thermal conductivity of materials. *Pozharovzryvbezopasnost' Veshch. Materials*. 2004;13(4):36-38 (In Russ.)
56. Martirosyan NA, Dolukhanyan SK, Merzhanov AG. Critical phenomena in combustion of mixtures of the type As+Bs+Cg (example of the titanium-carbon-hydrogen system). *Combustion, Explosion and Shock Waves*. 1981;17(4):369-373. DOI:10.1007/BF00761202
57. Seplyarskii BS, Abzalov NI, Kochetkov RA, Lisina TG. Combustion of granulated Ti-C-Ni mixtures: influence of granule size. *International Journal of Self-Propagating High-Temperature Synthesis*. 2021;30(3):185-187. DOI:10.3103/S1061386221030079

Information about the authors / Информация об авторах

Nail I. Abzalov, Cand. Sc. (Phys. and Math), Junior Researcher Associate, Merzhanov Institute of Structural Macrokinetics and Materials Science RAS (ISMAN), Chernogolovka, Russian Federation; ORCID 0000-0003-0970-3709; e-mail: abzalov396@mail.ru

Абзалов Наиль Илдусович, кандидат физико-математических наук, научный сотрудник, Институт структурной макрокинетики и проблем материаловедения им. А.Г. Мерджанова РАН (ИСМАН), Черноголовка, Российская Федерация; ORCID 0000-0003-0970-3709; e-mail: abzalov396@mail.ru

Boris S. Seplyarskii, Cand. Sc. (Phys. and Math), Leading Researcher, ISMAN, Chernogolovka, Russian Federation; ORCID 0000-0003-0852-184X; e-mail: seplb1@mail.ru

Roman A. Kochetkov, Cand. Sc. (Phys. and Math), Senior Researcher, ISMAN, Chernogolovka, Russian Federation; ORCID 0000-0003-4364-7464; e-mail: numenor@list.ru

Tatiana G. Lisina, Cand. Sc. (Phys. and Math), Senior Researcher, ISMAN, Chernogolovka, Russian Federation; ORCID 0000-0003-0454-6273; e-mail: lisina@ism.ac.ru

Mikhail I. Alymov, D. Sc. (Eng.), Professor, Corresponding member of RAS, Director ISMAN, Chernogolovka, Russian Federation; ORCID 0000-0001-6147-5753; e-mail: alymov@ism.ac.ru

Сеплярский Борис Семенович, кандидат физико-математических наук, ведущий научный сотрудник, ИСМАН, Черноголовка, Российская Федерация; ORCID 0000-0003-0852-184X; e-mail: seplb1@mail.ru

Кочетков Роман Александрович, кандидат физико-математических наук, старший научный сотрудник, ИСМАН, Черноголовка, Российская Федерация; ORCID 0000-0003-4364-7464; e-mail: numenor@list.ru

Лисина Татьяна Геннадиевна, кандидат физико-математических наук, старший научный сотрудник, ИСМАН, Черноголовка, Российская Федерация; ORCID 0000-0003-0454-6273; e-mail: lisina@ism.ac.ru

Алымов Михаил Иванович, доктор технических наук, профессор, член-корр. РАН, директор ИСМАН, Черноголовка, Российская Федерация; ORCID 0000-0001-6147-5753; e-mail: alymov@ism.ac.ru

Received 30 June 2023; Accepted 07 September 2023; Published 15 December 2023



Copyright: © Abzalov NI, Seplyarskii BS, Kochetkov RA, Lisina TG, Alymov MI, 2023. This article is an open access article distributed under the terms and conditions of the Creative Commons Attribution (CC BY) license (<https://creativecommons.org/licenses/by/4.0/>).

Территория распространения – Российская Федерация, зарубежные страны
Distributed in the Russian Federation and foreign countries

Computer layout: Olga V. Mochalina, TSTU, Tambov, Russian Federation
Компьютерный дизайн и верстка: Мочалина О. В., ТГТУ, Тамбов, Россия

Оригинал-макет подготовлен в Издательском центре ФГБОУ ВО «ТГТУ»,
392032, Тамбовская обл., г. Тамбов, ул. Мичуринская, д. 112А

Подписано в печать 27.11.2023. Дата выхода в свет 15.12.2023.

Формат 60×90/8. Усл. печ. л. 10,25. Уч.-изд. л. 10,55. Тираж 100 экз. Цена свободная. Заказ № 033.

СМИ журнал “Journal of Advanced Materials and Technologies”

(Журнал современных материалов и технологий) выпуск 2023. Том 8, № 4

Материалы журнала доступны по лицензии Creative Commons “Attribution” («Атрибуция») 4.0 Всемирная (CC BY 4.0)

All the materials of the “Golden Horde Review” are available under the Creative Commons License “Attribution” 4.0 International (CC BY 4.0)



ISSN 2782-2192



9 772782 219000 >